UNDERSTANDING FERROELASTIC DOMAIN REORIENTATION AS A DAMPING MECHANISM IN FERROELECTRIC REINFORCED METAL MATRIX COMPOSITES

Ben Poquette

PhD Dissertation

Materials Science and Engineering

Committee Members:

Dr. Stephen Kampe, Chairman
Dr. Alex Aning
Dr. Sean Corcoran
Dr. Gary Pickrell
Dr. William Reynolds
Dr. Jeffrey Schultz

September 25, 2007
Virginia Tech
Blacksburg, VA

Keywords: Metal Matrix Composites, Damping, Ferroelectric, Ferroelastic, Twinning, Domain Reorientation, Electroless Plating, Electrodeposition, Electroforming, Dispersion Strengthening

Understanding Ferroelastic Domain Reorientation as a Damping Mechanism in Ferroelectric Reinforced Metal Matrix Composites

Ben Poquette

(ABSTRACT)

Ferroelectric-reinforced metal matrix composites (FR-MMCs) offer the potential to improve damping characteristics of structural materials. Many structural materials are valued based on their stiffness and strength; however, stiff materials typically have limited inherent ability to dampen mechanical or acoustic vibrations. The addition of ferroelectric ceramic particles may also augment the strength of the matrix, creating a multifunctional composite. The damping behavior of two FR-MMC systems has been examined. One involved the incorporation of barium titanate ($BaTiO_3$) particles into a Cu- 10w%Sn (bearing bronze) matrix and the other incorporating them into an electroformed Ni matrix. Here the damping properties of the resulting ferroelectric reinforced metal matrix composites (FR-MMCs) have been investigated versus frequency, temperature (above and below the Curie temperature of the reinforcement), and number of strain cycles. FR-MMCs currently represent a material system capable of exhibiting increased damping ability, as compared to the structural metal matrix alone. Dynamic mechanical analysis and neutron diffraction have shown that much of this added damping ability can be attributed to the ferroelectric/ferroelastic nature of the reinforcement.

ACKNOWLEDGEMENTS

TABLE OF CONTENTS

TABLE OF FIGURES

ix

LIST OF TABLES

Chapter One- Project Introduction

Most structural metals are selected based on high stiffness and strength; however, stiff materials efficiently transmit vibrations, which are normally an unwanted side effect of mechanical motion. Because vibrations can cause mechanical failure via high cycle fatigue, induce physical discomfort, and compromise stealth, significant effort is made to eliminate them. Effective vibration suppression (damping) could be achieved by incorporating multifunctional composites, which can simultaneously improving passive damping, strength, and stiffness, into existing and planned structures.

Ferroelectric ceramics have been shown to have high damping behavior below their Curie temperatures (T_C), and the damping ability of these ceramics can be extended to stiff structural materials through compositing.[1-5] The addition of ferroelectric particles does not only improve damping capacity, but may also augment the load bearing capacity of the matrix, creating a multifunctional system.

A multifunctional material is designed to simultaneously address two or more engineering functions.[6] The concept of multifunctionality can be applied to many applications, including structural materials that are at the same time self-interrogating, self-healing, stealth providing, or energy dissipating. In most applications, the implementation of multifunctional materials leads to improved system efficiency. In this work, the feasibility of two systems was evaluated. One involved the incorporation of barium titanate ($BaTiO_3$) particles into a Cu- 10w%Sn (bearing bronze) matrix and the

other incorporating them into an electroformed Ni matrix. Here the damping properties of the resulting ferroelectric reinforced metal matrix composites (FR-MMCs) have been investigated versus frequency, temperature (above and below the Curie temperature of the reinforcement), and number of strain cycles.

The purpose of this work is to understand new methods to improve the overall quality of FR-MMCs as compared to work previously done in this area,[2-5, 7-10] while at the same time further the understanding of ferroelastic twinning as a damping mechanism and how environmental and loading parameters affect it.

Chapter Two- Background

The focus of this work is the fabrication and characterization of ferroelectric reinforced metal matrix composites (FR-MMCs) for damping and structural applications. This subject brings together several different areas of expertise. In order to address each of these areas, this chapter will be divided into five sections. The first section will focus on the concept of damping, the quantities used to represent it, and the methods used to measure damping ability in materials. Metal matrix composites (MMCs) and their strengthening mechanisms will be addressed in the second section, with the focus being on the predicted behavior of both the bronze-$BaTiO_3$ and electroformed Ni systems. The third section will address ferroelectric materials, what makes them unique, and ferroelastic domain motion as the root of their high-damping capability. Section four is focused on neutron diffraction and its use in materials characterization. Finally, section five will address electrochemical deposition, paying special attention to electroless plating onto nonconducting substrates and Ni electroforming.

1. Damping

In many practical applications, the rate at which elastic waves (periodically changing local strains) become attenuated in a structure is of considerable importance. For example, the use of components made from materials with a high damping ability leads to reduced noise and vibration in machinery. Here, the amplitude of vibration is lowered, reducing the noise volume and/or the danger of fatigue failure caused by vibrations.

Vibration is a form of simple harmonic motion. As with all motion, it will continue until a retarding force is applied. A retarding force is any force applied opposite that of the harmonic motion.   In passively damping materials, this retarding force comes in the form of resistance to strain leading to a phase lag between applied stress and material response. By this process, mechanical energy is dissipated, often in the form of heat. Thus, damping can be thought of as the dissipation of energy with time.

1.1 Damping Measurement in this Work

Dynamic Mechanical Analysis

Dynamic mechanical analysis (DMA) is a nondestructive testing technique that will be utilized in this work. In this method, the sample material is subjected to an oscillating force, as shown in Figure 1.
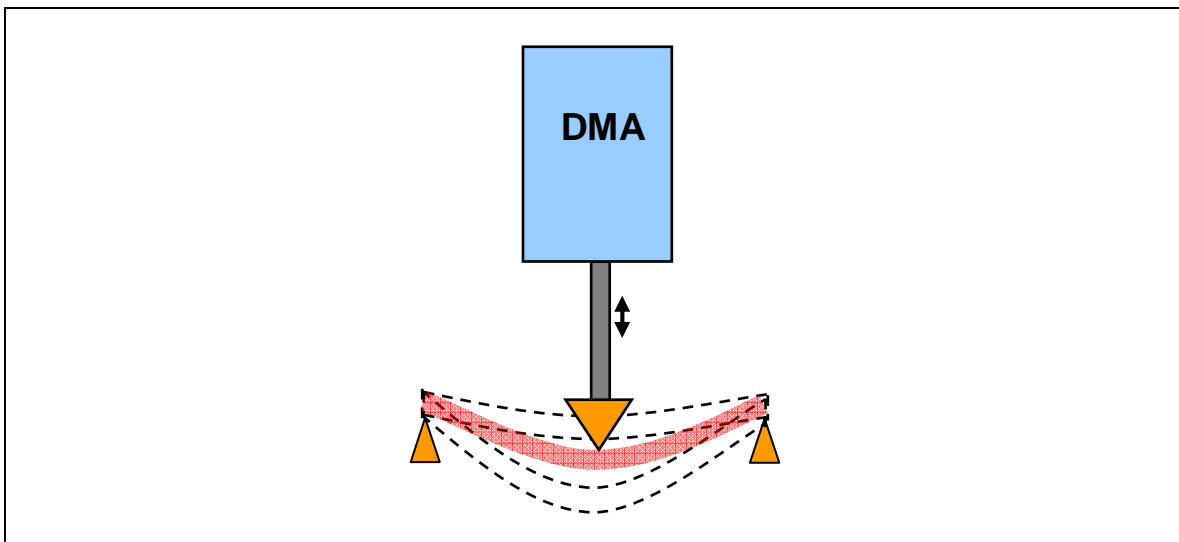
Figure 1. Schematic of a Dynamic Mechanical Analyzer, DMA

This force induces an oscillating strain response in the material, as shown in Figure 2.
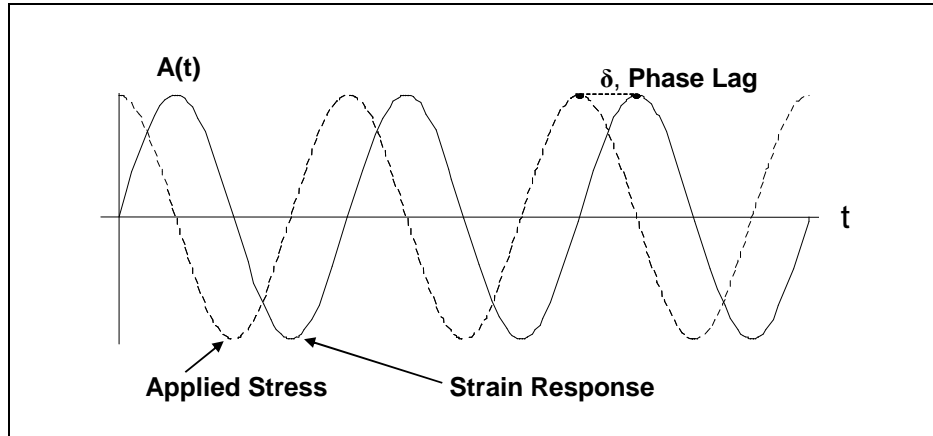
Figure 2. Applied stress and strain response in the material.

In most materials, there is a response time between when an object is stressed and when it responds to that stress. This response time results in a phase lag or phase angle (δ), between the curves for applied stress and strain response, and is essentially a manifestation of anelasticity. The tangent of this phase lag or loss tangent (tan δ) is commonly used to describe the damping ability of a material. For purely elastic materials the phase lag is zero degrees and 90 degrees for purely viscous ones.

To measure this value, the DMA records the raw signals of force, amplitude of deformation and phase lag directly. Force and amplitude can also be used with the phase lag to calculate the loss and storage stiffness (K'' and K'). *Tan δ* is calculated as the ratio of K'' to K'. The loss and storage moduli (E'' and E') are calculated by multiplying the raw stiffness measurements by appropriate geometry factors. It should be noted that tan δ can also be calculated as the ratio of E'' to E'. A good understanding of sample stiffness is important for understanding geometry selection when conducting DMA measurements.

Stress-Strain Hysteresis Method

Any material that is not perfectly elastic will exhibit some hysteresis when cyclically strained. Plotting this strain against the stress applied produces a hysteresis curve like that seen in Figure 3.[11]

5
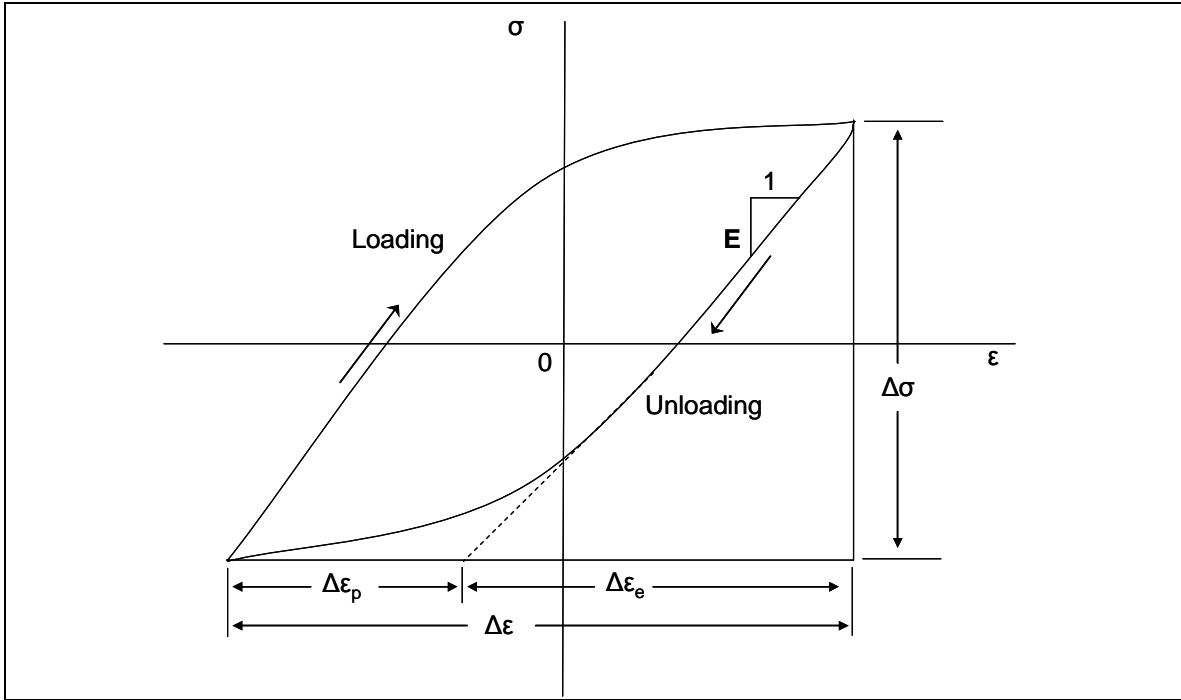
Figure 3. Stress-strain hysteresis curve.

Utilizing this curve, the specific damping capacity (Ψ) can be found using Eq 1,[12] where the energy dissipated (ΔW) is the area between the loading and unloading curve, and the energy stored (W) is the area under the loading curve in Figure 3.[13]

$$\psi = \frac{\Delta W}{W}$$ **Eq 1**

1.2 Nomenclature

As previously mentioned, all of the energy-absorbing processes active in a material contribute to its internal friction. Table 1 contains several commonly used quantities for describing internal friction.[14]

Table 1. Commonly used measures for internal friction

Loss Tangent	Loss Factor	Damping Ratio	Specific Damping Capacity, SDC	Logarithmic Decrement	Inverse Quality Factor	Ratio of Energy Loss to Elastic Stored Energy Per Cycle
$\tan \delta$	η	Z	Ψ	Δ	Q^{-1}	W_{loss}/W_{stored}

The relationship between these quantities is outlined in Eq 2.

$$\tan \delta = \eta = \zeta = \frac{\psi}{2\pi} = \frac{\Delta}{\pi} = Q^{-1} = 2\pi \frac{W_{loss}}{W_{stored}}$$

Eq 2

Here *tan δ* is referred to as the loss tangent. η is the loss factor. ζ is the damping ratio. Ψ represents the specific damping capacity. Δ is the logarithmic decrement. Q^{-1} is the inverse quality factor, and W_{loss}/W_{stored} is the ratio of the energy loss (W_{loss}) to the energy stored (W_{stored}) per cycle.

1.3 Damping Values of Selected Engineering Materials

As a general reference, the tan δ for several engineering materials has been given in Table 2.[14, 15] These room temperature values are what could be expected across a wide range of test parameters such as strain and frequency.

Table 2. Measured damping ability of several engineering materials at room temperature[14, 15]

Material	tan δ
Alumina (Al$_2$O$_3$)	$1 \cdot 10^{-5}$ - $3 \cdot 10^{-5}$
Steel	$2 \cdot 10^{-5}$ - $3 \cdot 10^{-3}$
Cast Iron	$6 \cdot 10^{-3}$ - $3 \cdot 10^{-2}$
Concrete	$1 \cdot 10^{-2}$ - $3 \cdot 10^{-2}$
Wood	$3 \cdot 10^{-3}$ - $3 \cdot 10^{-2}$
Polyethylene	$0.1 – 0.3$
Butyl Rubber	$0.3 – 4.0$

1.4 Damping Mechanisms in Materials

Materials for vibration damping are generally metals and polymers.[16] These materials generally have a sufficient elastic modulus to be useful in structural applications with sufficient energy dissipation ability to decrease vibration attenuation in the structure. Polymers, particularly thermoplastics, rely primarily on viscoelasticity as a damping mechanism. In metals, microstucture plays an important role in the activation damping mechanisms. Ceramics are generally not efficient damper, however due to their high stiffness, even small improvements in damping behavior can be extremely valuable. Composite systems of the above mentioned materials by their very nature, can exhibit a

high degree of interfacial damping.[17] This will be discussed in detail in section 2.4 of this chapter. All of these mechanisms however, are strongly dependent on the nature of the vibration applied to the system. Many will only become active within a certain stress range, can be strongly frequency dependent and/or have a limited life span.

Polymers

Rubber is commonly used as a high damping material, however its low modulus makes it unattractive as a purely structural material. Other common high damping polymers include polytetrafluoroethylene (PTFE), polyurethane, and several blends of polypropylene, polysulfone, polyimide, polyethylene, and polyvinylchloride (PVC).[16] In general, elastomer and other amorphous thermoplastics with a glass transition temperature below room temperature are attractive for damping due to their viscsoelastic properties. Here energy is dissipated as frictional heat as the polymer chains and/or molecules slide past one another.   Additionally the interfaces created in polymer blends and polymer based composites lend additional damping behavior.

Metals

Damping in most metals is heavily dependent on microstructure.[18] Certain structures however, can more easily facilitate certain mechanisms. All metals dissipate energy through the creation and movement of dislocations. In shape-memory alloys, a reversible, stress induced martensitic transformation can increase damping due to a large hysteresis between loading and unloading. Phase boundaries, grain boundaries and other boundaries in the material can also contribute to damping, as interfaces may move slightly slip with respect to one another during vibration. Also, when an elastic wave strikes such a defect, the imperfect transfer of elastic energy can lead to interfacial heating.

Ceramics

Ceramics are not commonly used primarily for damping, however due to their high stiffness, ceramic structures can benefit from any increase in damping. The most widely used structural ceramic is concrete, which is a composite of cement and aggregate. Fine particles of silica can be added to further increase amount of interface in this material which relies on interfacial composite mechanisms for its limited damping ability.[16]

2. Metal Matrix Composites

Metal matrix composites (MMCs) encompass a wide range of material and microstructural combinations, each of which has in common a continuous metallic matrix. MMCs can be further subdivided based on their reinforcement morphology. Reinforcements generally come in the form of continuous fibers, short fibers, or particles, each of which relies primarily on unique strengthening mechanisms.[19, 20] These categories are summarized in Table 3.

Table 3. Metal matrix composite subcategories

Type of MMC	Reinforcement Morphology	Primary Strengthening Mechanisms
Fiber Strengthened (Continuously Reinforced)	Long fibers (aspect ratio >10)	Shear lag theory (Load transfer from matrix to fiber)
Discontinuously Reinforced	Short fibers or whiskers (aspect ratio <10), and/or Large particles (diameter >1µm)	Combination of <u>fiber</u> and <u>dispersion</u> strengthening mechanisms
Dispersion Strengthened	Small particles (diameter <1µm)	Orowan inhibition of dislocation motion[21], Boundary strengthening - Matrix/reinforcement - Grain size refinement in the matrix Coefficient of thermal expansion mismatch

In this work, two discontinuous metal matrix composite systems were examined; one having a matrix of Cu-10w%Sn bronze and the other with an electroformed nickel, both reinforced with ~35µm $BaTiO_3$ ferroelectric ceramic particles.

2.1 Strengthening Mechanisms in Discontinuously Reinforced Metal Matrix Composites

Discontinuously reinforced composites fall somewhere between the dispersion strengthened and fiber strengthened extremes. A discontinuously reinforced composite's place between these extremes is strongly dependent on the size and shape of its reinforcement. In general, as the aspect ratio of the reinforcement increases, the composite tends to exhibit increased amounts of fiber strengthening, but as particle size

or whisker diameter decreases, the composite will tend to be primarily strengthened by dispersion methods. With this in mind, an ideal composite may be one having a high aspect ratio, small diameter reinforcement, in that all strengthening mechanisms would be highly active. The following sections should serve to explain how reinforcement size and geometry affects the strengthening contributions by these mechanisms.   These calculations are based on a mean particle reinforcement size of 35 microns and the published properties for BaTiO$_3$, Cu- 10w% Sn bronze, and electroformed Ni shown in Table 4, Table 5, and Table 6.

Selected properties of ceramic BaTiO$_3$ are shown in Table 4.[22-24]

Table 4. Selected properties of ceramic BaTiO3

Modulus of Rupture, *MOR*	Elastic Modulus, *E*	Theoretical Density, ρ_{th}	Melting Temp. T_m	Piezoelectric Constant d_{33}	Electro-mechanical Coupling Factor, *k*	Coef. of Thermal Expansion α_l	Curie Temp. T_C
82 MPa	67 GPa	6.02 g/cm^3	1618 ^{o}C	191 pC/N	0.5	0.9x10^{-5} 1/^{o}C	130 ^{o}C

Selected properties of annealed Cu- 10w% Sn bronze are shown in Table 5.[25]

Table 5. Selected properties of Cu- 10w% Sn bronze

Yield Strength, σ_y	Tensile Strength, σ_T	Elastic Modulus, *E*	Density, ρ	Poisson's Ratio *v*	Melting Temp. T_m	Coef. of Thermal Expansion α_l	Electrical Resistivity at 20°C
195 MPa	455 MPa	110 GPa	8.78 g/cm^3	0.34	1000°C	1.84x10^{-5} 1/^{o}C	157 nΩ/m

Selected properties of electroformed sulfamate Ni are shown in Table 6.[26, 27]

Table 6. Selected properties electroformed sulfamate nickel

Yield Strength, σ_y	Tensile Strength, σ_T	Elastic Modulus, *E*	Density, ρ	Poisson's Ratio *v*	Melting Temp. T_m	Coef. of Thermal Expansion α_l	Electrical Resistivity at 20°C
538 MPa	758 MPa	207 GPa	8.90 g/cm^3	0.31	1453°C	1.31x10^{-5} 1/^{o}C	95 nΩ/m

Shear Lag Theory

The shear lag theory assumes that load transfer occurs between high aspect ratio reinforcement and the matrix by means of shear stresses at the particle-matrix interface. Through this mechanism, the particle acts to bear some of the applied load. The original model[28] of this mechanism only accounted for the shear transfer of load along the interface parallel to the applied load, but subsequent modifications have been made to account for the tensile transfer of load at the particle ends. This is important in dispersion strengthened composites, as its contribution tends to become more significant as the aspect ratio of the particle deceases.[29, 30] According to the modified shear lag theory, which assumes no slipping at the matrix/reinforcement (M/R) interface, the yield strength of a composite can be found using Eq 3.[30]

$$\sigma_c = \sigma_{ym}\left[1 + \frac{(L+t)S}{4L}\right]f + \sigma_{ym}(1-f)$$

Eq 3

Here σ_{ym} is the yield strength of the unreinforced matrix. L is the length of the particle perpendicular to the applied stress. t is the length of the particle parallel to the applied stress. S represents the particle aspect ratio, and f is the particle volume fraction. In the case of spherical or equiaxed particles $L \approx t$ and $S \approx 1$ reducing Eq 3 to Eq 4.[31]

$$\sigma_c = \sigma_{ym}\left(1 + \frac{1}{2}f\right)$$

Eq 4

This represents a linear and very modest increase in yield strength with increasing volume fraction. Upon comparison of Eq 3and Eq 4, the dependence on aspect ratio becomes apparent. Applying this relation, Figure 5 shows the dependence of yield strength vs. volume fraction reinforcement for both the Cu-10w%Sn (Figure 4) and the Ni (Figure 5) matrix composite systems reinforced with 35µm $BaTiO_3$ particles.
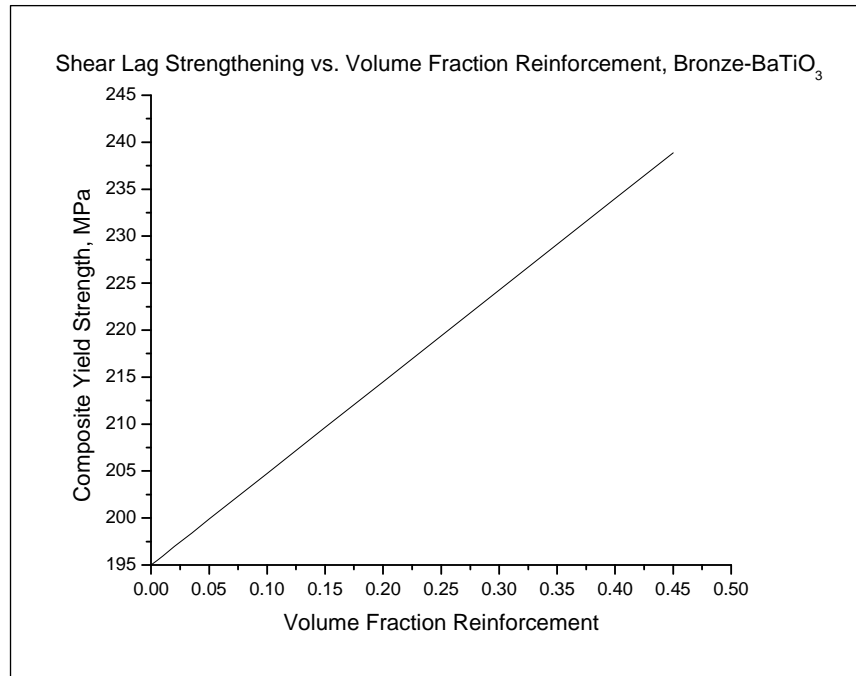
Figure 4. Calculated dependence of yield strength vs. volume fraction reinforcement according to the modified shear lag theory of the bronze-BaTiO3 composite system.
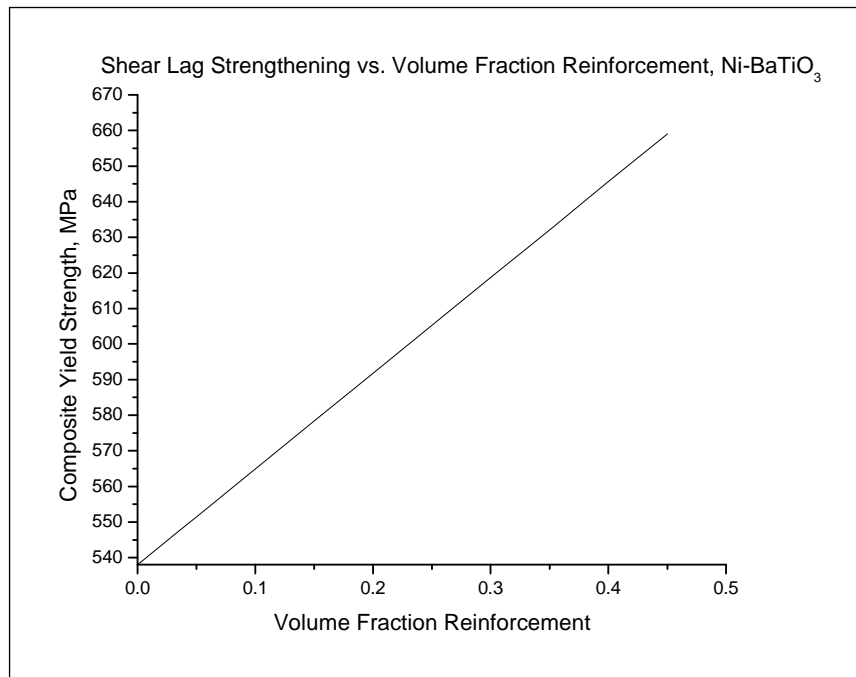
Figure 5. Calculated dependence of yield strength vs. volume fraction reinforcement according to the modified shear lag theory of the electroformed Ni-BaTiO$_3$ composite system.

In this work, this upward trend becomes dually important. Not only does it predict composite strengthening due to load transfer, but from the prediction of load transfer, one

can predict increased damping arising from the activation of damping mechanisms in the reinforcement by the transferred load.

Orowan Strengthening

Yielding in metals generally occurs through the process of dislocation motion. In composites containing small (<1μm), incoherent particles, inhibition of dislocation motion can arise as dislocations physically interact with the small reinforcement. With small impenetrable particles, a passing dislocation will bow between particles and finally pass by leaving behind an "Orowan" loop, as illustrated in Figure 6.
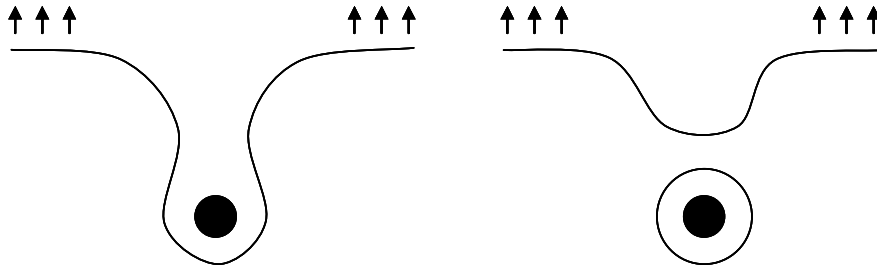
Figure 6. Formation of an Orowan loop as a dislocation bows around a particle

By increasing dislocation density through the creation of Orowan loops and by causing dislocations to increase in length, the presence of these small particles tends to increase the yield strength of the material. This was originally described by the Orowan relationship[21] which predicts the shear stress (τ) required for a dislocation to by-pass a particle and is shown in Eq 5.

$$\tau = \frac{Gb}{\lambda_{e-e}}$$
Eq 5

Here, G is the shear modulus of the matrix material; b is the operative Burger's vector, and λ_{e-e} is the edge-to-edge spacing of the particles. Ashby modified the above equation to account for diminished strengthening as the particle size approaches an atomic diameter. Further modification to normal stress in polycrystalline materials yields,[20, 31]

$$\sigma_c = \sigma_m + \frac{2.4 G_m b}{2\pi (1-v)^{1/2}} \frac{\ln \frac{2r}{r_o}}{\lambda_{e-e}}$$
Eq 6

or for rod and plate shaped reinforcement, Kelly and Street proposed a further modification.[32]

$$\sigma_c = \sigma_m + \frac{2.4 G_m \cdot b}{2\pi(1-\nu)^{1/2}} \frac{1 + \dfrac{L_T}{\lambda_{c-c}}}{\lambda_{c-c}} \ln\left(\frac{t}{r_o}\right)$$

Eq 7

In Eq 6 and Eq 7, the factor 2.4 comes from the product of the Taylor factor ($\approx$3), which relates shear to normal stresses, and a statistical/geometric factor, which discounts the overall strengthening effect that is possible. This discount is based on the fact that the wrapping of a dislocation around one particle inhibits its ability to fully wrap around and adjacent particle. Thus the adjacent particle cannot inhibit the motion of that dislocation to its fullest ability. This discounted ability has been calculated to be roughly 0.81.[20] Also, σ_c is the strength of the composite and σ_m is the strength of the matrix without reinforcement. G_m is the shear modulus of the matrix, which for isotropic matrices can be found using Eq 8.

$$G_m = \frac{E}{2(1+\nu)}$$

Eq 8

Here, ν is Poisson's ratio and E the elastic modulus of the matrix.

Referring back to Eq 8 and Eq 9, t is the thickness and L_T the total length of rod or plate reinforcement. b is the magnitude of the Burgers vector for deformation in the matrix, which for cubic matrices can be estimated as $b \approx 2(r_{ma})$, where r_{ma} is the atomic radius of the matrix. r_o represents the dislocation core radius which can be estimated as $r_o \approx 3b$. r is the average particle radius, and λ_{e-e} is the edge-to-edge particle spacing, which is approximated by Eq 9.

$$\lambda_{e-e} \approx \lambda_{c-c} - 2r$$

Eq 9

λ_{c-c} is the center-to-center particle spacing according to Eq 10.

$$\lambda_{c-c} \approx 1.23r \cdot \left(\frac{2\pi}{3f}\right)^{1/2}$$

Eq 10

Here, f is the volume fraction reinforcement.

The Ashby-Orowan Equation predicts increased strength with decreasing particles size and/or increasing volume fractions. This is particularly true for particles in the submicron range, but strengthening effects are still predicted but not expected to be dominant for particle sizes greater than 10μm. Figure 8 shows the predicted dependence of yield strength vs. volume fraction reinforcement according to Ashby-Orowan strengthening, for both the Cu-10w%Sn (Figure 7) and the electroformed Ni-BaTiO$_3$ (Figure 8) composite system addressed in this work.
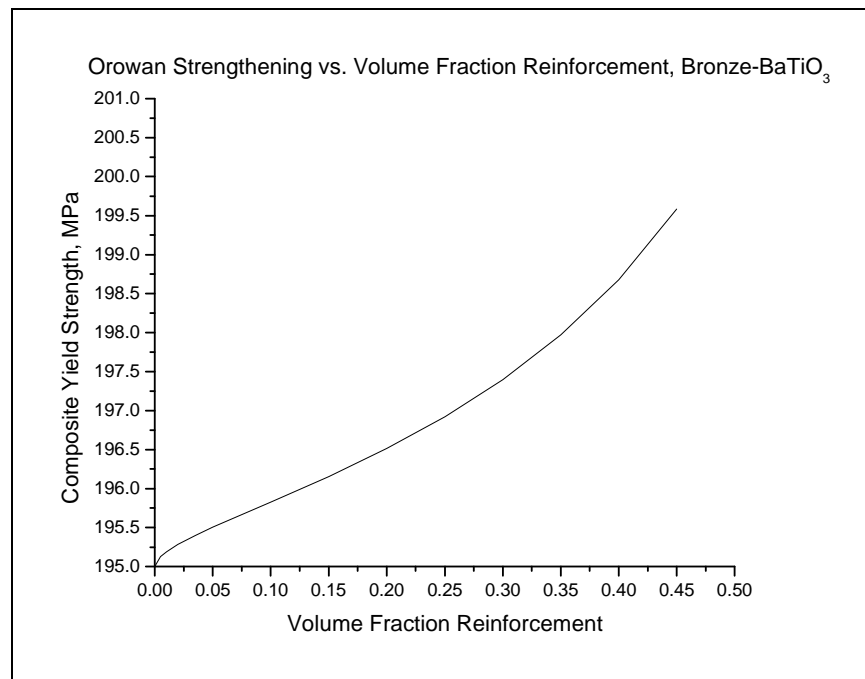
Figure 7. Calculated dependence of yield strength vs. volume fraction reinforcement according to Orowan strengthening of the bronze-BaTiO3 composite system.
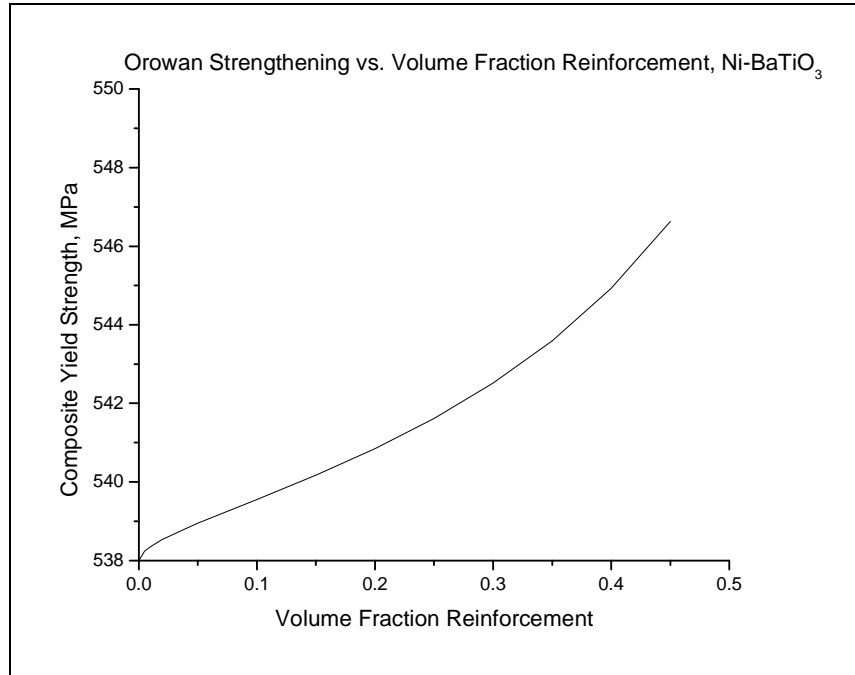
Figure 8. Calculated dependence of yield strength vs. volume fraction reinforcement according to Orowan strengthening of the electroformed nickel-BaTiO₃ composite system.

Due to the relatively large size of the particulate reinforcement (35μm), negligible Orowan strengthening is predicted for this system, however the scale has been expanded to better visualize the trend.

Boundary Strengthening

The Ashby-Orowan Equation predicts negligible strengthening in composites having coarse or widely-spaced reinforcement.[20] In such systems, an alternative mechanism of strengthening may be predominant, boundary strengthening. Again, yielding in metals occurs primarily through the creation and motion of dislocations, and this mechanism is based on crystallographic discontinuities or boundaries impeding this motion. When the reinforcement is added to the matrix, boundaries are formed. When the material is stressed, dislocations tend to pile-up at these incoherent interfaces increasing the overall dislocation density and thus strength of the material. This is similar to Hall-Petch strengthening in metals, which can simultaneously occur in the matrix due to grain refinement.[20]

There are four different equations used to model boundary strengthening. These are based on the shear "impingement" stress ($\tau_{boundary}$) from the matrix at the matrix/reinforcement (M/R) boundary and also the shear properties of the matrix (τ_{matrix}) and reinforcement ($\tau_{reinforcement}$). This behavior can be difficult to predict, so often composites are stressed to failure and examined to determine which equation to use.

If the particle has fractured, then $\tau_{boundary} > \tau_{reinforcement\text{-}fracture}$, and Eq 11 is used to calculate composite strength (σ_c).

$$\sigma_c = \sigma_m + \alpha' \sqrt{\frac{G_m G_p b}{5 \lambda_{e-e}}}$$

Eq 11

If the matrix has fractured, then $\tau_{boundary} > \tau_{matrix\text{-}fracture}$, and Eq 12 is used to calculate σ_c.

$$\sigma_c = \sigma_m + \alpha'' \sqrt{\frac{G_m^2 b}{5 \lambda_{e-e}}}$$

Eq 12

If the particle has yielded, then $\tau_{reinforcement\text{-}fracture} > \tau_{boundary} > \tau_{reinforcement\text{-}yield}$, and Eq 13 is used.

$$\sigma_c = \sigma_m + \alpha''' \sqrt{\frac{G_m G_p b}{10 \lambda_{e-e}}}$$

Eq 13

If the particle has neither fractured nor yielded, then $\tau_{reinforcement\text{-}fracture} \gg \tau_{reinforcement\text{-}yield} \gg \tau_{boundary}$, and Eq 14 is used utilized.

$$\sigma_c = \sigma_m + \alpha'''' \sqrt{\frac{G_m E_p b}{10 \lambda_{e-e}}}$$

Eq 14

In Eq 11-Eq 14, σ_m is the matrix strength without reinforcement. G_m and G_p are the shear moduli of the matrix and particle. E_p is the elastic modulus of the particle. b represents the Burger's vector for deformation in the matrix. λ_{e-e} is the edge-to-edge particle spacing from Eq 9, and α is used as a fitting parameter with a value approximately equal to one.

The presence of α is an acknowledgement that the equations are predictive and that there are other factors which may influence the actual value of strength obtained through experiment. In Eq 11-Eq 14, the trend shown in Eq 15 is generally true.[17]

$$\alpha^{''''} > \alpha^{'''} > \alpha^{''} > \alpha^{'}$$

<div align="right">**Eq 15**</div>

For both the Cu-10w%Sn and the electroformed nickel-BaTiO$_3$ systems studied in this work, the BaTiO$_3$ reinforcement is expected to fracture upon testing based upon its low strength. Therefore $\tau_{boundary} > \tau_{reinforcement-fracture}$ and Eq 11 might be used to calculate the composite strength. However, this cannot be verified through experiment as the reinforcement particles are already heavily cracked due to processing conditions. In cases such as this when the failure conditions cannot be determined, an underestimate of the boundary strengthening behavior can be found utilizing the experimentally determined Hall-Petch behavior of the matrix material. This is done, by combining the Hall-Petch equation,[27] where k_{H-P} represents the Hall-Petch constant and d the grain diameter,

$$\sigma_c = \sigma_m + k_{H-P}\sqrt{\frac{1}{d}}$$

<div align="right">**Eq 16**</div>

with the equations for boundary strengthening. In Eq 11-Eq 14, the modulus and Burger's vector terms inside the square root along with the factor of 5 or 10 represent the mechanical mismatch between the matrix and the reinforcement. Large values of this term signify that the reinforcement particles are rigid with respect to the matrix, and thus would act as strong barriers to dislocation motion. This is analogous to the Hall-Petch constant which describes the rigidity of grain boundaries, as compared to the interior of grains, and their ability to impede dislocation motion. Thus a substitution can be made in Eq 11-Eq 14 resulting in Eq 17, where k_{H-P} represents the Hall-Petch constant for the matrix material.

$$\sigma_c = \sigma_m + \alpha k_{H-P}\sqrt{\frac{1}{\lambda_{e-e}}}$$

<div align="right">**Eq 17**</div>

Here, α remains as a fitting parameter with a value approximately equal to one, and $\lambda_{e\text{-}e}$ is the edge to edge spacing between the particles. This distance, as with *d* from Eq 16, represents the spacing between obstacles to dislocation motion in the material.

As mentioned earlier, the calculation of strengthening effects using Eq 17 usually leads to an underestimate of true strengthening behavior. This is due to the fact that in most composite systems reinforcement particles are much better barriers to dislocation motion than are grain boundaries in a material. In the case of the bronze-$BaTiO_3$ system, the $k_{H\text{-}P}$ for Cu (0.112 $MNm^{-3/2}$)[33] is used to calculate boundary strengthening effects, and this has been plotted vs. reinforcement volume fraction as shown in Figure 9.

Boundary Strengthening vs. Volume Fraction Reinforcement, Bronze-$BaTiO_3$
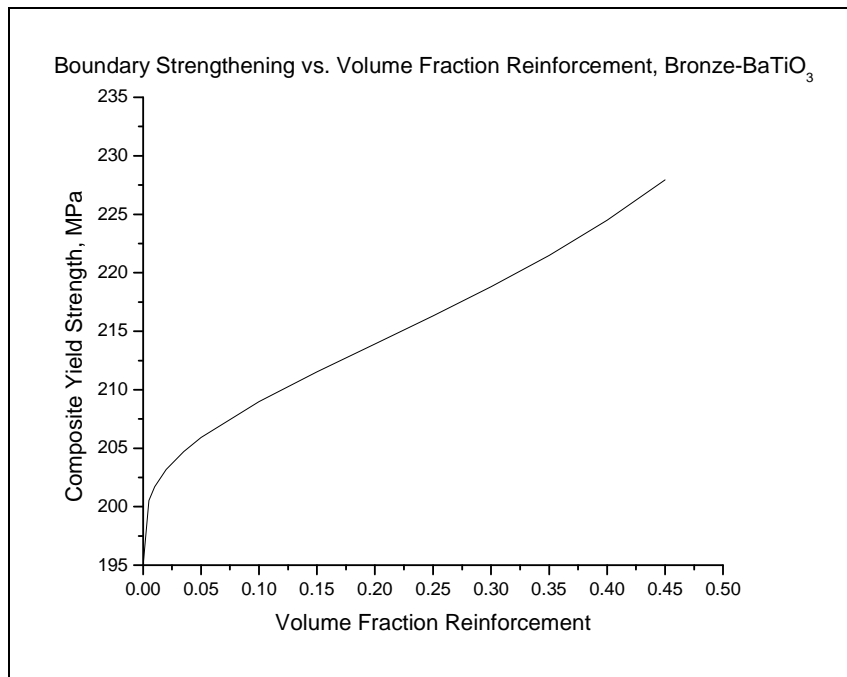
Figure 9. Calculated dependence of yield strength vs. volume fraction reinforcement according to boundary strengthening of the bronze-BaTiO3 composite system.

For the Ni-$BaTiO_3$ system, the $k_{H\text{-}P}$ for Ni (0.13 $MNm^{-3/2}$)[33] is used to calculate boundary strengthening effects, and this has been plotted vs. reinforcement volume fraction as shown in Figure 10.
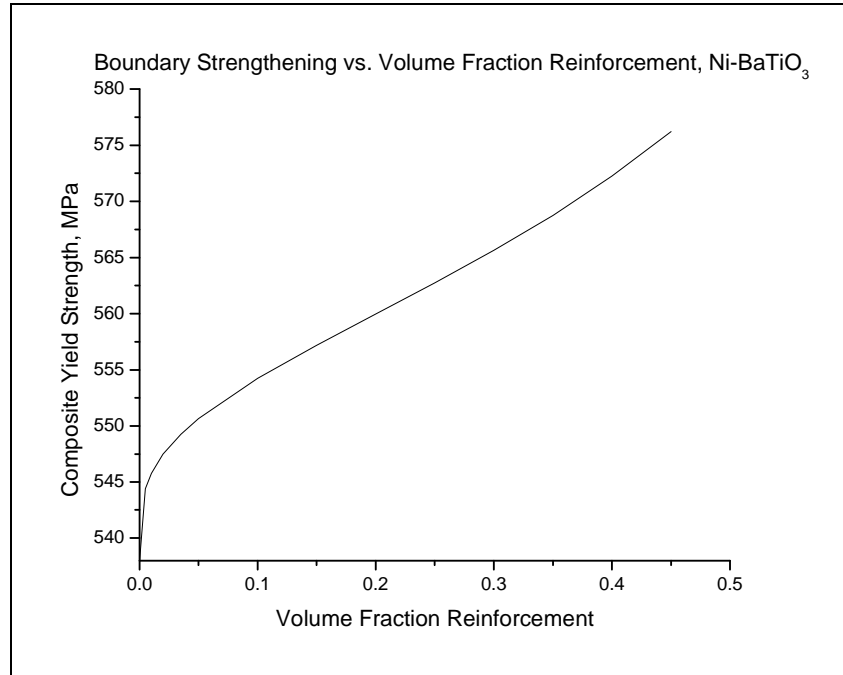
Figure 10. Calculated dependence of yield strength vs. volume fraction reinforcement according to boundary strengthening of the Ni-BaTiO$_3$ composite system.

Coefficient of Thermal Expansion Mismatch

Dislocation strengthening of the matrix due to thermal expansion mismatch between the matrix and reinforcement, can also play an important role in MMC strengthening.[34] The residual stress developed due to the difference in coefficient of thermal expansion between the matrix and reinforcement (ΔCTE) can be large enough to induce plastic relaxation in the matrix. This can increase dislocation density by a few orders of magnitude in the matrix leading to the strengthening of the composite.[35] The composite strength (σ_c) can be predicted by this mechanism using Eq 18,[17]

$$\sigma_c = \sigma_m + \alpha G_m \left(\frac{2 f \varepsilon_{\Delta CTE}\, b}{(1-f)} \frac{S}{V} \right)^{\frac{1}{2}} \qquad \textbf{Eq 18}$$

or with Eq 19[17] for cylindrical reinforcement.

$$\sigma_c = \sigma_m + \alpha' G_m \left(\frac{2 f \varepsilon_{\Delta CTE}\, b}{(1-f)} \frac{1}{t} \right)^{\frac{1}{2}} \qquad \textbf{Eq 19}$$

Here, σ_m is the matrix strength without reinforcement. Again, α is used as a fitting parameter as in Eq 11-Eq 14 with a value approximately equal to one. As before, G_m is the shear modulus of the matrix; f represents the volume fraction of reinforcement, and t is the reinforcement thickness. b is the Burger's vector for deformation in the matrix, which can be estimated for cubic matrices as approximately the atomic diameter. S/V is the surface to volume ratio, and $\varepsilon_{\Delta CTE}$ is predicted using Eq 20,[17]

$$\varepsilon_{\Delta CTE} \approx \frac{(\Delta CTE)(\Delta T)}{2}$$

Eq 20

where ΔT is the temperature change upon cool-down during processing or heat treatment. For the bronze-BaTiO$_3$, system this was based on the 820° sintering temperature used for consolidation.

For the bronze-BaTiO$_3$, ΔCTE strengthening has been calculated for equiaxed BaTiO$_3$ and plotted vs. reinforcement volume fraction. This is shown in Figure 11.
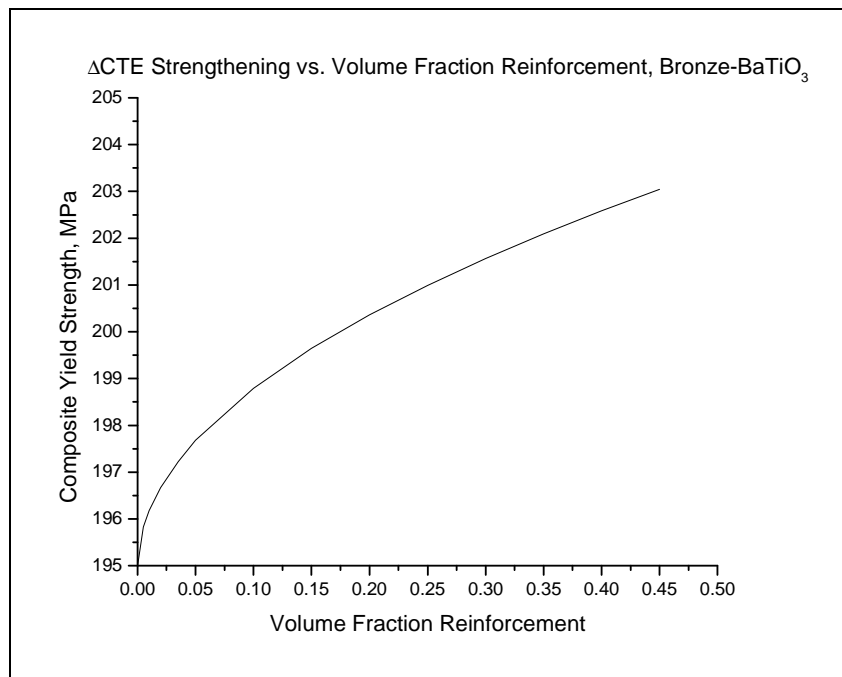
Figure 11. Dependence of yield strength vs. volume fraction reinforcement according to ΔCTE strengthening of the bronze-BaTiO3 composite system.

For the Ni-BaTiO$_3$, ΔCTE strengthening has been calculated and plotted vs. reinforcement volume fraction. This is shown in Figure 12.
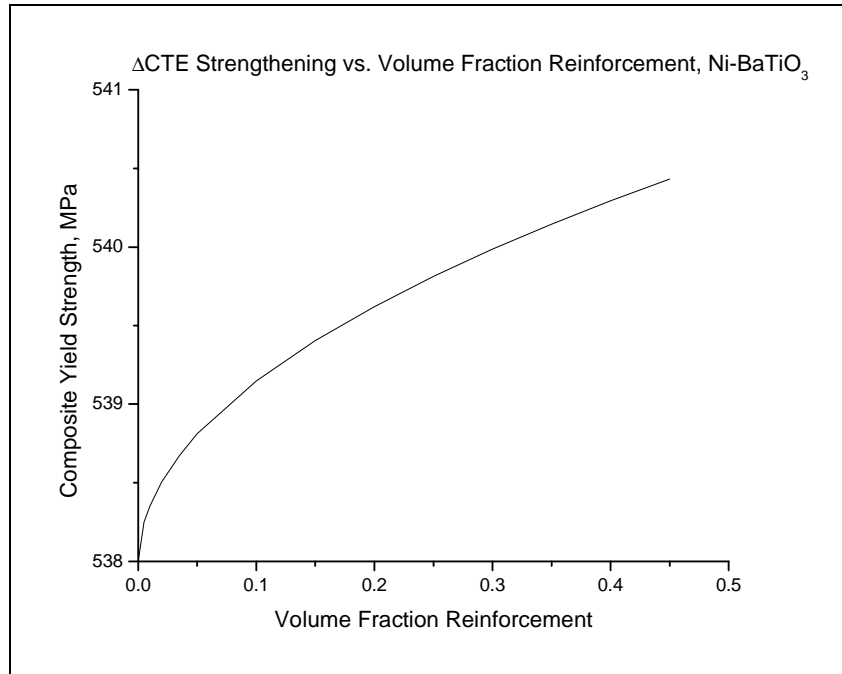
Figure 12. Dependence of yield strength vs. volume fraction reinforcement according to ΔCTE strengthening of the Ni-BaTiO$_3$ composite system.

This was modeled based on cooling from the electroforming temperature of 70^0C, and as with Orowan strengthening, the ΔCTE mechanism is not predicted to have a large effect on the strength of either system.

Indirect Strengthening Mechanisms

Metal matrix composites can also be strengthened by mechanisms indirectly related to reinforcement addition. These indirect effects often stem from changes made to the matrix through reinforcement addition. Especially in the case of small particulates, the reinforcement can cause grain refinement in the matrix leading to strengthening through Hall-Petch mechanisms as previously mentioned. Primary or secondary recrystallization can also be initiated through reinforcement addition. Dissolution of the reinforcement or the formation of reaction layers at the M/R interface can also lead to strengthening or weakening in the matrix. These secondary effects will not be addressed in this work.

2.2 Additivity of Strengthening Mechanism Effects in Metal Matrix Composites

Figure 13 compares the effects of each of the previously mentioned direct strengthening mechanisms.
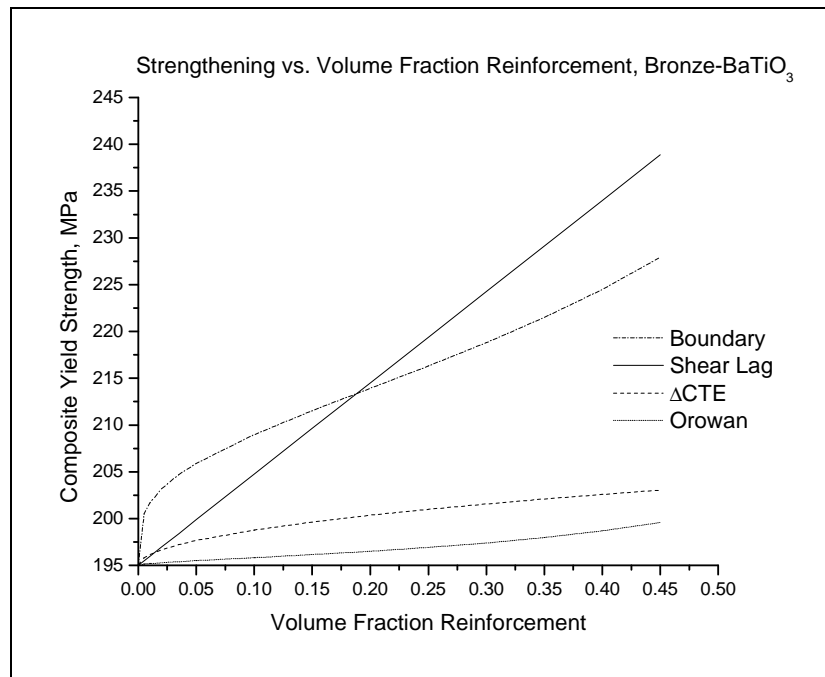
Figure 13. Dependence of yield strength vs. volume fraction reinforcement according to shear lag, Orowan, boundary, and ΔCTE strengthening of the bronze-BaTiO3 composite system.

Figure 14 compares the effects of each of the previously mentioned direct strengthening mechanisms for the Ni matrix system.
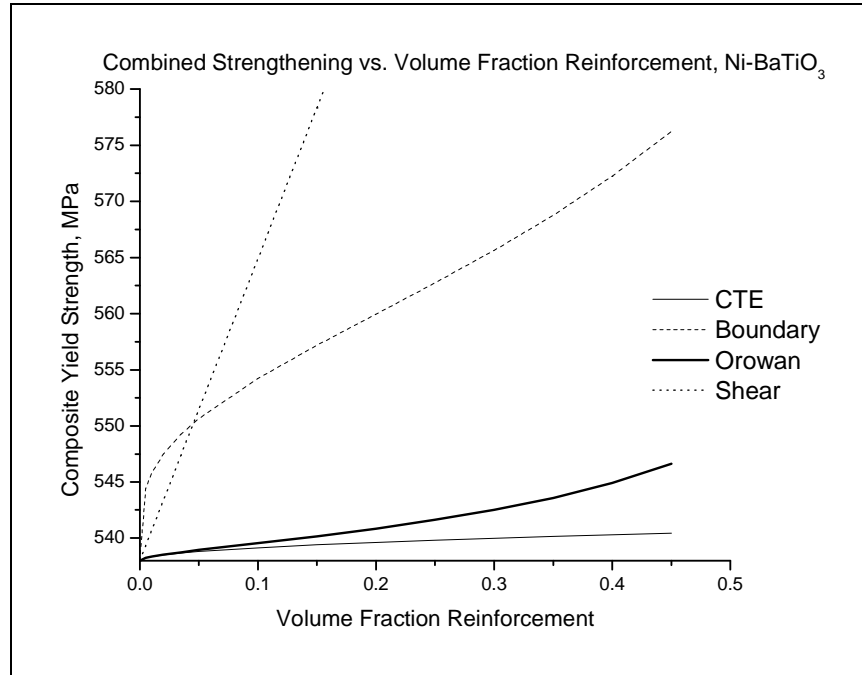
Figure 14. Dependence of yield strength vs. volume fraction reinforcement according to shear lag, Orowan, boundary, and ΔCTE strengthening of the Ni-BaTiO₃ composite system.

In general, these strengthening effects are all active in a composite at the same time leading to a combined effect on composite strength. Interdependency of these strengthening mechanisms however leads to the prediction of composite strength using an upper and lower bounds.

The upper bound assumes that each mechanism strengthens independently and combines their effects using linear additivity. This is shown in Eq 21.

$$\sigma_c = \sigma_m + \Delta\sigma_{ShearLag} + \Delta\sigma_{Orowan} + \Delta\sigma_{Boundary} + \Delta\sigma_{\Delta CTE} \qquad \textbf{Eq 21}$$

The lower bound assumes strong interdependence of the mechanisms using Pythagorean additivity, as shown in Eq 22.

$$\sigma_c^2 = \sigma_m^2 + \Delta\sigma_{ShearLag}^2 + \Delta\sigma_{Orowan}^2 + \Delta\sigma_{Boundary}^2 + \Delta\sigma_{\Delta CTE}^2 \qquad \textbf{Eq 22}$$

The predicted upper and lower bounds of the composite yield strength vs. volume fraction reinforcement can be seen in Figure 15 for the bronze-BaTiO₃ system.

Combined Strengthening vs. Volume Fraction Reinforcement, Bronze-BaTiO$_3$
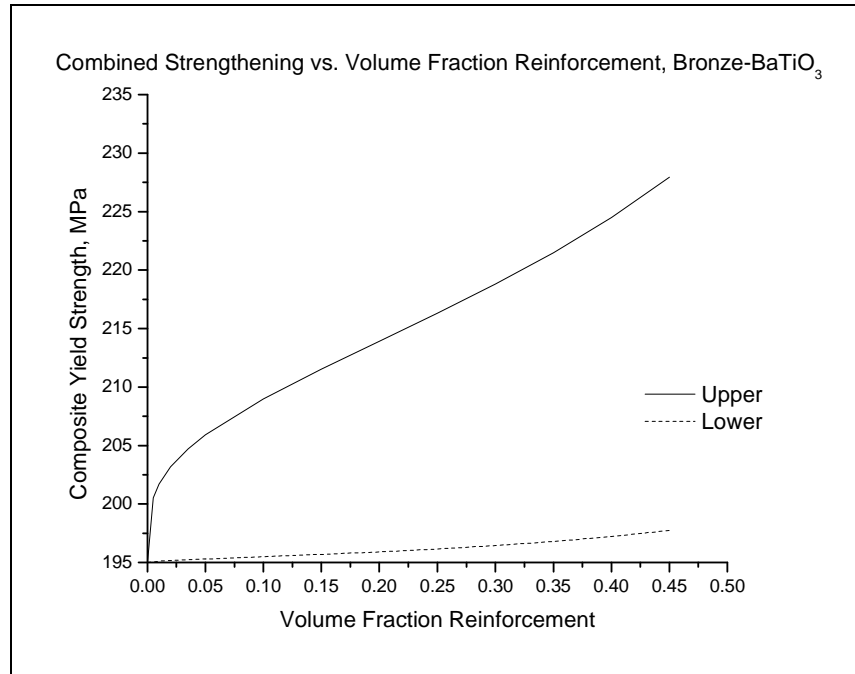
Figure 15. Dependence of yield strength vs. volume fraction reinforcement according to the combined strengthening mechanisms of the bronze-BaTiO3 composite system.

The predicted upper and lower bounds of the composite yield strength vs. volume

fraction reinforcement can be seen in Figure 16 for the Ni-BaTiO$_3$ system.
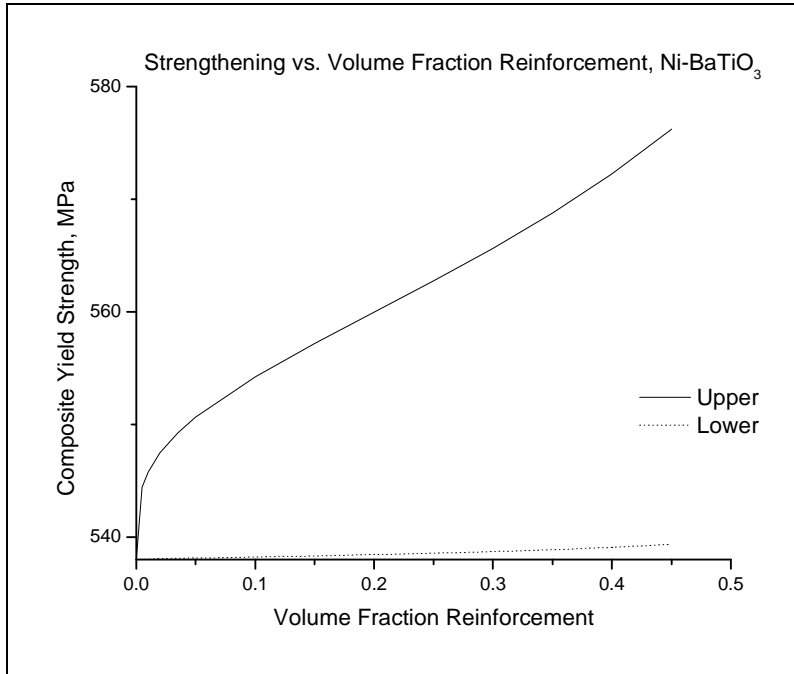
Figure 16. Dependence of yield strength vs. volume fraction reinforcement according to the combined strengthening mechanisms of the Ni-BaTiO$_3$ composite system.

2.3 Damping Mechanisms in Metal Matrix Composites

The damping ability of a MMC is generally greater than a simple volume fraction combination of the abilities of its constituents. This is due to a number of additional damping mechanisms involved in composite systems. This is particularly true if the matrix/reinforcement (M/R) bonding is poor. Interfacial damping mechanisms, such as frictional sliding or stress induced diffusion across the interface, are both potential energy-absorbing processes. Also, when an elastic wave strikes an imperfectly bonded interface, the imperfect transfer of elastic energy can lead to interfacial heating.

Further increases in damping ability can be attained when the presence of one constituent increases the inherent damping ability of another. In the matrix as in unreinforced metals, the local movement of dislocations can serve to dissipate energy. This occurs as they escape from pinning points, vibrate and/or relax into local low energy configurations. The main difference in MMCs is that as a consequence of CTE mismatch between the matrix and reinforcement or of the presence of Orowan loops, dislocation

density is usually greater and dislocations are more efficiently pinned or tangled. Also in the matrix, as in unreinforced metals, grain boundary sliding can occur. This is further increased in MMCs however, due to the refinement of grain size induced by the reinforcement.

In MMCs, the matrix and interface are not the only sources of damping. Since some degree of stress is usually transferred to the reinforcement, all of the reinforcement's inherent damping mechanisms can be active. In the case of this work, the damping ability of $BaTiO_3$ is being used to increase the overall damping ability of both the bronze and the electroformed nickel matrices.

3. Ferroelectric Materials

Ferroelectrics are group of dielectric materials which exhibit spontaneous polarization, that is, polarization in the absence of an electric field. They are the dielectric analogue of ferromagnetic materials, which may display permanent magnetic behavior. In ferroelectric materials, there must exist permanent electric dipoles, which are capable of switching polarity in the presence of an electric field. The origin of this will be explained later using barium titanate ($BaTiO_3$) as an example.

3.1 Piezoelectricity

There are 32 classes or point groups of crystalline materials. Of these, 11 are centrosymmetric and contain no polarity. Therefore the center of negative charge coincides with the center of positive charge. This remains true even under stress, so this type of crystal is termed paraelectric. Of the remaining 21 non-centric crystals, 20 have one or more axes along which when stressed exhibit the piezoelectric effect.[36] Piezoelectricity is the ability to develop an electric charge proportional to a mechanical stress.

3.2 Curie Temperature

As mentioned previously, piezoelectricity is dependent on crystal structure, so in piezoelectric materials, phase changes are very important. During a phase change a non-piezoelectric (paraelectric) phase may become piezoelectric or vice versa, and the temperature at which such phase change occurs is known as the Curie point or Curie temperature (T_C).

Barium titanate ($BaTiO_3$) is given as an example in Figure 17.
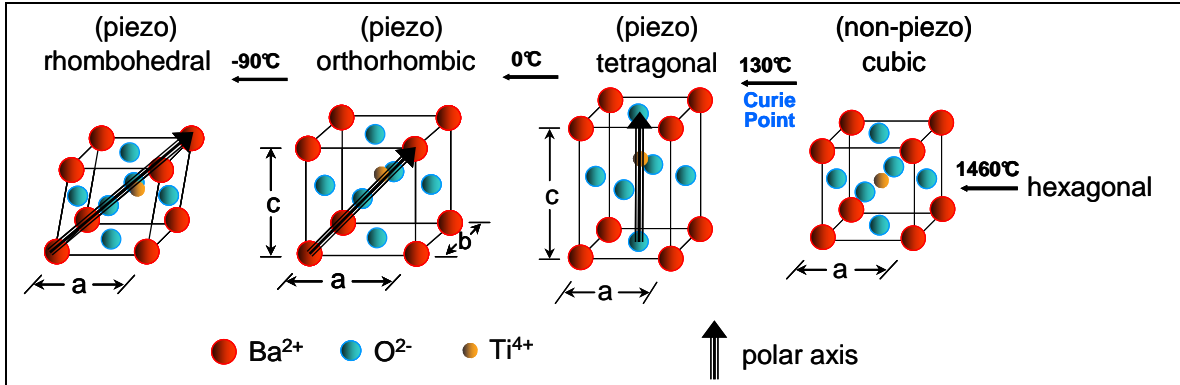
Figure 17. Crystal phases of barium titanate

From the figure it can be seen that the Curie point of $BaTiO_3$ is at ~130°C, where there is a phase change between the piezoelectric tetragonal phase and the paraelectric cubic phase.

3.3 Pyroelectricity

Of the 20 piezoelectric crystal classes, 10 contain at least one spontaneous polar axis in the unit cell, i.e. an axis which shows properties at one end different from those at the other. This polarization is spontaneous in that it exists without external influence, such as an electric or stress field. Crystals of this type are deemed pyroelectric, due to the fact that the magnitude of this spontaneous polarization (P_s) varies with temperature until heated through T_C.

In order to minimize energy, polarized unit cells arrange themselves in likely oriented groups called domains.[22, 37, 38] The size and arrangement of these domains is the result of two competing energies, the domain wall energy and the depolarization energy of the surroundings (E_{dp}).[38] To explain this further, imagine a pyroelectric single crystal consisting of many polarized unit cells aligned in the same direction as seen in Figure 18.

30
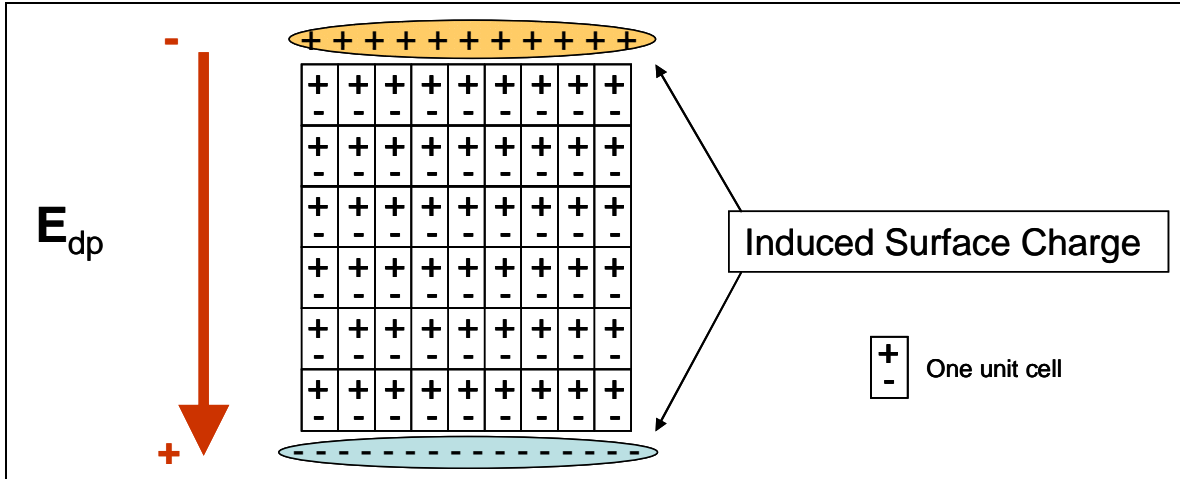
Figure 18. Charge arrangement in a single crystal pyroelectric

In this state, the crystal would have one single domain. In this domain, the net polarization of the like-oriented unit cells creates a net polarization across the crystal. Since the crystal is polarized, surface charges are induced on its surface. The surface charges create a depolarizing electric field (E_{dp}) whose energy is proportional to the volume of the crystal and the square of the polarization.[36] Here E_{dp} is essentially the result of the resistance of the surroundings to become polarized; thus, the aligned single domain state which opposes the depolarizing field is a very high energy state for the crystal.

To avoid this high energy state, the unit cells arrange themselves into several domains. The domains themselves remain polarized, but their antiparallel arrangement causes the overall net polarization of the crystal to approach zero, as in Figure 19. At this point, although the individual unit cells are of a piezoelectric class, the crystal as a whole will not exhibit the piezoelectric effect.
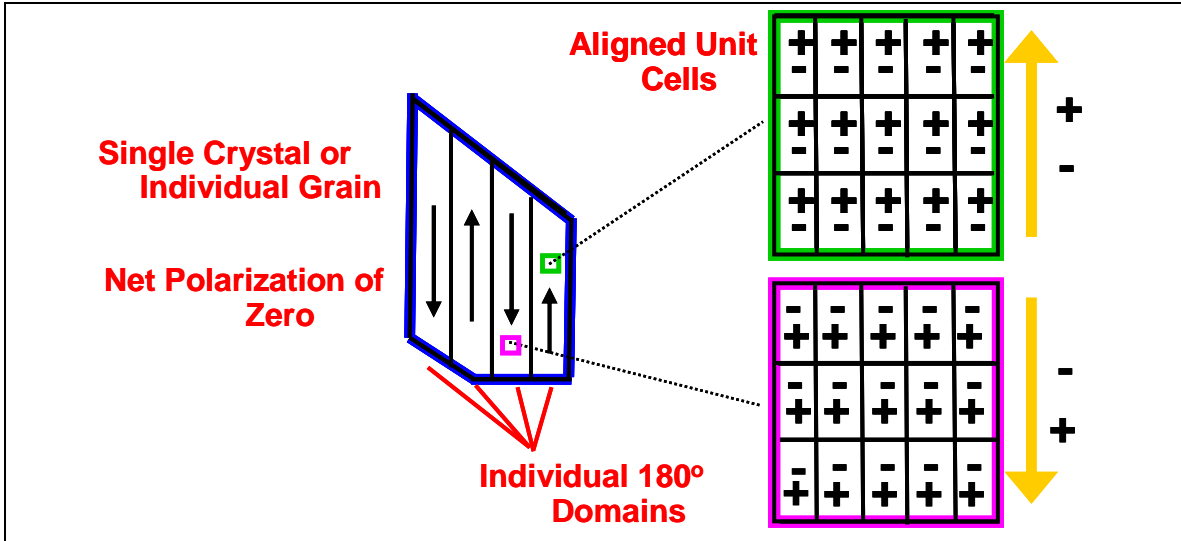
Figure 19. Antiparallel domains

This arrangement occurs upon normal cooling through the Curie temperature (T_C). As the pyroelectric phase nucleates, the 180° ferroelectric domains arrange to minimize the overall electrostatic energy state[38-40] i.e., to minimize the overall polarization. A minimum energy state, however, cannot generally be achieved through 180° domain formation alone. Local thermal stresses also affect domain formation creating 90° ferroelastic domains in the form of twins within the 180° domains. These 90° domains serve to stabilize the tetragonal phase by relieving compressive stress while maintaining overall neutral polarity along the polarized axis of the material,[38-40] Figure 20.
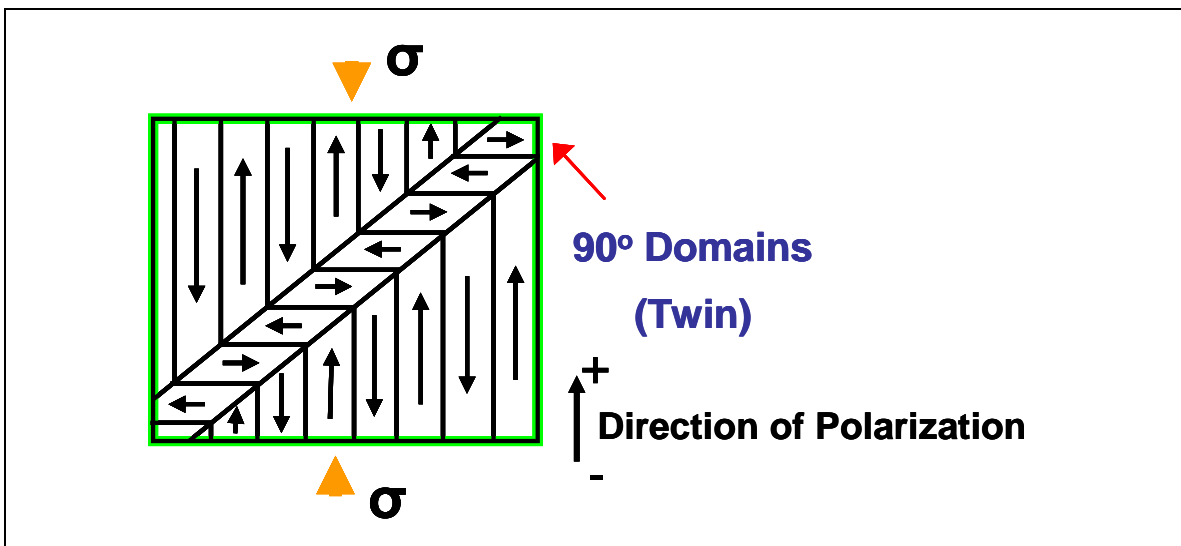
Figure 20. A twin (90° ferroelastic domains) across the 180° domains

As an increasing number of domains are formed and rearranged, energy is stored in the boundaries or "walls" between then. At the same time though, the energy of the crystal is lowered as its net polarization and internal stress are reduced. An actual resulting domain structure, is seen in Figure 21, showing the metastable compromise reached as domain mobility drops off with temperature from its peak at T_C.
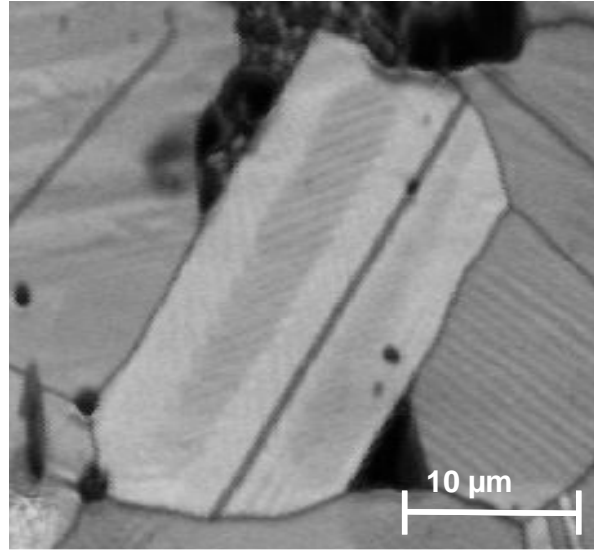
Figure 21. Antiparallel domains showing unit cell and domain wall placement

This same process occurs in the individual grains of polycrystalline pyroelectrics, with each grain consisting of its own multi-domain structure.

3.4 Poling

Poling is the process of using an external force to bias the alignment of the polar axes in a multi-domain material. In the case of pyroelectrics, this force is usually in the form of an electric field. If a DC electric field is applied to a pyroelectric crystal having several randomly oriented domains, each of the domains contained in the crystal will show a tendency to align in the direction of the applied field (E_{app}). This realignment of domains takes place by way of nucleation and domain wall motion, which comes at an energy cost overcome by E_{app}.

One common example of a poling device is a capacitor in which the pyroelectric acts as the dielectric material between the electrodes. When poling large ceramic samples, two thin layers of conductive material are plated onto the sample at opposite ends. These layers are used as electrical contacts for the positive and negative electrodes of the poling device. Once an electric field of sufficient magnitude is created across the pyroelectric, its random domains align, creating a piezoelectric material. Consequently, it is along the axis of polarization that the poled material will exhibit maximum piezoelectric properties.

3.5 Ferroelectricity

Within the 10 pyroelectric crystal classes, there exists a subset of materials known as ferroelectrics. Ferroelectrics are materials whose spontaneous polar axes can be reversed 180° with the application of an electric field. This property, known as switching, allows for greater ease and quality of poling. Through this phenomenon, existing antiparallel domains can simply reverse their orientation to align with the applied electric field. This facilitates domain reorientation with a lesser dependence on the higher energy mechanisms previously mentioned. The result is that, in general, bulk ferroelectric materials can be more readily made piezoelectric and with a larger degree of remnant polarization than other pyroelectric materials. The $BaTiO_3$ utilized for this study is a ferroelectric material, however since applied stress generally does not cause ferroelectric domain switching; it is actually the pyroelectric nature of $BaTiO_3$ which leads to its high-damping properties. In the literature though, $BaTiO_3$ and other pyroelectric materials are better know for their ferroelectric properties and are commonly termed "ferroelectrics" regardless of their application. Thus the author has chosen to stick with the classification of $BaTiO_3$ as a ferroelectric to avoid confusion.

3.6 Damping by Ferroelastic Domain Motion

As previously mentioned, stress can have an effect on domain structure and orientation. External or internal stresses can cause the formation of 90° ferroelastic domains, which form through the twinning of existing 180° ferroelectric domains.[38,40, 41] As this occurs, a

portion of the applied stress energy is dissipated, as it is utilized for domain reorientation. In the case of a cyclic applied stress, as with vibrational energy, the induced twinning is also cyclic. With each cycle, energy is dissipated, effectively damping the vibrational stress.   When the external stress is relieved the majority of the induced twins (90° domains) will disappear by relaxing back to the initial 180° domain structure. Those twins which remain are considered irreversible and will not further contribute to damping once activated as they have become immobile. This irreversibility is generally caused by pinning of the twins by grain boundaries, by other twins, or by oxygen vacancies which disrupt the tetragonal domain structure.[38, 41, 42]

In work performed by this group, this mechanism has been proven to play a large role in the damping ability of FR-MMCs.[2, 4, 43, 44] It should be noted however, that this effect is sensitive to the existing domain structure and material grain size. This is a direct result of the limiting effect on domain wall motion of grain boundaries in materials having grains smaller than 1μm.[1, 40]

4. Neutron Diffraction

In order to fully characterize a material or material system, it is often beneficial to see "inside" the system.   This is often attempted through sectioning of the material and observation through either optical or electron microscopy of the newly exposed surface. These methods however, are destructive to the sample and preclude in-situ characterization. Using these destructive methods, the true interior of the sample is not observed, but rather a newly created surface which has been altered by the cutting method itself and exposure to the environment. Neutron diffraction is a nondestructive technique that has become increasingly popular surface and bulk material characterization technique.

In the medical field and others involving the use of low density or "soft" materials, x-rays are generally used as a nondestructive means to view the interior of a material or system. X-rays, like light and electrons, interact with and are scattered by the electrons in the sample. Because of this, the penetration depth of x-rays at a given energy is determined by the material's physical density which directly translates to electron density in that material. This is why in medical x-rays the soft tissues appear transparent and the bone structures do not. By increasing the x-ray energy, one can look further into bulk materials as this energy enables increased x-ray penetration. However, this brute force method can damage or alter the sample while it is in the x-ray beam. In some large scale facilities, however, high energy x-rays are currently being utilized to peer inside materials, especially for those that cannot be imaged with neutron techniques.

Neutrons have no charge and thus have minimal interaction with the electrons of a material. Neutron interaction with matter is generally limited to scattering by nuclear rather than electrical forces, and nuclear forces are very short ranged, which are generally on the order of 10^{-15} meters.[45] Thus, matter appears less dense to neutrons than their electron interacting counterparts. Due to this, neutrons can penetrate much further into matter and at much low energies. As an example, the attenuation or decrease in intensity of a beam of low-energy neutrons by aluminum is about one percent per millimeter

(1%/mm) compared with 99 percent or more per millimeter (99+%/mm) for x-rays. The high penetrating power of neutrons is actually so great that in most cases their energy must be decreased so that they can be scattered by the material and not damage or pass straight through, and even then they are only weakly scattered by the material. This, coupled with the fact that neutron sources are of relatively low intensity as compared to x-ray sources, lead to much longer run times (hours versus seconds) when characterizing a sample using neutrons versus x-rays. Thus, in many cases it can be useful to utilize both techniques to fully characterize a given system.

4.1 Neutron Production

Unlike x-ray diffraction which can be done by a single unit and is commonly available, the production, distribution, and diffraction of neutrons generally requires an entire facility. Those that exist are generally located at government laboratories or large universities. All of these facilities generate neutrons either with nuclear reactors or with high energy particle accelerators. The neutrons produced have energies up to tens or even hundreds of mega-electron volts (MeV). Upon production, this high energy involves wavelengths far too short for interaction with condensed matter and neutron energies above a few electron volts can knock atoms from their structural positions, damaging the material. To be made useful, neutrons must be "cooled" to decrease their energy and increase their wavelength. This is done by passing them through a moderating material. This "moderator" must have a large scattering cross section, such as liquid water, and is placed near the neutron source. As the neutrons enter the moderator they go through a series of collisions with the moderator atoms, gradually losing energy, and being emitted as thermal neutrons having an average energy determined by the temperature at which is maintained in the moderator material through external cooling. The average energy of neutrons from a water moderator at ambient temperatures is about 0.025 eV which corresponds to a wavelength of 0.18 nanometers, which is of the same order as typical interatomic distances, making them suitable for diffraction experiments.[45]

37

Reactor Sources

In a nuclear reactor, neutrons are produced by fission of the atoms of the reactor fuel. These neutrons are emitted in a continuous, broad spectrum, high energy stream. After moderation, this spectrum must be made monochromatic to be useful for most diffraction experiments. Here, only neutrons in a single, narrow energy band are selected from the spectrum. This selection is usually accomplished through Bragg reflection from a large single crystal of a highly reflective material, such as pyrolytic graphite, germanium, or copper.[45] The incident neutron beam is reflected off of the crystal monochromator at a specific scattering angle, 2θ. Since the planer spacing of the atoms (d) of the monochromator is fixed, the scattering angle can be adjusted satisfying the Bragg equation, which will be addressed further in section 4.2, to transmit neutrons only of a specific wavelength.

Spallation Sources

Spallation sources utilize particle accelerators to produce spallation neutrons. Here, high-energy charged particles (protons or electrons) are accelerated to hundreds of MeVs and directed into a heavy-metal target, such as tungsten or uranium, freeing neutrons from the nuclei of the target. Unlike the constant flow from a reactor source, spallation neutrons arrive in pulses. This avoids the need for a crystal monochromator, and thus all neutrons produced can be utilized after moderation.

What allows the use of all neutrons from a spallation source is the measurement of the time it takes for each detected neutron to traverse the distance between the moderator and the detector. Using this time of flight method, the neutron velocity can be determined, and knowing its velocity, its wavelength can be determined using Eq 23,

$$\frac{hk}{2\pi} = mv \qquad\qquad\qquad \textbf{Eq 23}$$

Where *h* is Planck's constant, *m* is the mass of the neutron (1.67495x10^{-27} kilograms), *k* is the neutron's wave vector whose magnitude is $2\pi/\lambda$ pointing along its trajectory, and *v* is the neutron's velocity vector.

A thermal neutron with an energy of 25 meV has a velocity of about 2.2 km/s,[46] and a typical neutron spectrometer is roughly 10 meters long leading to a travel time of about 5 milliseconds. With the each neutron pulse lasting a few tens of microseconds, the time of flight of the neutrons can be determined with high relative precision.

4.2 Bragg Scattering

As was previously mentioned, neutrons are uncharged particles and thus have limited interaction with electrons. This is the main reason for the great penetration depth of neutrons into most materials, as interaction is dependent on nuclear forces and atomic nuclei make up only a very small portion of the total volume of matter. This nuclear interaction is in the form of neutron scattering from the nucleus, which can be either coherent or incoherent. With incoherent scattering each incident neutron wave has a random, or indeterminate, relative phase and acts independently with each nucleus in the sample, so that the scattered waves from different nuclei do not interfere. Instead the intensities from each scattering event just add up and can provide information on atomic diffusion.

With coherent scattering the incident neutron wave interacts with all the nuclei in the material in a coordinated fashion. The scattered waves from all the nuclei have definite relative phases as the neutron wave can interact with the whole sample as a unit so the scattered waves from different nuclei interfere with each. This scattering depends on the relative atomic distances and thus gives information about the structure of the material.

The simplest type of coherent neutron scattering is diffraction or Bragg scattering. Imagine a crystalline solid where atoms are arranged at fixed positions on a lattice and a beam of neutrons is incident on that lattice. We imagine that this lattice is far enough

removed from the source that all neutrons move on parallel paths and have the same velocity. The atomic nuclei are assumed to be fixed and there is no change in the neutron's energy during scattering. As the incident wave contacts each atom, that atomic site becomes the center of a scattered spherical wave emanating from that site having a definite phase relative to all other scattered waves. This circular wave spreads outward overlapping other spherical waves.
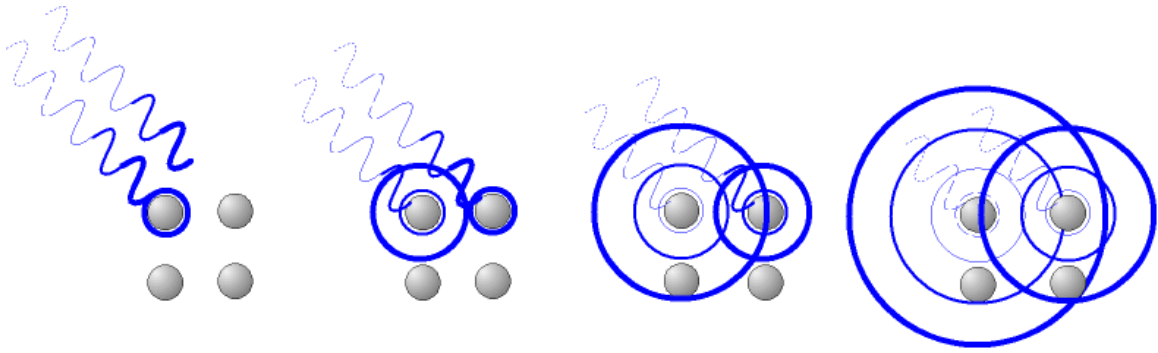
Figure 22. The creation of spherical wave fields through atomic interaction with incident waves

As the spherical waves interact they will interfere, causing places where they reinforce one another and other places where they cancel out.

a.							b.
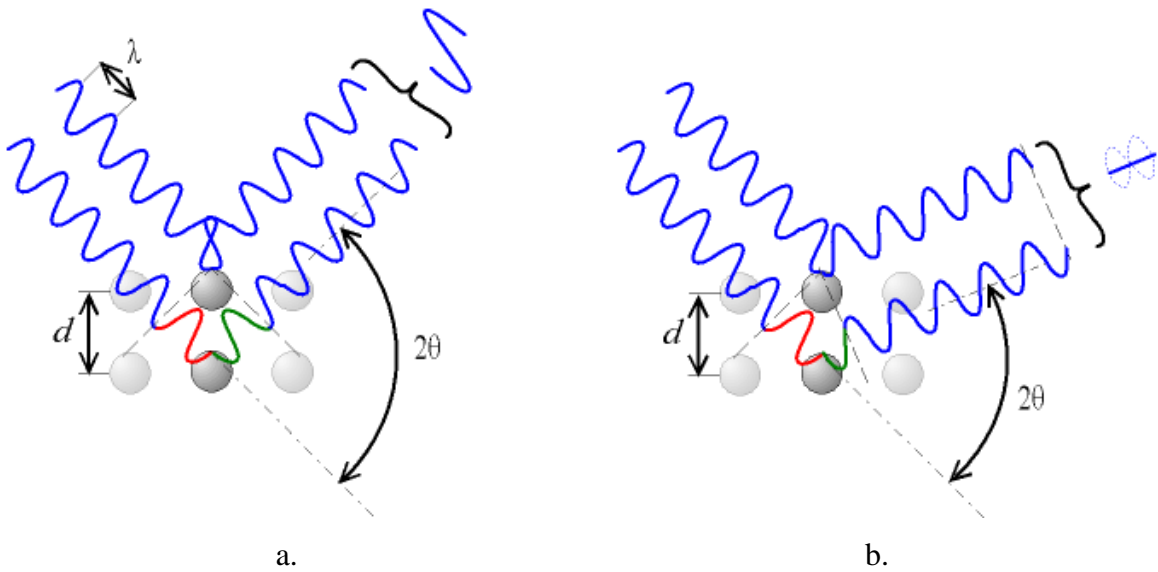
Figure 23. Bragg scattering: a.) constructive interference b.) destructive interference

Globally these waves will only reinforce each other in particular directions, and this will

be observed as scattered neutron waves traveling in well-defined directions which are

closely related to the symmetry and spacing (lattice) of the scattering sites. This

relationship is used to deduce both the symmetry and atomic distances of the lattice. This

entire process is called diffraction and is governed by Bragg's law, Eq 24, the same law

used for x-rays.

$$n\lambda = 2d\ sin\theta$$ **Eq 24**

Here *n* is an integer, λ is the wavelength, *d* the atomic spacing and θ is the angle of

reflection which is one half of the scattering angle, 2θ. For simplification, Bragg's law is

generally described in terms of the path-length difference of neutrons waves interacting

with the lattice.

4.3 SMARTS

The Spectrometer for Materials Research at Temperature and Stress (SMARTS) is a

third-generation neutron diffractometer optimized for the study of engineering materials.

Its development was funded by DOE and came online in the summer of 2001.[47] This

spectrometer is fed by a spallation neutron source at the Manuel Lujan, Jr. Neutron

Scattering Center at the Los Alamos Neutron Science Center (LANSCE), which directs

twenty 800-MeV bursts of protons per second into a tungsten target to produce spallation

neutrons.[45]

SMARTS provides an wide range of capabilities for studying polycrystalline materials

focusing on the measurement of deformation under stress and extreme temperature, and

the measurement of spatially resolved strain fields. The underlying technique is neutron

diffraction, which has been used to study engineering structural materials since the early

1980s.

With an extensive array of in situ capabilities for sample environments, it enables

measurements on small (1 mm^3) or large (1 m^3) samples. Components with dimensions

up to 1 m and up to 1,500 kg can be positioned precisely in the beam. Permanently

mounted alignment theodolites provide a simple and efficient way to position samples or equipment to within 0.01 mm. The furnace and load frame allows research on materials under extreme loads (250 KN) and at extreme temperatures (1,500°C). In situ uniaxial loading on samples up to 1 cm in diameter at stresses of 2 GPa and with lower stresses at temperatures up to 1,500°C are common.[47]

4.4 Time of Flight Method

SMARTS at LANL relies on the time of flight method to measure the energies of the neutrons in the incoming pulsed beam. Since this incoming beam contains neutrons of multiple energies the beam vector can remain fixed with respect to the sample as these multiple neutron energies translate to the beam having multiple incident neutron wavelengths. Figure 24 shows a schematic of the diffraction chamber at SMARTS.
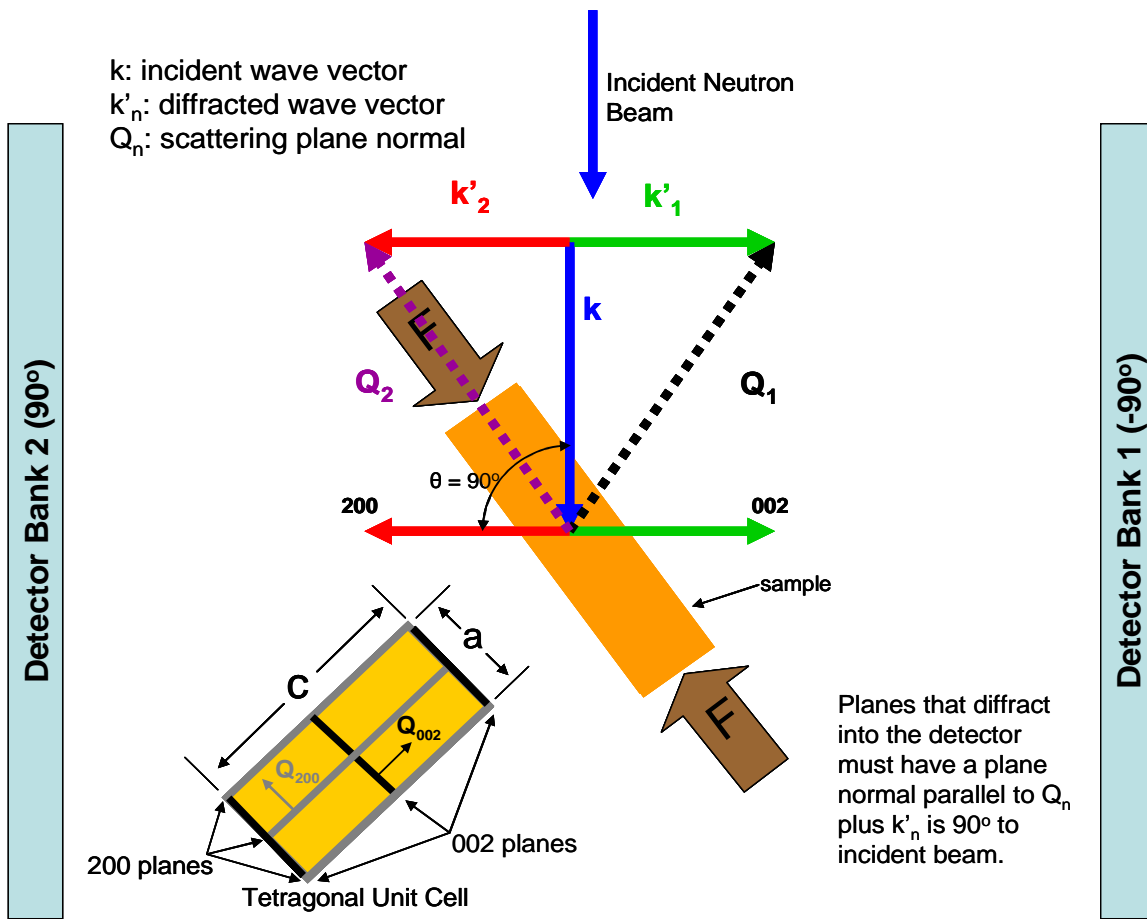
Figure 24. Schematic of the SMARTS facility at LANSCE

Here the blue vector *k* represents the incoming neutron beam, manifested as a pulse of
neutrons from the spallation source.   Again, this pulse contains neutrons having a range
of velocities which translates into neutrons of varying energies as shown by Eq 25 and Eq
26 .[45]

$$v = \frac{L}{t}$$ **Eq 25**

Here *v* is the velocity. *L* is the length or distance traveled from the source to the detector,
and *t* is the "time of flight" needed to cover that distance, *L*.

$$E = \frac{1}{2}mv^2$$ **Eq 26**

Here *E* is the neutron energy and *m* is its mass, 1.6749286 x 10^{-27} kg.[46] The neutron
energy can be used to calculate its wavelength, λ using Eq 27.

$$\lambda = \frac{h}{mv}$$ **Eq 27**

Here *h* is Planck's constant, 4.1456692 x 10^{-15} eV ·s. This range of wavelengths in the
pulsed neutron beam results in a full diffraction pattern across theta without the need to
rotate the sample with respect to the neutron beam.

5. Electrochemical Metal Deposition

Electrochemical deposition of metals and alloys involves the reduction of metal ions from aqueous, organic, and fused-salt electrolytes. Here the focus will remain on aqueous solutions only. The reduction of metal ions M^{z+} in aqueous solution is represented by Eq 28.

$$M^{z+}_{\text{in solution}} + ze^{-} \longrightarrow M_{\text{lattice}} \qquad \textbf{Eq 28}$$
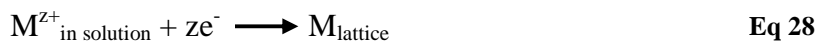
This can be accomplished via two different processes: (1) an electrodeposition process in which z electrons (e^{-}) are provided by an external power supply or (2) an electroless (autocatalytic) deposition process in which a reducing agent in the solution is the electron source and there is no external power supply involved. These two processes, electrodeposition and electroless deposition, constitute electrochemical deposition and will be addressed in the following two sections.

5.1 Electrochemistry and Electrode Potential

When a metal M is immersed in an aqueous solution containing ions of that metal, M^{z+} there will be an exchange of metal ions between the solution and the metal. Some M^{z+} ions from the crystal lattice enter the solution, and some ions from solution enter the crystal lattice. Initially one of these will occur faster than the other. Let us assume that conditions are such that more M^{z+} ions leave than enter the crystal lattice. In this case, there is an excess of electrons in the metal and it acquires a negative charge, q_M^{-} (charge on the metal per unit area). In response to the charging of the metal side of the interface, there is also a rearrangement of charges on the solution side. The negative charge on the metal attracts the positively charged M^{z+} ions from the solution and repels negatively charged ions. The result is an excess of positive M^{z+} ions in the solution in the vicinity of the metal/solution interface. At the same time, the solution side of the interface acquires opposite and equal charge, q_s^{+} (the charge per unit area on the solution side of the interface). This positive charge on the solution side slows down the rate of M^{z+} ions leaving the crystal lattice (due to repulsion) and accelerates the rate of ions entering the

crystal lattice. After a certain period of time a dynamic equilibrium between the metal M

and its ions in the solution will result according to Eq 29,

$$M^{z+} + ze \longleftrightarrow M^0 \qquad\qquad \textbf{Eq 29}$$

were z is the number of electrons involved in the reaction. In this reaction taken from left

to right, electrons are consumed through the reduction of the metal ions. From right to

left, electrons are released through the oxidation of M^0. Again, equilibrium occurs when

the rate at which both of these mechanisms occur is equal. When this is true, the charge

on the metal (q_m) is equal to the charge of the solution ($-q_s$) at the interface.

Before and while this equilibrium is being reached, there exists a potential difference

between that of the metal and the solution. In order to measure the potential difference of

this interphase, it must be connected to another one forming an electrochemical cell. The

potential difference can then be measured across the entire cell.

Electrochemical deposition takes advantage of the nonequilibrium transfer of ions to and

from the solution. In the nonequilibrium state there is a steady state of ions either being

deposited or dissolved from any electrode in contact with the electrolyte solution. During

electroplating an external power source, commonly called a rectifier, is connected

between two electrodes both of which are in contact with the electrolyte, and the applied

voltage maintains a constant state of nonequilibrium causing constant deposition at the

cathode. In electroless plating, the state of nonequilibrium is simply prolonged by

complexing agents which bind metal ions allowing for controlled deposition of the plated

species from a relatively concentrated electrolyte.

5.2 Electroless Plating

Electroless (autocatalytic) plating involves the use of a chemical reducing agent to reduce

chelated metal ions at the solution/substrate interface forming a uniform deposition upon

the surface. This process can be done for several different metals and alloys including:

Cu, Ni, Co, Pd, Pt, Au, Cr and a variety of alloys involving one or more of these

constituents plus P or B.[48] This process is deemed "electroless" due to the lack of a need for external electrodes or a power supply. There is however a transfer of electrons from the reducing agent to the metal ion according to Eq 30,

$$M^{z+} + Red \xrightarrow[\text{surface}]{\text{catalytic}} M^0 + Ox \qquad\qquad \textbf{Eq 30}$$
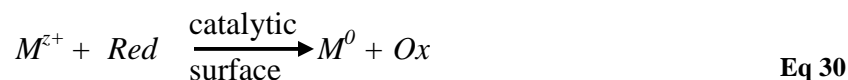
Where *Ox* is the oxidation product of the reducing agent, *Red* and *M* is the metal plated. According to mixed-potential theory, the overall reaction given by Eq 30 can be decomposed into one reduction (cathodic) reaction,

$$M^{z+} + ze \text{ (from reducing agent)} \xrightarrow[\text{surface}]{\text{catalytic}} M^0 \qquad\qquad \textbf{Eq 31}$$
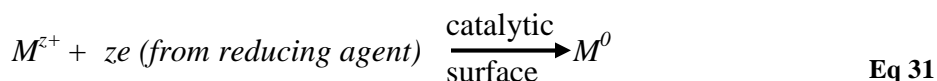
and one oxidation (anodic) reaction.

$$Red \xrightarrow[\text{surface}]{\text{catalytic}} Ox + ze \qquad\qquad \textbf{Eq 32}$$

These two partial reactions occur at one and the same electrode, the metal-solution interface. In order for electroless deposition to proceed, the equilibrium (rest) potential of the reducing agent must be more negative than that of the metal being plated.

However, Eq 30 can only occur only on a catalytic surface.[48] Once the initial layer is deposited, the metallic layer itself acts as the catalytic surface, allowing for the process to continue.   For most non-catalytic substrates, plating can be done, but only after some surface preparation rendering them catalytically active.

Surface Preparation

As previously mentioned, electroless plating must take place on a catalytic surface. Various metals exhibit catalytic properties useful in chemical plating, including the precious metals Au, Ag, and members of the platinum metal family. Electroless plating can also occur on certain less noble metals such as Co, Ni, Cu and Fe,[49]but these metals are not truly catalytic. When attempting to plate a metal onto a less noble one, an

exchange of charges occurs at the surface. This results in a layer of the more noble metal
being deposited, which acts as the catalyst on which electroless plating then occurs.[50]
All other substrates, especially nonconductors, require some surface preparation prior to
plating. This generally involves the deposition of a catalyzing metal onto its surface at
which point the material is activated. Palladium is generally the best choice for
activation of non-conductive substrates. The following sections give detailed examples
of activation methods.

Surface Roughness

Most activation methods rely on some degree of mechanical adsorption. Thus the degree
of activation can be increased with increasing surface area. This technique is generally
not needed when plating onto metals, but is common when plating nonconducting
material. A common method of increasing surface area is by increasing the surface
roughness of the substrate. This can be done by either mechanical (sanding sandblasting)
or chemical (etching) means, although chemical treatments are usually preferred.
Chemical methods not only roughen the surface through the creation of fine pits, but they
can also modify surface functionalities, which can, for instance, convert a hydrophobic
(nonpolar, water-repelling) to a hydrophilic (polar, water compatible) surface. Some
example chemical baths for use with nonconducting polymers can be found in Table 7.[51]

Table 7. Example chemical surface roughening baths

1. CrO_3 H_2SO_4	75 g/l 250 ml/l
2. $K_2Cr_2O_7$ H_2SO_4	90 g/l 600 ml/l

3. CrO_3
    H_2SO_4
    HF
	50 g/l
	100 ml/l
	100 ml/l

These solutions are used for 1 to 5 min, at 20-35°C, or as required to produce the desired
hydrophilic surface, interlocking etch areas, and/or chemical bonding sites.
Underexposure results in incomplete activation leading to skip plating. Overexposure
generally results in physical and chemical degradation of the surface, giving poor
adhesion. In both cases peeling and blistering can occur.

Plasma techniques can also be used to alter the surface characteristics of polymeric substrates, and have the advantage of not producing waste, which must be disposed of.[52] In the case of plating onto ceramic or semiconductors, these chemical roughening baths are generally not required.

Cleaning

Any substrate to be plated must first be thoroughly cleaned. As most activation methods rely on adsorption, it is important to have a clean surface so that the plated layer will be adhered to the substrate and not simply to contamination found on its surface. Residues from cleaners and deoxidizers may create inactive spots that will not initiate electroless deposition. This may result in the necessity to have a thicker deposit before continuity is achieved. This step is extremely substrate dependent, and may need to be tailored around substrate stability. An example set of cleaning steps can be found in Table 8.[5]

Table 8. Example cleaning steps

Purpose	Constituents	notes	time, min	^{o}C
Cleaning	ultrasonically cleaned in an ethyl-alcohol bath	- rinse when done	5	room
Alkaline Cleaning	- 100ml DI water - 4.0g NaOH 97%	- stir until NaOH is dissolved - bring to temperature - pour over powder and stir - DI rinse when done	15	65-70
Acid Cleaning	- 75ml DI water - 25ml HCl 36.5-38%	- stir and bring to temperature - pour over powder and stir - DI rinse when done	15	30-35

The use of each and every cleaning step may not always be necessary, but is recommended. This is dependent on the cleanliness of the substrate and its chemistry.

Sensitizing/Activation Catalysis

Sensitizing and activation (S/A) involve the application of a catalytic metal to a non-catalytic surface. As implied by the name, this involves two steps. The first step, sensitizing, consists of adsorbing a readily oxidized material onto the surface to be plated. Solutions containing tin(II) or titanium(III) salts and small amount of acid are commonly

used. The addition of acid inhibits hydrolyzation of the metal salts, which leads to the

formation of insoluble oxychlorides.[51] In the case of Sn, the amount of Sn on the surface

of the sensitized substrate is about $10\mu g/cm^3$, and surface coverage is less than 25%.

This Sn is in the form of dense clumps about 10-25nm in size, consisting of particles on

the order of 2.5nm.[53] Immersion in the sensitizing bath is normally done at 20°-30^oC for

1-3 min.[53] Agitation can improve results, especially when plating complicated shapes.

After this step, pieces must be thoroughly rinsed, as dragin of the sensitizer will destroy

the activation bath.[51] Avoid drying in air after this step, as the adsorbed Sn^{2+} can form

SnO at the surface.

It is during the activation step that the surface truly becomes catalytic. The most

effective activation solutions contain precious metal salts, such as gold, silver, or the

platinum group metals (Au, Pt, Rh, Os, Ag), along with small additions of acid.[51] Here,

the acid stabilizes the bath by both limiting the precipitation of Pd particles and

decreasing the reduction rate. Activation baths are used at 20-45°C, with immersion

times of 1-2 min.[53] When the sensitized piece comes in contact with the activation

solution, the adsorbed sensitizer is readily oxidized, thereby reducing the activating metal

and depositing it in the metallic state forming nucleation centers on the surface, according

to the example in Eq 33.

$$Pd^{2+} + Sn^{2+} \rightarrow Sn^{4+} + Pd^0 \qquad \textbf{Eq 33}$$

It is estimated that these catalytic nucleation centers are less than 1nm in diameter, and

their height is ~ 4nm. As an example, the amount of Pd on a glass substrate is generally

0.04-0.05$\mu g/cm^3$, which assuming uniform distribution corresponds to roughly 0.3 of a

monolayer of Pd.[53] The surface density of catalytic sites is substrate material dependent.

For glass this is roughly 10^{14} sites/cm^2.[53]

Thorough rinsing should also follow the activation step, as dragin of precious metal salts

will cause spontaneous seeding and breakdown of most plating baths. An example S/A

recipe can be found in Table 9.

Table 9. Example sensitizing and activation recipe

Purpose	Constituents	notes	time, min	^{o}C
Sensitizing	- 120ml DI water - 3.0g SnCl$_2$•2H$_2$O 98.2% - 5ml HCl	- stir and bring to temperature - pour over powder and stir - do not allow undissolved SnCl$_2$ to be transferred - DI rinse when done, 3x - Avoid drying	1-3	25-30
Activating	- 125ml DI water - 0.03g PdCl$_2$ 99.9+% - 0.063ml HCl (~2 drops)	- stir and bring to temperature - pour over powder and stir - do not allow undissolved PdCl$_2$ to be transferred - DI rinse when done, 3x - rinse once in ethyl-alcohol - allow to dry in air	1-2	40-45

If, as sometimes is the case, a given metal can be reduced by the sensitizing ion, then it may not be necessary to utilize an activation bath. Instead, the substrate is immersed in the electroless bath immediately after sensitizing and rinsing.   An example system, where this is the case, is electroless Cu or Ag when using a Sn(II) based sensitization bath.[48]

Colloidal Catalysis

This method is an alternative to sensitization and activation catalysis, utilizing a mixed colloidal catalyst. The colloid particles contain a core of reduced, metallic Pd, also containing a small amount of Sn metal. This core is surrounded by a stabilizing layer of Sn^{+2} and Sn^{+4} ions,[48, 52] which attract dissolved chloride when in solution. Particle diameter can range from 2.5-35nm, and is described by Figure 25.[50]
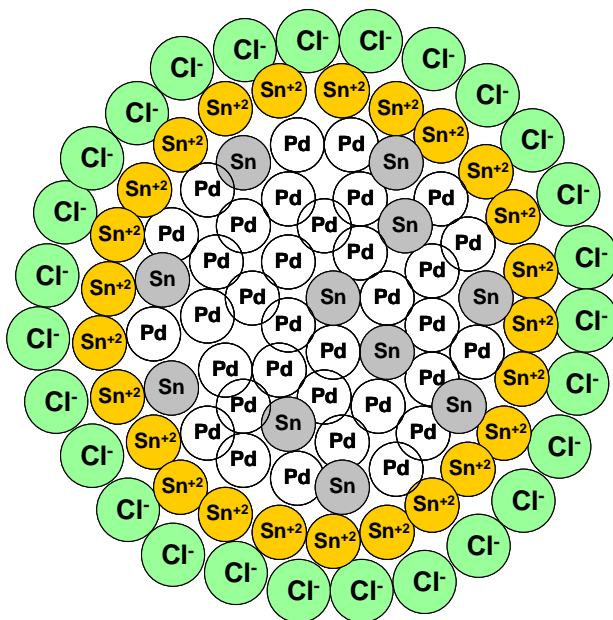
Figure 25. Colloidal activation-Pd cluster enveloped by tin ions

Table 10 contains a recipe for a Sn/Pd colloid solution found by the author to catalyze a
wide variety of plastic, ceramic and metallic substrates for electroless plating of Cu and
Au. It is very stable and can be stored for long periods without deterioration.[54]

Table 10. Recipe for a Sn/Pd colloidal catalyzing solution

Purpose	Constituents	notes	Time, min	^{o}C
Solution A - provides excess Sn ions for stability	- 1.4g $Na_2SnO_3 \cdot 3H_2O$ - 9.6g $SnCl_2 \cdot 2H_2O$ 98.2% - 40ml HCl	- stir until all solids are dissolved	15-20	15-20
Solution B - formation of colloid particles	- 0.2g $PdCl_2$ 99.9+% - 20ml HCl - 40ml DI water - 0.4g $SnCl_2 \cdot 2H_2O$ 98.2%	- combine PdCl2, HCL, and water - stir until all solids are dissolved (10-15 min) - add $SnCl_2$ and stir for 12 min, the color will change from and an initial dark green to dark olive brown	See notes	40-45
Mixing		- pour solution B into A while stirring	quickly	N/A
Activation		- cover - heat to 57°C for 3 hrs	50-65	180
Dilution		- can be diluted down to 15v% provided HCl makes up 10-20v% of the final volume		N/A

After mixing, the combination of solutions A and B is a concentrated solution containing roughly 58w% concentrated (37%) hydrochloric acid and 32w% water with the balance being Pd and Sn salts. It is immediately ready for use, but is made more aggressive by heating it to 50-65°C, for three hours.[54]

An important variable in the preparation procedure, which affects the nature of the resulting colloid, is the length of time during which the stannous chloride is allowed to react with the palladium chloride in solution B, before it is combined with the balance of stannous chloride in solution A. This reaction time has a significant effect on the final particle size, size distribution and shape in the resulting colloid.[54] Due to this, solution B must be stirred for exactly 12 min as times less than 10 minutes lead to marginal catalysis ability of the solution and times greater than 14 minutes lead to solution instability.

If the area to be plated requires high resolution as in the case of printed circuit boards, the prepared colloidal solution should be diluted 1:1 with DI water and with sufficient additional concentrated HCl to comprise 20-30v% of the final volume. For ordinary surface plating, the catalyzing solution should comprise 15v% prepared colloid, 10-20v% concentrated HCl, and the balance DI water.

Regardless of concentration, the substrate is immersed in or contacted with the activation solution for a minimum of 1 min at room temperature. Upon contact with the substrate, the colloidal particles adhere to the surface, forming catalytic nucleation sites.[55] Following contact with the catalyzing solution, the substrate shall be thoroughly rinsed in DI water before immersion into a chemical plating bath.   If the substrate is not to be immediately plated, it can be rinsed in alcohol, dried, and plated later.

After the catalytic solution is rinsed away, the ionic tin no longer plays a role, and can in fact bury the Pd core and detract from its catalytic activity.[52]   In cases where the metal to be plated cannot be reduced by the Sn (II) ion, an acceleration step is required to remove the excess tin ions and expose the catalytic Pd surface. Some accelerating solutions include 1 M HCl, 1 M NaOH, 1 M NH4BF4, 1 M NH4HF2, 0.13 M EDTA at

pH 11.7, and 0.13 M EDTA at pH 4.5. Substrates should be immersed for a minimum of 1 minute followed by thorough rinsing in DI water.[52]

Colloidal vs. Sensitizing/Activation Catalysis

In practical applications the mixed colloidal technology seems to be preferred. The reasons for this are as follows:

- It exhibits more reproducibility than the separate Sn-Pd (S/A) technology
- After activation the Pd layer is clearly visible. Not so for the S/A process.
- Mixed colloidal solutions are stable and do not exhibit ageing effects as do Sn solutions.
- Mixed colloidal solutions are rather resistant to impurities.
- Surface preparation is far less critical than in the case of Sn based solutions.

For the separate S/A process, other than being clean, surfaces must also be hydrophilic in order to be efficiently wetted by the sensitizing solution. However, despite the above-mentioned advantages of the mixed colloidal technology over the S/A process, the initial nucleation site density achieved by the latter method is up to an order of magnitude greater than that obtained using the colloidal method. This means that a continuous film can be obtained at a smaller plating thickness. In practical terms this translates into the following advantages:

- Less metal is needed to render the surface conductive
- Better adhesion due to a higher density of fastening sites.
- Potential in the development of products where very thin coatings are required.

Electroless Plating of Copper

Typical electroless copper solutions comprise deionized water, a source of copper ions, a complexing agent for copper ions, a pH regulator, a reducing agent, and a bath stabilizing agent. Plating is usually performed between 30-80°C.[56] Most commercial baths utilize

formaldehyde (HCHO) under basic conditions as the reducing agent, thus only baths of this type will be addressed here. In this case, electroless Cu plating is a result of the reaction given in Eq 34.

$$Cu^{2+} + 2HCHO + 4OH^{-} \xrightarrow[\text{surface}]{\text{catalytic}} Cu^{0} + 2HCOO^{-} + 2H_2O + H_2$$

Eq 34
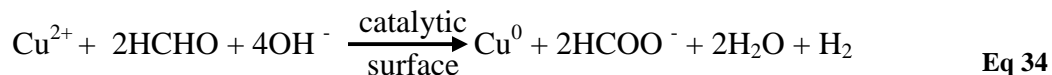
Ions of Cu^{2+} are generally added as Cu salts, such as $CuSO_4$, but halides, nitrates, acetates and other organic and inorganic acid salts of Cu may be used.[57] Since the solubility of Cu^{2+} decreases with increasing pH,[58] complexing (chelating) agents are also commonly added to the plating bath to avoid the precipitation of copper(II)hydroxide $(Cu(OH)_2)$.[48] These ligands form co-ordinate bonds with the Cu^{2+} ions allowing them to stay in solution. Complexing agents are usually organic acids or their salts, such as EDTA, EDTP, and tartaric acid.[48, 58]

Basic conditions are generally realized through the addition of NaOH, elevating the pH to 12-13, where the plating rate reaches a maximum.[58] Formic acid $(HCOO^{-})$ is the oxidation product of the reducing agent, formaldehyde.[58] Evolved H_2 gas and excess H_2O are formed as byproducts of the reaction, with Cu^{0} being left behind as a plated film on the catalytic surface.

Electroless Plating of Nickel

Typical electroless nickel solutions, like copper, comprise deionized water, a source of nickel ions, a complexing agent for the nickel ions, and a reducing agent. Plating is usually performed between 50-100°C an at pH values from about 4 to 11.[48] Four reducing agents are generally utilized in nickel electroless plating: sodium hypophosphite $(NaH_2PO_2 \cdot H_2O)$, sodium borohydride $(NaBH_4)$, Dimethylamine borane $((CH_3)_2NHBH_3)$, and hydrazine $(N_2H_4 \cdot H_2O)$.[59] These are all structurally similar in that each contains two or more reactive hydrogen atoms, and nickel reduction is said to result from the catalytic dehydrogenation of the reducing agent. Only baths reduced using hypophosphite will be

54

addressed here. In this case, electroless Ni plating is a result of the reaction given in Eq 35.

$$Ni^{2+} + 2H_2PO_2^- + 2H_2O \xrightarrow[\text{surface}]{\text{catalytic}} Ni^0 + 2H_2PO_3^- + 2H^+ + H_2$$

Eq 35
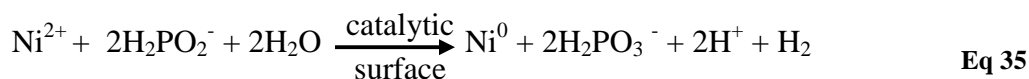
Ions of Ni^{2+} are generally added as nickel sulfate ($NiSO_4$), but chlorides and acetates may be used.[59] To increase the stability and controllability of the plating bath, complexing (chelating) agents are commonly added to buffer the pH, prevent precipitation of nickel salts, and reduce the concentration of free nickel ions.[59] Complexing agents are usually organic acids or their salts, but for alkaline plating baths, as in this work, the pyrophosphate and ammonium will be utilized.

Electroless Plated Metal Film Properties

The film may initially have bubbles especially if the substrate is smooth. These are most likely filled with H_2 and will dissipate within 2 hrs. The occurrence of this tends to increase with film thickness and is a sign of poor adhesion.

During electroless deposition hydrogen can be co-deposited in atomic (H) as well as molecular (H_2) form, however most tends to be molecular. At room temperature, or through low temperature (100-260°C) annealing, the molecular hydrogen diffuses out of the deposit, interstitially, via a dissociative reaction leading to increased ductility.[58, 60] Some of this increased ductility is also due to structural changes involving recrystallization and grain growth in the electroless deposit. Low temperature recrystallization and grain growth are commonly observed in copper films prepared by other growth techniques such as vapor deposition, sputtering and electrodeposition.[58] Poor ductility can also be caused by a high impurity content.[58]

Plating temperature can also greatly affect the film properties. Plating is typically done between 25 and 70°C. In general a fine-grained structure is produced at low temperatures, while as temperature is increased the grain structure becomes coarser and

hydrogen adsorption is decreased, leading to improved ductility and increased electrical conductivity.[58]

5.3 Electrodeposition

Electrodeposition, the process used in electroplating and electroforming, is analogous to a galvanic or electrochemical cell acting in reverse. The part to be plated is the cathode of the circuit, while the anode generally provides ions of the metal to be plated. Both of these components are immersed into a solution containing one or more metal salts as well as other ions that permit the flow of electricity. A rectifier supplies a direct current to the cathode causing the metal ions in solution to lose their charge and plate out on the cathode. In most cases the electrical current flows through the circuit, the anode slowly dissolves and replenishes the ions in the bath, as seen in Figure 24. Some electroplating processes use a noble, nonconsumable anode. In these situations, ions of the metal to be plated must be periodically replenished in the bath as the plate forms out of the solution.
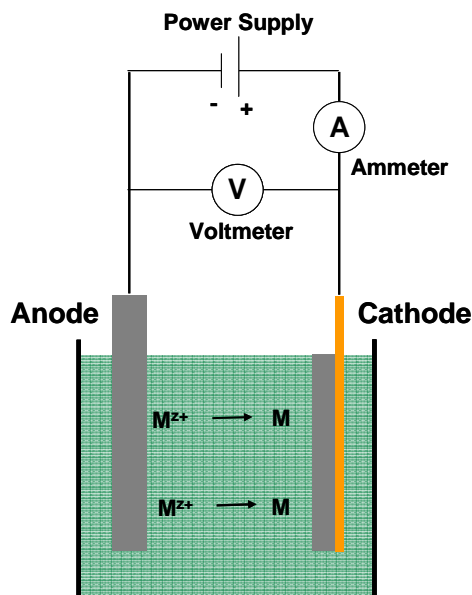
Figure 26. Typical electrodeposition cell

Electrodeposition in the form of electroplating involves the coating of an electrically conductive object with a layer of metal using electrical current. Usually, the process is used to deposit an adherent surface layer of a metal having some desired property (e.g., abrasion and wear resistance, corrosion protection, lubricity, etc.) onto a substrate lacking

that property. In the case of heavy plating, it is also used to build up thickness on undersized or worn parts. As electroforming, electrodeposition can be utilized as a means to create an entire part onto, or incorporating, a master.

Electroforming

Electroforming is a process that employs technology similar to that used for conventional electroplating, but which is used to manufacture metallic articles, rather than as a means of producing surface coatings.   While electroforming and electroplating differ in their product, they are superficially identical and fundamentally similar in their technology and execution. The work-piece, or master, is the cathode. This is suspended in a tank or vat of electrolyte. Metal anodes act as a source of electrons and in most cases are soluble and replenish the metal content of the electrolyte. Due to its metal ion content, the electrolyte is conductive and closes the electrical circuit which is fed by a source of low voltage direct current.

In many cases the master is a simple negative of the desired part. Once the desired thickness has been deposited, the electroform is separated from the master resulting in an exact positive, accurate down to the 10's of nanometers. This near exact reproduction led to the use of electroforming as the primary method to manufacture masters for vinyl records and even early phonographic cylinders. The master can also become incorporated into the electroform as is the case in this work.

Electroforming of Composites

Electroforming of composites, also known as occlusion or composite plating, is an alternate method to fabricate metal matrix composites which does not require the high temperatures and pressures involved in more traditional methods, such as internal oxidation, powder metallurgy, high pressure bonding, and infiltration.[61] The resultant composite material is termed an electrocomposite. Electrocomposites have seen most of their use in the abrasives industry where occlusion plating is used to incorporate carbides or diamond chips into metal matrices to fabricate abrasive bits and cutting blades.[62]

A variety of techniques can be used for the codeposition of particles. Primarily particles are kept in suspension by either mechanical (rotational stirrer) or chemical means (surfactants). The optimum condition for preparing particle suspensions and codepositing a designated volume fraction of uniformly dispersed inert particles has not been firmly established and tends to vary by plating bath and cathode geometry. In the literature however, particle diameters have ranged from 0.02-100µm, and quantities dispersed in solution have varied from 50-200g/L.[61] In general it is difficult to achieve a high volume fraction with this method, especially for large particle sizes. Here, incorporation relies on weak electrophoretic forces to hold particles before ionic species, adsorbed onto the particle, are reduced attaching it to the cathode at its point of contact. From there sufficient metal has to be plated around the particle sufficient to hold it in place before electrolyte convection can knock it away.[61] The high particulate loading levels required in the electrolyte can often cause contamination in the bath.

5.4 Electrodeposition of Ni

Nickel electrodeposition is primarily performed using acidic aqueous solutions of one or a combination of three Ni salts, nickel sulfate ($NiSO_4$), nickel chloride ($NiCl_2$), and nickel sulfamate ($Ni(SO_3NH_2)_2$). Boric acid (H_3BO_3) is generally used as a pH buffer. A surfactant is used to avoid pitting, and when necessary organic additives to tailor the internal stress or surface finish of the deposit.

Nickel electrodeposition is a commercially important and versatile surface finishing process, and its applications fall into three main categories: decorative, functional, and electroforming. Decorative applications generally involve the deposition of thin Ni layers to offer the plated part the appearance or corrosion resistance of Ni. Most modern corrosion resistant Ni coatings actually consist of multiple layers of Ni with a thin topcoat of Cr. This combination is often used to protect steel, zinc, copper, aluminum, and many other materials from corrosion for extended periods of time.[26]

There are many functional applications where decoration is not the issue. Here, Ni and its alloys are deposited on surfaces to not only increase corrosion resistance, but also to

improve wear resistance or to modify the magnetic or other properties of the material being plated. Of particular interest is the dependence of the properties of electrodeposited nickel on its plating conditions.

5.5 Nickel Electroforming

Today nickel is utilized in the largest number of electroforming applications because it is strong, tough, resistant to corrosion, erosion, and wear. Further, its mechanical properties can be varied and controlled by: changing solution composition and operating conditions, by alloying, and by incorporating particles and fibers within the electrodeposited nickel matrix.[26] Electroforming is electroplating applied to the production of metallic parts without the need for high temperature processing. Here, metal is deliberately electrodeposited non-adherently, so that it can be separated from a mandrel or mold which is usually a negative or reverse replica of the electroformed part.

Nickel electroforming processes can reproduce fine surfaces with resolution into the nanometer range due to the excellent microthrowing power of nickel-plating solutions. This accuracy is commonly used in the production of stampers for pressing compact audio discs and vinyl records. The combination of electroforming and modern photolithographic techniques makes it possible to produce parts with extreme precision and fineness of detail on a microscopic scale, while closely controlling the mechanical and physical properties of the metal.

Nickel Sulfamate Chemistry

All of the previously mentioned nickel salts can be utilized in Ni electroforming, however nickel sulfamate based solutions are popular for electroforming because of the low internal stress of the deposits, the high rates of deposition possible, and the improved throwing power. Nickel sulfamate is similar to nickel sulfate except that one of the hydroxyl groups is replaced by and amido group. Because of the high solubility of nickel sulfamate, higher nickel metal concentration is possible than in other nickel electrolytes, permitting higher plating rates. A small amount of nickel chloride is usually added to

nickel sulfamate solution to minimize anode passivity, however this is no longer an issue

if sulfur-containing nickel anode materials such as S-rounds in place of pure electrolytic

nickel. Prolonged use of sulfamate solution at temperatures above 70^oC and/or at a pH of

less than 3.0 can hydrolyze the nickel sulfamate to the less soluble form of nickel

ammonium sulfate. This is undesirable as the ammonium ad sulfate ions increase the

internal tensile stress and hardness of the nickel deposits, and there is no "simple" way to

remove ammonium ions from sulfamate solutions.

Throwing Power and Leveling

The throwing power of a plating bath is the degree at which the bath is able to deposit

metal evenly on to the mandrel or substrate being plated. The amount of metal deposited

onto a substrate is dictated by the density of electric field lines that intersect the surface

of the substrate. Sharp features and corners on the mandrel or substrate tend to

concentrate the field lines leading to increased metal deposition on these features. This

also holds true for features extending from the substrate, which place them closer to the

anode. This decreased distance leads to decreased electrical resistance between the

feature and the anode, but it also puts the protrusion further into the Ni solution where Ni

ions are more plentiful, leading to increased metal deposition at that site. In

electroforming this second mechanism is especially important as defects tend to magnify

with time during electrodeposition. Any small protrusion will be preferentially plated

upon eventually forming a nodule and in extreme cases a multi-armed dendrite as its

increased height further drives its growth.

These effects are especially prevalent in electroforming due to the long plating times and

high current densities involved. To combat this organic leveling agents can be employed,

such as 2-butyne 1,4-diol, however these generally act as microlevelers acting mostly

inducing a smooth polished look on the deposit. Care must also be taken when using

these compounds as their breakdown products lead to increased internal stress in the

deposit, but this can be remedied by carbon filtration. A more common method to

minimize roughness and protrusions during electroforming is the use of periodic reverse

plating. Here the polarity of the applied current is periodically reversed, as the name

implies, but also increased to as much as twice that of the forward current. Here the same factors working to create the nodules in the forward direction are used to preferentially erode away the nodules as they act as current concentration points. This is driven further by the fact that the current in the reverse direction is greater than the forward direction. This technique is especially useful when electroforming composites as the co-deposited particles act as nodule initiators significantly increasing surface roughness.

Quality Control

Controlling the composition of the plating bath is one of the most important factors contributing to the quality of electrodeposited nickel. At the outset, the bath must be prepared to the specified composition, adjusted to the proper pH, and purified before use. Thereafter the composition and pH of the solution must be controlled within specified limits, and contamination by metallic, organic, and gaseous substances must be prevented.

The pH of the nickel plating solution will rise during normal operation of the bath requiring regular additions of acid to maintain the pH within prescribed limits. In Ni sulfamate baths, sulfamic acid is added to control pH. The operation temperature also has a significant effect on the properties of the deposit. In general, most sulfamate baths are operated within 40°-70°C. Since current density determines the rate of deposition, this is generally maximized, and increases in temperature allow for increases in current density without increasing the internal stress in the deposit.

Impurities can greatly influence the behavior of the plating bath and the properties of the deposit. Organic impurities can be removed by carbon filtration. Metallic impurities are removed by dummy plating at very low current densities. Each impurity metal is preferentially plated out at a different current density, thus corrugated cathodes are commonly used to induce widely varying current densities across its surface. Dust and other particulate impurities are generally minimized through constant filtration of the bath, however for obvious reasons, this is impractical when depositing particulate reinforced composites. Some impurities cannot be removed from the plating bath. When

a sulfamate bath is contaminated with ions such as ammonia, there is no practical

separation method and the entire bath must be replaced.

Chapter Three- Experimental Procedure

Several different techniques were utilized in the fabrication and evaluation of the ferroelectric reinforced metal matrix composites (FR-MMCs) studied in this work. This chapter will attempt to describe and discuss in depth each of these techniques in a manner which would allow the reader to recreate them in a laboratory setting.

1. Materials Selection

In this work, two model systems were chosen, bearing bronze (Cu-10w%Sn)-BaTiO$_3$ and Ni-BaTiO$_3$. In both, the high damping properties of BaTiO$_3$ will be lent to a structural matrix.

1.1 Barium Titanate Reinforcement

Here, BaTiO$_3$ was selected based on having a distinct ferroelectric-to-paraelectric phase transition at its Curie temperature (T_C). Upon heating through T_C, the ferroelastic domain structure abruptly disappears, acting as a switch turning off the ferroelastic damping mechanism. This abrupt change in behavior allows for the quantification of damping effects due to domain motion versus other mechanisms in the composite system. Barium titanate (BaTiO$_3$) is also relatively thermo-dynamically stable compared to other

ferroelectric materials. Many of the current Pb-based ferroelectric ceramics (PZT, PLZT, PMN, etc.) are unstable in contact with most structural metals, such as Fe, Ni, Al, and Cu-Sn bronze, at temperatures above 300°C, as manifested by excessive reactions between the metal matrix and the reinforcement. $BaTiO_3$ is also unstable in contact with Fe, Ni, and Al at high temperature, however remains stable while co-processed with Cu-based alloys.[5]   Selected properties of ceramic $BaTiO_3$ are shown in Table 4.[22-24]

1.2 Bearing Bronze (Cu-10w%Sn) Matrix

Copper was initially selected as the matrix material due to its thermo-dynamic compatibility with $BaTiO_3$. Elemental Cu can be sintered at $\sim 900\text{-}1050^{\circ}$C.[27, 63] This is much lower than for other structural metals such as Ni, Ti, Fe and Mo. Cu is also much less reactive than structural metals having a lower melting point such as Al and Mg. To further reduce the sintering temperature an alloy of Cu- 10 w% Sn (bearing bronze) was finally selected for the matrix metal. This alloy can be liquid phase sintered at 820°C and is resistant to oxidation leading to greater ease in lab handling.

Selected properties of annealed Cu- 10w% Sn bronze are shown in Table 5.[25]

1.3 Electroformed Sulfamate Nickel Matrix

Electroforming was selected as a near room temperature fabrication technique, needed to avoid the excessive reactions between $BaTiO_3$ at the elevated processing temperatures associated with most structural metals. Nickel was chosen as a matrix metal as it is the most commonly electroformed metal whose behavior is well understood. Nickel sulfamate solutions are popular for electroforming because of their ability to produce deposits having low internal stress and utilize high rates of deposition, while generally exhibiting increased throwing power over Watts nickel solutions. Also, nickel represents a major structural material especially in advanced structural applications.

Sulfamate Ni solutions generally contain 300-450 g/L of nickel sulfamate ($Ni(SO_3NH_2)_2$) as the primary source of Ni ions, while this can exceed 650g/L for the most concentrated solutions. Nickel chloride ($NiCl_2$) is also commonly added at 0-30g/L which besides providing additional Ni ions can increase bath conductivity and limit anode passivity during plating. The pH is maintained at 3.5-5.0 with the use of boric acid (H_3BO_3) as a buffer, and anionic surfactants are added to prevent reduced hydrogen from adhering to the cathode and creating pits in the deposit. Bath temperatures can range from 25°-70^oC, with increasing temperature and decreasing current density leading to decreased internal stress in the deposit. Selected properties of electroformed sulfamate Ni are shown in Table 6.[26, 27]

2. Barium Titanate Reinforcement Fabrication

As previously mentioned, the presence of large grains and domains tends to increase twinning in ferroelastic materials. Current commercial methods used to produce $BaTiO_3$ powders however, generally result in a fine grain structure. These fine grained powders cannot be simply heat-treated as sintering/necking of the powder will result at the temperatures required for grain growth. To fabricate a powder of ~35µm, large grained, reinforcement particles, monolithic large grained material must be ground and sieved.

$BaTiO_3$ powder with a particle size (diameter) ranging from 25 - 45µm (-325 +500 mesh) was prepared by the crushing and sieving of as-delivered bulk 3 - 12 mm pieces of 99.99% purity (Sigma-Aldrich, St. Louis, MO). The bulk pieces were initially crushed to a ~1mm size, 3 ml at a time using a mortar and pestle. The $BaTiO_3$ was then poured in 3 ml increments over a stack of successively finer sieves including -120, -200, -325, and -500 mesh sizes. The sieves were shaken and rotated and fines were collected at the bottom. To prevent overfilling and clogging of the mesh, the stack was periodically emptied and cleaned, and the powders caught by each mesh were extracted. Once all of the initial $BaTiO_3$ had been passed through the top sieve in the stack, that sieve was removed, and material that had not passed through the second sieve was re-crushed. The re-crushed powder was then passed through the stack as before and the process was repeated until only the -500 mesh sieve remained. At this point, all of the powder that

had not passed through as fines was collected. It was then mixed 3 ml at a time with ethyl-alcohol and again passed wet over the -500 mesh sieve. The alcohol served to break up agglomerations of fines that would otherwise not pass, allowing for the further elimination of fines. This wet sieving was repeated three times and the powder was oven-dried at 110°C. The Horiba LA-700 particle size analyzer was used to confirm the 30 - 44μm (-325 +500mesh) powder particle size. Here, approximately 1 gram of barium titanate powder was dispersed in deionized water and suspended by the flow of water through a loop, while laser scattering was used to analyze the particle size distribution of barium titanate particles yielding a median diameter of 35.475 μm.

3. Sintered Bronze-BaTiO$_3$ FR-MMCs

3.1 Bronze Matrix Preparation

To produce the bearing bronze powder mixture, -325 mesh Cu powder of 99.9% purity (Atlantic Equipment Engineers, Bergenfield, NJ) was first reduced in H$_2$ for 30min at 250°C. The Cu powder was then blended with -325 mesh Sn of 99.9% purity (Atlantic Equipment Engineers, Bergenfield, NJ) powder in a jar mill for 2 hours under argon. After blending, the powder mixture was maintained in a glove box under argon atmosphere.

3.2 Electroless Copper Plating

In order to improve the quality of the matrix-reinforcement (M/R) interface, the reinforcement particles were electrolessly plated with Cu. Copper was chosen due to its compatibility with the bronze matrix. The presence of Sn in the bronze alloy serves to strengthen the M/R interface through interdiffusion and solid solution formation with the electrolessly plated Cu surrounding the reinforcement. Not only does a Cu layer strengthen the M/R bond, but it also decreases the amount of porosity which had formerly agglomerated at the interface due to the lack of wettability of the reinforcement powder by the matrix material.[9]

The BaTiO$_3$ reinforcement powder was electrolessly plated by a process outlined in Table 11. Here, all of the solutions were prepared in 600ml Pyrex beakers and the bath temperature was maintained using a hotplate equipped with a temperature probe and controller. Between each step, the material was rinsed using deionized (DI) water. In doing this, most of the solution was first siphoned away and replaced with DI water, completely submersing the material being plated. The mixture is then stirred for 5 seconds and the liquid is again siphoned away. DI water is again added, and this process is repeated three times.

This recipe remained stable in contact with, and was sufficient to plate, 4,000cm^2 of surface area at a rate of ~ 4µm/hr.

Table 11. Electroless copper plating recipe

Purpose	Constituents	notes	time, min	°C
Cleaning	ultrasonically cleaned in an ethyl-alcohol bath	- rinse when done	5	room
Alkaline Cleaning	- 100ml DI water - 4.0g NaOH 97%	- stir until NaOH is dissolved - bring to temperature - pour over powder and stir - DI rinse when done	15	65-70
Acid Cleaning	- 75ml DI water - 25ml HCl 36.5-38%	- stir and bring to temperature - pour over powder and stir - DI rinse when done	15	30-35
Sensitizing	- 120ml DI water - 3.0g $SnCl_2 \cdot 2H_2O$ 98.2% - 5ml HCl	- stir and bring to temperature - pour over powder and stir - do not allow undissolved $SnCl_2$ to be transferred - DI rinse when done	10	25-30
Activating	- 125ml DI water - 0.03g $PdCl_2$ 99.9+% - 0.063ml HCl (2 drops)	- stir and bring to temperature - pour over powder and stir - do not allow undissolved $PdCl_2$ to be transferred - DI rinse when done - rinse once in ethyl-alcohol - allow to dry in air	25	40-45
Plating 1 - adjusts pH	- 30ml DI water - 4.0g NaOH	- stir until NaOH is dissolved	until dissolved	room
Plating 2 - provides Cu ions	- 80ml DI water - 1.25g $CuSO_4 \cdot 5H_2O$ 98+% - 7.5g EDTA 99.0-101.0%	- stir vigorously - slowly add plating solution 1 until solution 2 becomes deep blue, pH ~9.0 - bring to temp - slowly add additional plating solution 1 until solution 2 becomes light blue, pH ~12.5	to temp	40
Plating 3 - reduces Cu ions	- 2.5ml HCOH 37w% in H_2O (10-15% methanol) - 0.002ml Pyridine 99+%	- put Pyridine on the lip of the beaker containing HCOH - slowly pour HCOH into solution 2, running the last of it over the Pyridine - add material to be plated - bring to temperature	~4μm/hr	50

The surface area of the $BaTiO_3$ powder was first estimated to be 2,734cm^2/g based on the median diameter of 35µm and the assumption that the particles were spherical. A Quantachrome Instruments gas sorption system was then used to run a Brunauer,

Emmett, and Teller (BET) surface analysis. This involves the flowing of an adsorbing gas over a sample cooled with liquid nitrogen, and using the amount of gas adsorbed to determine surface area. This test yielded a value of 2,960cm^2/g, which was in close agreement with the earlier estimate of 2,734cm^2/g. This enables the surface area of crushed BaTiO$_3$ powder prepared in the manner outlined in this work to be reasonably estimated based on the median particle diameter and a spherical shape assumption.

3.3 Bronze-BaTiO$_3$ Composite Fabrication

FR-MMCs were created using the bearing bronze matrix (Cu-10 w% Sn) reinforced with 0, 15, 30, and 45 volume percent particulate BaTiO$_3$. The appropriate amounts of each powder (Cu, Sn, BaTiO$_3$) were combined and blended in a jar mill for 2 hours. The Cu-Sn-BaTiO$_3$ powder mixtures were then uniaxially pressed at 280 MPa into disc shaped powder compacts roughly 3 mm in height with a 29 mm in diameter and liquid phase sintered in argon at 820°C for six minutes. The heating rate was 10°C/min, and the cooling rate was 10°C/min between 820-300°C. Below 300°C, samples were furnace cooled, which has been found to result in greater tetragonality in the BaTiO$_3$ reinforcement and to minimize possible residual stresses in the matrix. From the composite discs, three-point bend bars were cut using a diamond blade abrasive saw.

4. Electroformed Nickel-BaTiO$_3$ FR-MMCs

As was previously mentioned, most combinations of a ferroelectric ceramic reinforcement within a metal are unstable and tend to react at the high temperatures involved with traditional metals processing. In an effort to study the ferroelastic damping behavior of FR-MMCs other than the bronze-BaTiO$_3$ system, near room temperature composite fabrication methods are needed. Here electroforming was selected.

4.1 Electroless Nickel Plating

To improve the quality of the M/R interface and increase the efficiency of particle incorporation during electroforming, the BaTiO$_3$ reinforcement particles were Ni electrolessly plated.

This process is outlined in Table 12. As with the electroless Cu plating, all of the

solutions were prepared in 600ml Pyrex beakers and the bath temperature was maintained

using a hotplate equipped with a temperature probe and controller. Between each step,

the material was rinsed three times using deionized (DI) water. the solution was first

siphoned away and replaced with DI water, completely submersing the material being

plated. The mixture is then stirred for 5 seconds and the liquid is again siphoned away.

Table 12. Electroless nickel plating recipe

Purpose	Constituents	notes	time, min	^oC
Cleaning	ultrasonically cleaned in an ethyl-alcohol bath	- rinse when done	5	room
Alkaline Cleaning	- 100ml DI water - 4.0g NaOH 97%	- stir until NaOH is dissolved - bring to temperature - pour over powder and stir - DI rinse when done	15	65-70
Acid Cleaning	- 75ml DI water - 25ml HCl 36.5-38%	- stir and bring to temperature - pour over powder and stir - DI rinse when done	15	30-35
Sensitizing	- 120ml DI water - 3.0g $SnCl_2 \cdot 2H_2O$ 98.2% - 5ml HCl	- stir and bring to temperature - pour over powder and stir - do not allow undissolved $SnCl_2$ to be transferred - DI rinse when done	10	25-30
Activating	- 125ml DI water - 0.03g $PdCl_2$ 99.9+% - 0.063ml HCl (2 drops)	- stir and bring to temperature - pour over powder and stir - do not allow undissolved $PdCl_2$ to be transferred - DI rinse when done - rinse once in ethyl-alcohol - allow to dry in air	25	40-45
Solution 1 - provides Ni ions	- 90ml DI water - 2.5g $NiSO_4$ - 4.0g $Na_4P_2O_7$ - 2.3 ml NH_4OH	- add $NiSO_4$ and $Na_4P_2O_7$ to DI water - stir until dissolved - add NH_4OH, color will change from lime to emerald green - bring to temp	until dissolved	50
Solution 2 - reducer	- 10ml DI water - 2.5g NaH_2PO_2	- add NaH_2PO_2 to DI water - stir until dissolved - add to solution 1 - add material to be plated	until dissolved	room

This recipe remained stable in contact with, and was sufficient to plate, $4,000cm^2$ of surface area at a rate of $\sim 4\mu m/hr$ (decreased plating surface area will result in faster plating rates). As for the Cu-based system, the surface area of the $BaTiO_3$ powder was measured using a Quantachrome Instruments gas sorption system to run a Brunauer, Emmett, and Teller (BET) surface analysis. It was found that the surface area can again be reasonably estimated based on the median particle diameter and a spherical shape assumption.

4.2 Electroforming of FR-MMCs

In this work electroformed Ni from a nickel sulfamate based electrolyte is used as the matrix material. Here Ni plated $BaTiO_3$ reinforcement particles are suspended in the electrolyte solution resulting in their codeposition along with the electroformed Ni metal. This Ni coating of the $BaTiO_3$ serves as a physical barrier between the reinforcement and the Ni electrolyte minimizing contamination of the electrolyte. The conductive nature of this Ni coating also aids in the incorporation of the particles. Instead of the particles having to be "caught" by the electroformed Ni layer, as is the case with bare nonconducting ceramic particles, the Ni plated particles actually become electrically connected and part of the cathode upon contact. This causes Ni to be electroformed on and around each particle leading to incorporation after a single contact event with the cathode, decreasing the necessary amount of particles which must be added to the electrolyte from roughly 200 to 0.02g/L and increases the amount of reinforcement that may be incorporated in the composite.

The interface formed between the electroformed Ni matrix and the Ni plated $BaTiO_3$ should also prove very strong. Here the Ni coating is chemically and mechanically bonded to the $BaTiO_3$ and seamlessly becomes a part of the Ni matrix through the process of electroforming. Overall this process provides a near-room temperature fabrication technique in which to produce FR-MMCs which could lead to the incorporation of other ferroelectric materials which like $BaTiO_3$ would not normally be compatible with most matrix metals at the temperatures required for their processing.

A schematic of the electroforming system used in this work is shown in Figure 27.
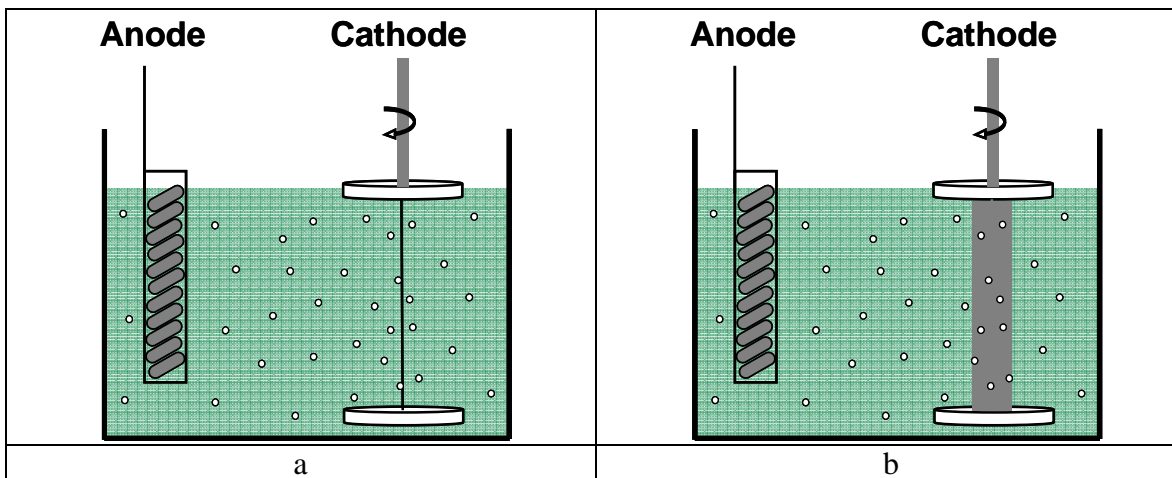

Figure 27. Composite electroforming bath used in this work: a.) initial set up b.) composite growth with time

Here the anode takes the form of a Ti mesh basket filled with electrolytic Ni pellets and covered with a woven polypropylene bag (not pictured). The cathode is in the form of a 250µm diameter, commercially pure Ni wire that is stretched between two acrylic disks by four threaded nylon rods (not pictured). Here, nickel along with incorporated $BaTiO_3$ particles, is deposited onto this wire which after fabrication remains part of the electroformed composite. To ensure both a uniform Ni deposit and a uniform volume fraction of $BaTiO_3$ reinforcement, the entire cathode apparatus is rotated and the entire bath is aggresively mechanically agitated. This creates a uniform average current density on the cathode surface and should significantly reduce Stokes settling of the particles in the bath.

Using this method the length of the resulting composite cylinder is dictated by the spacing between the acrylic discs and the diameter a result of the volume of Ni deposited. The amount of nickel that is deposited at the cathode is determined by the product of current (in amperes) and the time (in hours). The plating bath contains divalent Ni ions (Ni^{+2}), which must react with 2 electrons to form a metallic Ni atom, as shown in Eq 36.

$$Ni^{2+} + 2e^- \longrightarrow Ni^0 \qquad\qquad \textbf{Eq 36}$$

Under ideal conditions, 26.8 A flowing for 1 hr will deposit 29.4g of Ni, leading to the common standard for nickel plating of 1.095g/A-hr. However, under real conditions efficiency is estimated at 96.5 percent, as a portion of the current is utilized to reduce hydrogen ions, which leads to an increase in pH over time.

Not just any amount of current may be applied to the cathode however, as current density can significantly affects the properties of the electrodeposit as discussed in Chapter 1. Generally to achieve low internal stress in Ni sulfamate deposits, the current density is limited to between 0.05-0.3 A/cm^2. This can be raised above 0.3 A/cm^2 for highly concentrated baths or decreased below 0.05 A/cm^2 in cases where throwing power is critical.[64] For typical parallel plate type electrodeposition, this is straightforward as the area of the cathode remains consistent as Ni is deposited. Due to the cylindrical nature of the electroformed composite in this work, the area is constantly changing. As Ni is deposited onto the rotating wire, the diameter is constantly increasing. To account for this, the growth of the composite was modeled based on a plating rate of 1.095g/A-hr at 96.5% efficiency. Based on this model, stepped increases in current where determined to maintain a current density at the cathode within the chosen range of 0.02-0.04 A/cm^2. Although this current density added a small amount of compressive stress in the matrix, this low current density was needed to minimize surface roughness during fabrication.

This model also took into account the incorporation of the $BaTiO_3$ reinforcement which adds to the composite volume increasing the diameter of the sample without consuming the supplied current. With this stepped increase in current density comes a stepped increase in the rate of Ni deposition and along with this comes increased consumption of $BaTiO_3$ particles from the plating bath. To maintain a constant particle concentration in the electrolyte, timed 0.21g particle additions were made to the bath to maintain a constant particle concentration in the range of 0.01-0.07g/L using a Lambda Powder Doser. The surface roughness induced by the incorporation of the reinforcement particles led to severe dendrite formation causing samples to be unusable. To reduce this effect, the center 4 mm of each sample was deposited without particle additions and no test bars where cut from this portion of the composite.

In this manner, the composites were grown over 8-13 days, depending on volume fraction barium titanate, as this portion is simply added and not "grown", a composite of higher volume fraction reinforcement will take less time to produce at the same current density. The composites were 125 mm long with a diameter of ~13 mm measured at the valleys of any surface roughness. An example can be seen in Figure 28.

Figure 28. Electroformed nickel sample having 0v% BaTiO$_3$

A disc shaped cross section was then cut from each end and one from the center for metallographic analysis as shown in Figure 29, leaving two cylindrical pieces roughly 55 mm in length.
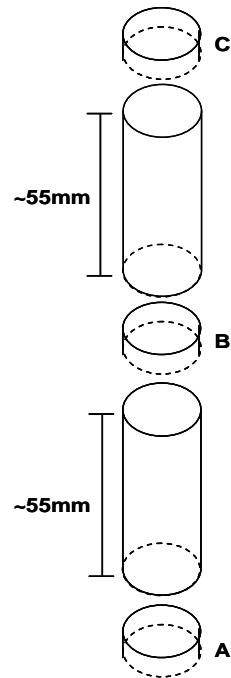
Figure 29. Sample sectioning schematic

Eight, two-by-three millimeter bars were electrical discharge machined from the outer composite portion of each cylindrical piece which was grown about a pure Ni core as shown in Figure 30.
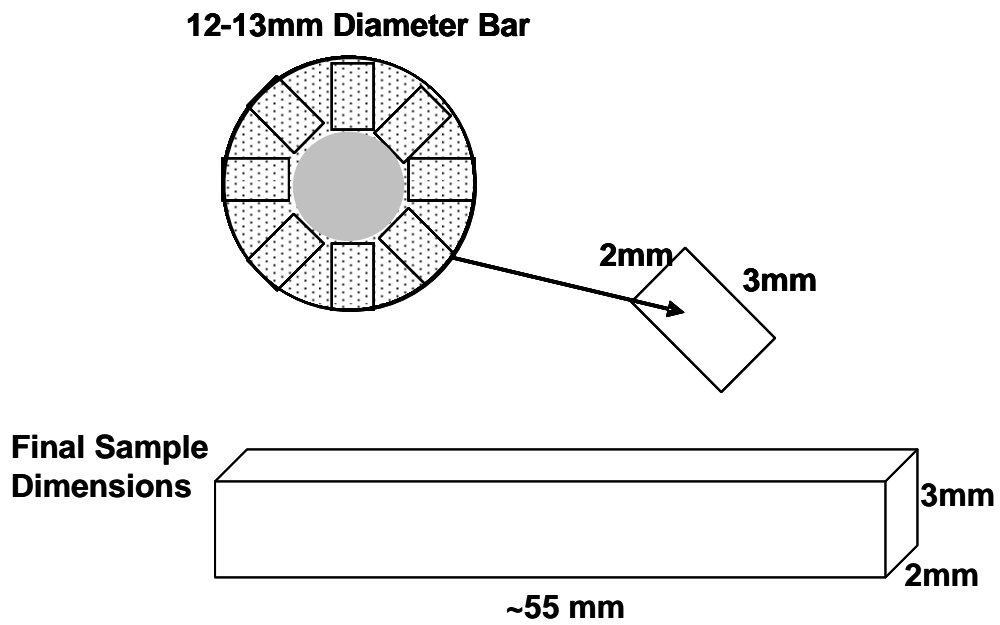

Figure 30. Schematic describing the manner in which test bars were cut from the electroformed composite cylinders

Cutting the samples in this manner ensured a consistent structure as the grain structure tended to be radially columnar from the center.

5. Polished Specimen Preparation

After consolidation, specimens from each composite were mounted in 2-part epoxy resin and cured overnight at room temperature. Samples of the plated $BaTiO_3$ powder were also mounted in this manner. Each mounted sample was ground using 240, 400, 600, and 1200 grit paper and polished using 1.0, 0.3, and 0.05 µm Al_2O_3 suspensions. This allowed for the examination of the cross-section of both the composite discs and the plated particles using electron microscopy.

6. Scanning Electron Microscopy

Backscattered scanning electron microscopy (SEM) was used to examine the plated $BaTiO_3$ powder as well as the structure of the composites. Here, the features of primary importance included porosity in the matrix, reinforcement, and at the matrix/reinforcement interfaces. The backscatter detector is sensitive to contrast between phases of different average atomic number.

7. Reinforcement and Porosity Volume Fraction Calculations

Although the fabrication parameters of the FR-MMCs in this work was based on a growth model according to a desired volume fraction, variation of up to 5 volume percent was common and thus the resultant volume fraction of each sample had to be measured. To do this, a 2-3 mm thick section was cut from the top (C), bottom (A) and middle (B) of the composite cylinder, as shown previously in Figure 29.

 These sections were then metallographically prepared and polished according to section 5 of this chapter and four representative pictures were taken of each section, generally one from the top, bottom, left side and right side.

These pictures were then analyzed using Image J. Image J is a public domain, Java-based image processing program developed at the National Institutes of Health. It was used to first transform these images into a black and white binary form, as in Figure 31.
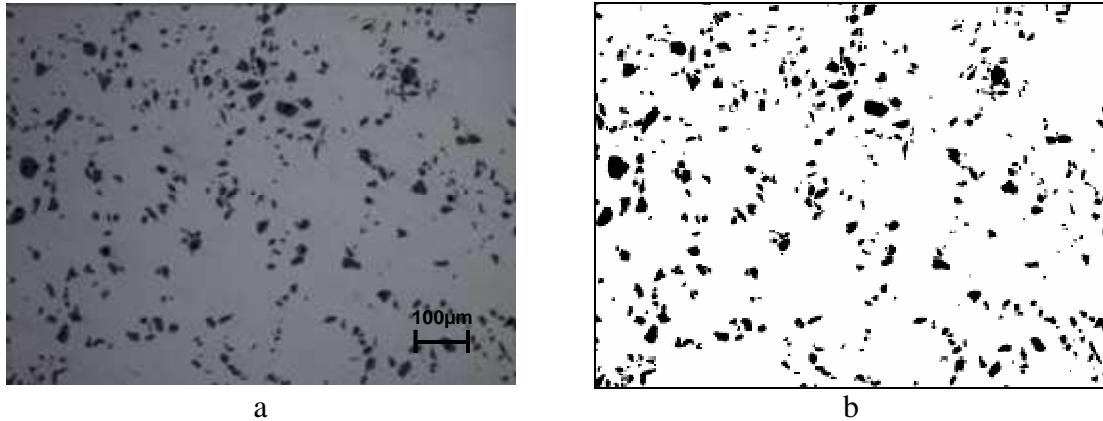

<p style="text-align:center;">a   b</p>

Figure 31. Cross-sectional images of an electroformed Ni FR-MMC a.) Image as taken b.)Image made binary using Image J

With a binary image, the number of black pixels (reinforcement) is counted and the volume fraction of black pixels to total pixels corresponds with the volume fraction of the reinforcement in the composite. This was done for all four pictures of each of the three sections, and these 12 measures were averaged to obtain the reinforcement volume fraction for each composite.

In the case of the heavily loaded Ni composites, the volume fraction of porosity also had to be taken into account as only nonporous sections were used to measure volume fraction $BaTiO_3$. The volume fraction of the porosity was also measured in a similar way using Image J. An image of the full composite cross section was made binary, as shown in Figure 32,
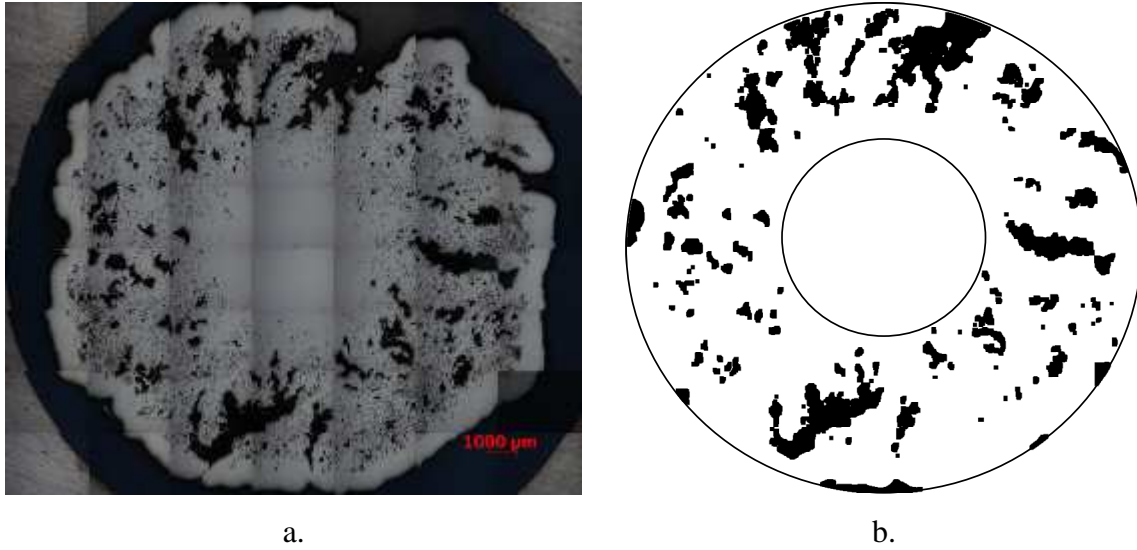
a.	b.

Figure 32. Cross-section of a Ni- 12v%BaTiO$_3$ composite a.) as taken b.) made binary

and the volume fraction of porosity was considered as the part of the Ni matrix when adjusting the reinforcement volume fraction.

8. Differential Scanning Calorimetry

Differential scanning calorimetry (DSC) was performed on both the plated and unplated BaTiO$_3$ reinforcement particles as well as each of the composites. This was done to ensure that the BaTiO$_3$ remained in the ferroelectric tetragonal phase which is responsible for ferroelastic damping in the systems. A TA Instruments Q1000 DSC was utilized in this work. The samples underwent two heating and cooling cycles in a He atmosphere between 25° to 200°C at a rate of 5°C/min. Data was taken the entire time to capture the peaks due to the phase change at the Curie temperature of ~130°C.

9. Mechanical Testing

This is done chiefly to identify the yield strength of the composite to be used as a guide in ensuring that all damping measurements take place within the elastic region. These data may also useful to gauge the quality of the composites.

Stress/strain (s/s) analysis was performed using a TA.XT.Plus Texture Analyzer (TA) with a 50kg load cell and a knife blade three-point bend clamp kit. Stress/strain

calculations, based on the signals of force and displacement, are made using three-point bending equations included in the software package provided with the TA. The end result is a curve representing the maximum s/s, which occurs at the top (compression) and bottom (tension) edges at the midspan of the sample.

The displacement rate 0.6 mm/min of each sample was loaded to 2 cm of displacement or failure, depending on which came first. The s/s curves were also utilized in determining the appropriate strain to be used during dynamic mechanical analysis. To obtain accurate an measure of damping ability, it is necessary to insure that tests are done well within the elastic region of the composites.

9.1 Stress/Strain Calculations in Three-Point Bending

In three-point bending, since the actual stress and strain varies through the sample cross section, the TA produces a stress/strain (s/s) curve based on the σ_{max} and ε_{max} in the sample. This is logical, as one would expect a sample to fail at the point of greatest s/s.

In three-point bending, assuming a homogeneous specimen free of significant stress concentration sites, the maximum stress (σ_{max}) and maximum strain (ε_{max}) occur respectively on the top and the bottom surface of the sample at the midspan.[65] This is where the TA drive applies the load (P) causing deflection (δ), as illustrated in Figure 24.
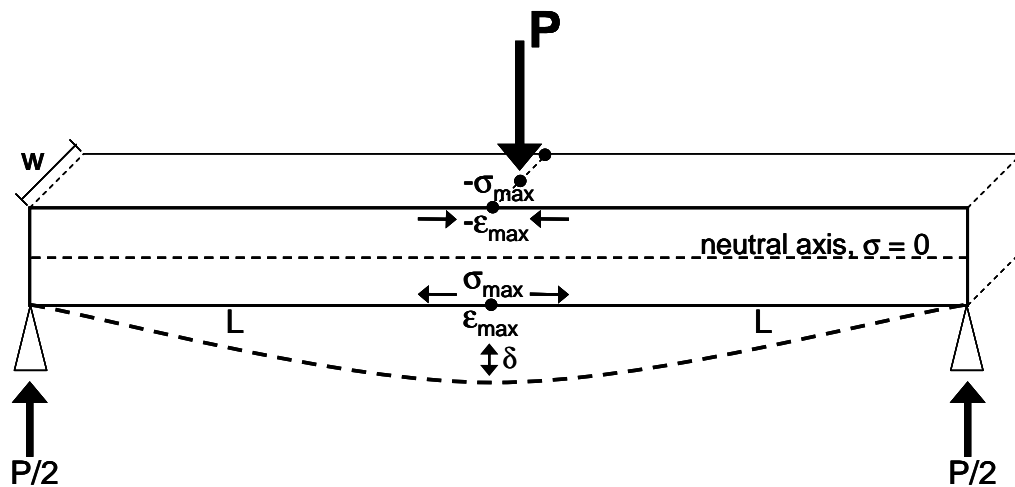

Figure 33. Location of maximum stress and strain of a member in 3-point bending

The TA measures the raw signals of applied force and displacement. These, combined with the sample dimensions and Poisson's ratio, were used by to obtain the maximum stress and strain experienced by the sample using Eqs. 31, 32 and 33.

$$\sigma_{max} = \frac{PLt}{4I} = \frac{3PL}{wt^2}$$
[31]

$$S = K \frac{L^3}{6I} \left[1 + \frac{6}{10}(1+v)\left(\frac{t}{L}\right)^2 \right]$$
[32]

$$\varepsilon_{max} = \frac{6\delta t}{2L^2 \left[1 + \frac{6}{10}(1+v)\left(\frac{t}{L}\right)^2 \right]}$$
[33]

In Eqs. 31, 32 and 33, P is the load. L is one half of the sample length. t is the sample thickness. I represents the moment of inertia. w is the sample width. δ is the deflection. v is the Poisson's ratio of the sample material, and S is the slope of the stress/strain curve.

For the linear (elastic) region of the curve, S is a constant value which corresponds with the elastic modulus (E). This allows the use of Hooke's law to relate σ_{max} and ε_{max} for the entire linear region of the s/s curve. Once plastic deformation begins and the curve strays from linearity, S can no longer be treated as E, and thus S can no longer be used to relate σ_{max} and ε_{max} between data points. It does however remain the slope of the curve for each individual point on the curve and can therefore be used to relate σ_{max} and ε_{max} at each data point. This distinction between S as the elastic modulus (E) versus S being treated simply as the slope of the curve at any point should be noted in the derivations of Eqs. 31, 32 and 33, which are given in Appendix A.

10. Damping Behavior Evaluation

The damping behavior was examined and used to better understand the behavior and limitations of ferroelastic domain twinning as an energy dissipating mechanism in the composite system studied. Dynamic mechanical analysis (DMA) was used to

characterize the relative damping properties of both the bulk $BaTiO_3$ and the FR-MMCs. All tests were conducted using a TA Instruments model Q 800, using the 50 mm roller-edged three-point bend clamp kit.   For each sample the static strain was set to 0.05%, and the ratio of static/dynamic strain was configured at 1.25. Here, a resulting maximum strain of 0.09% was applied. This strain level falls well within the elastic region of these materials while maintaining stresses within the active region of 15-100 MPa[3] for ferroelastic damping mechanisms. The dynamic strain was driven at 1 Hz.

10.1 Damping vs. Frequency

Tan δ was measured at room temperature from 0.01 to 20 Hz in an effort to further the understanding of the dependence of ferroelastic damping (twinning) on frequency. From these results the drive frequency of 1 Hz was chosen as it fell into the most stable region of the curve avoiding resonance which could be a significant source of variation in the damping results with the potential to mask variation seen between samples of dissimilar volume fraction $BaTiO_3$.

10.2 Damping Properties vs. Temperature

Each run began with a temperature equilibration at 25^oC, at this point data collection was turned on. Once data was being collected, the sample was held at 25^oC for 0.25min followed by a temperature ramp at 3^oC/min to 200^oC. Upon reaching 200^oC, the sample temperature was held for 1min. Data collection was then turned off and the sample was cooled to 25^oC at 3^oC/min under no load. For each sample this process was repeated twice. Data was collected during the first run but not used in the analysis as this run was simply used to erase any processing history that the sample may have had. Further discussion of DMA in general is addressed in the Background section of this thesis.

10.3 Reversible vs. Irreversible Damping

Tan δ was measured at room temperature from 1 to 30,000 cycles in an effort to discover the quantity of ferroelastic twinning that is reversible vs. irreversible. It is expected that

the *tan δ* should drop off with increasing cycles as more ferroelastic twins become pinned which could limit the effective service life of the FR-MMCs.

11. Neutron Diffraction

As part of a larger study by Schultz et. al., which includes the author of this work, neutron diffraction was used to verify ferroelastic domain motion as an active damping mechanism in FR-MMCs.[44, 66] These tests, were performed on the Spectrometer for Materials Research at Temperature and Stress (SMARTS) at the Los Alamos Neutron Science Center (LANSCE).

In the electroformed Ni-BaTiO$_3$ composite system, BaTiO$_3$ tetragonal peaks are eclipsed by the primary Ni peaks of the matrix, and neutron diffraction studies could not be performed. In the case of the bronze matrix composites, 30v% BaTiO$_3$ composite samples were subjected to an oscillating stress state (±10 MPa) about a static compressive stress of 30 MPa at room temperature while in the path of the neutron beam. This led to a maximum stress state of 40 MPa, well within the elastic region of the composite. The sample was subject to 50 cycles at 1 Hz. Five diffraction patterns were taken during cycles 1, 2, 5, 10, 25, and 50. To facilitate a sufficient neutron count, the cyclic loading was paused for ~1 hour while obtaining each diffraction pattern. One was take at the maximum stress (40 MPa), one at the minimum stress (20 MPa) and one each time the static stress of 30 MPa was crossed.

Figure 34 shows a bronze- 30v% BaTiO$_3$ composite sample loaded into the load frame at SMARTS. Around this is the high temperature furnace unit. The squares embedded into the furnace are Al windows that are virtually transparent to neutrons allowing the beam to pass into the furnace to the sample and back out to the detectors.
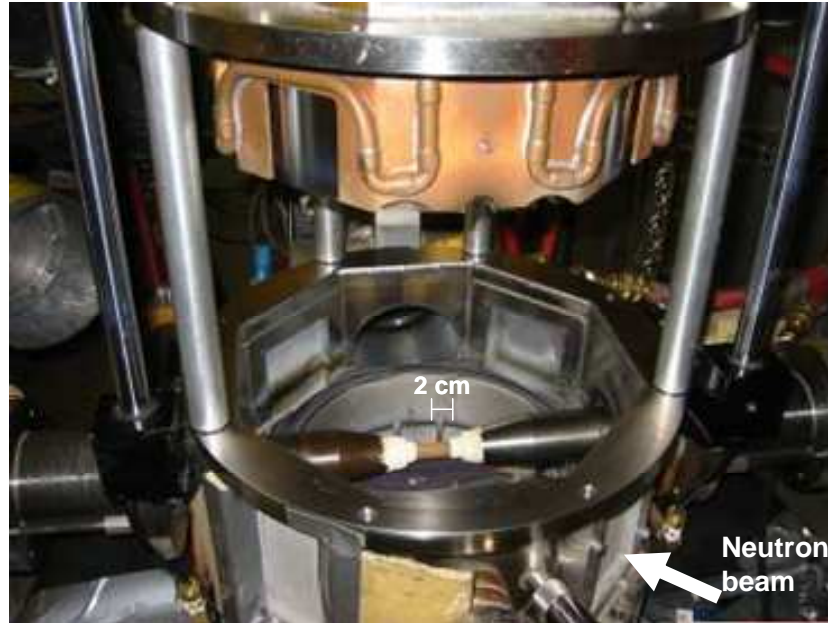
Figure 34. Bronze- 30v%BaTiO3 sample inside the load frame of SMARTS at LANSCE

Here the focus was on data from detector bank 2. For the purpose of twin identification, both detectors provide similar information, however the peak sharpness greater in detector 2 as the diffraction neutrons mass through more of the sample material which act to filter stray neutrons that have been incoherently scattered toward the detector. The scattering vectors for detector 2 can be seen in Figure 35.
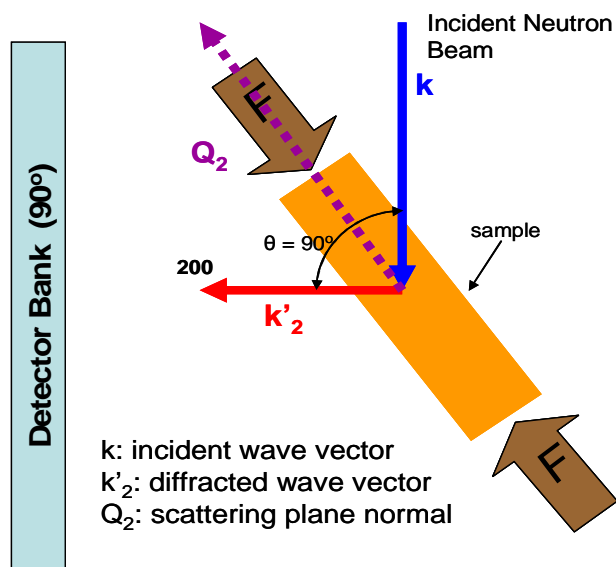

Figure 35. Scattering vector schematic for detector 2

Those atomic planes in the sample having plane normals equal to vector Q2 will scatter neutrons from the incident beam into detector ban 2. For the tetragonal structure of BaTiO$_3$, this corresponds to the "c" and "a" lattice parameters which are perpendicular to the loading direction.
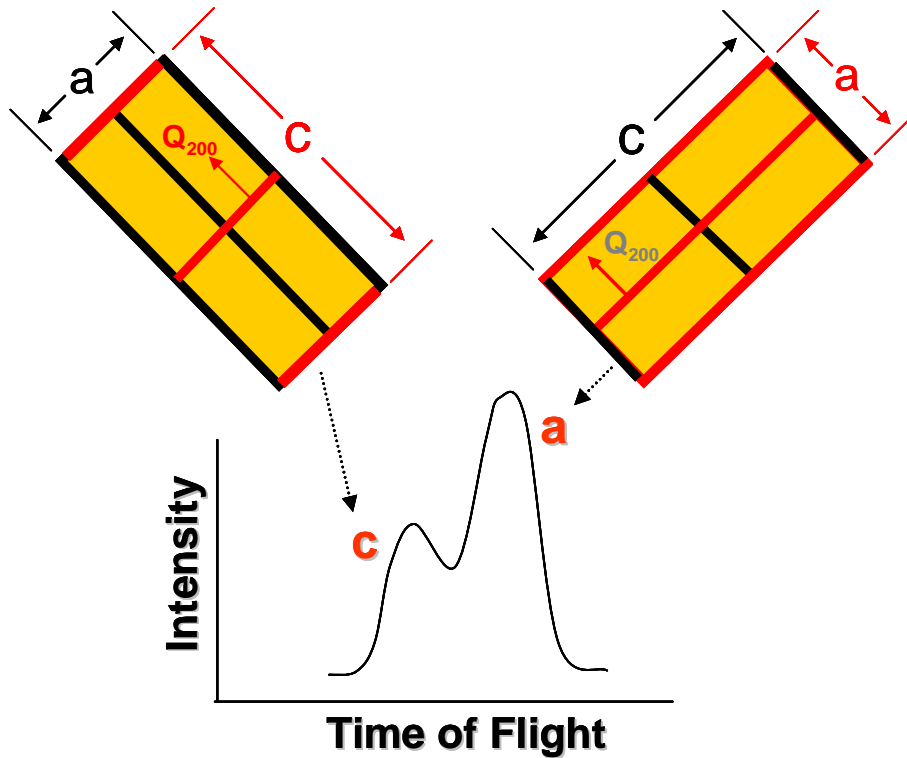

Figure 36. Diffraction planes in BaTiO$_3$ and their intensity peaks in the resulting diffraction pattern

These diffraction planes are shown in red in Figure 36 and there presence is quantified through their normalized peak intensities. Due to the symmetry of the tetragonal structure of BaTiO$_3$, the intensities of these peaks will maintain a ratio of 2:1 as 2 a axes exist for each c axis.

When stress is applied to the composite sample, a portion of the c axes which are aligned parallel to the loading direction will switch by 90° to avoid compression of the elongated c axis, Figure 37.
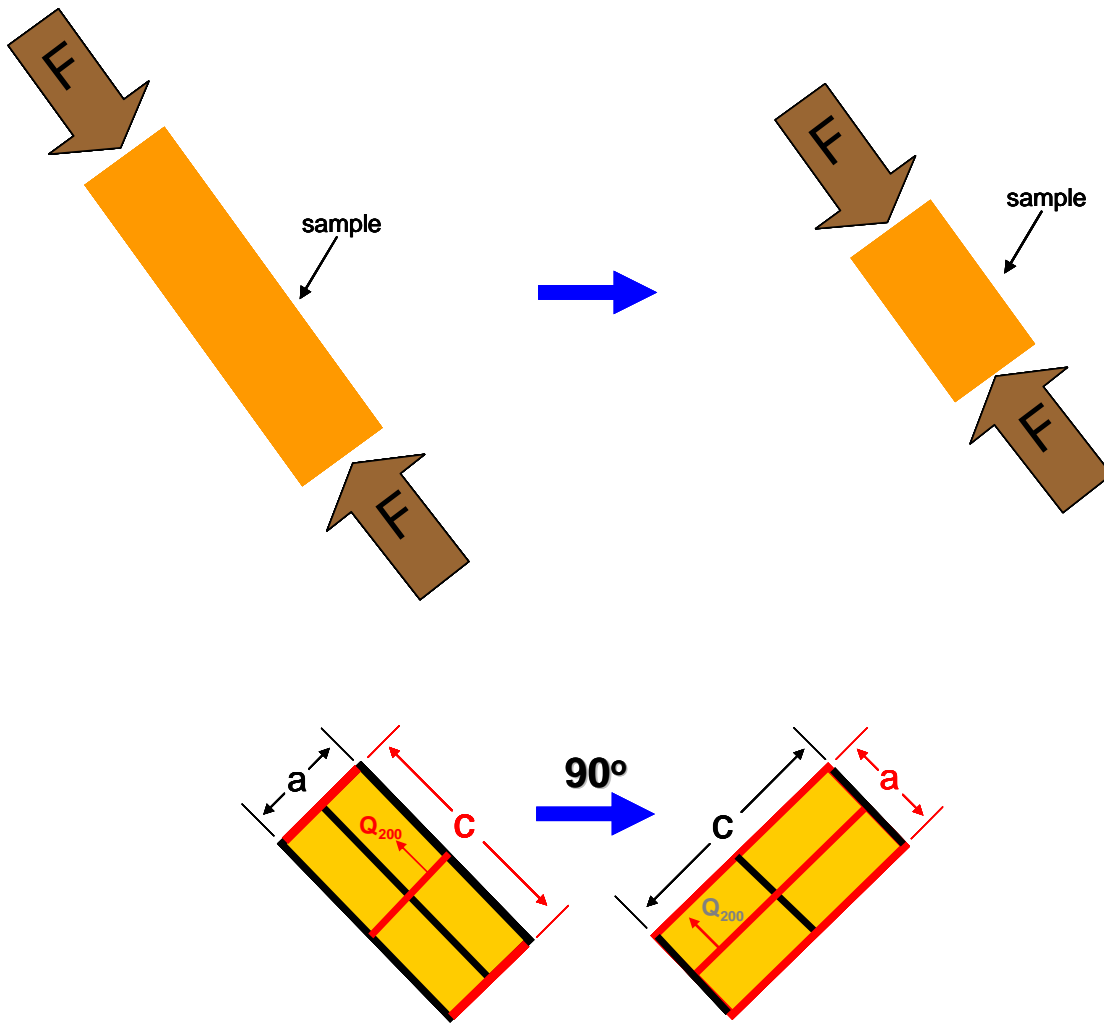
Figure 37. Stress induced switching of the c axis in tetragonal BaTiO₃

This switching is physically manifested as twinning in the material and can be quantified by the trade-off in intensity seen from the "c" to the "a" axis in the diffraction pattern, Figure 38.
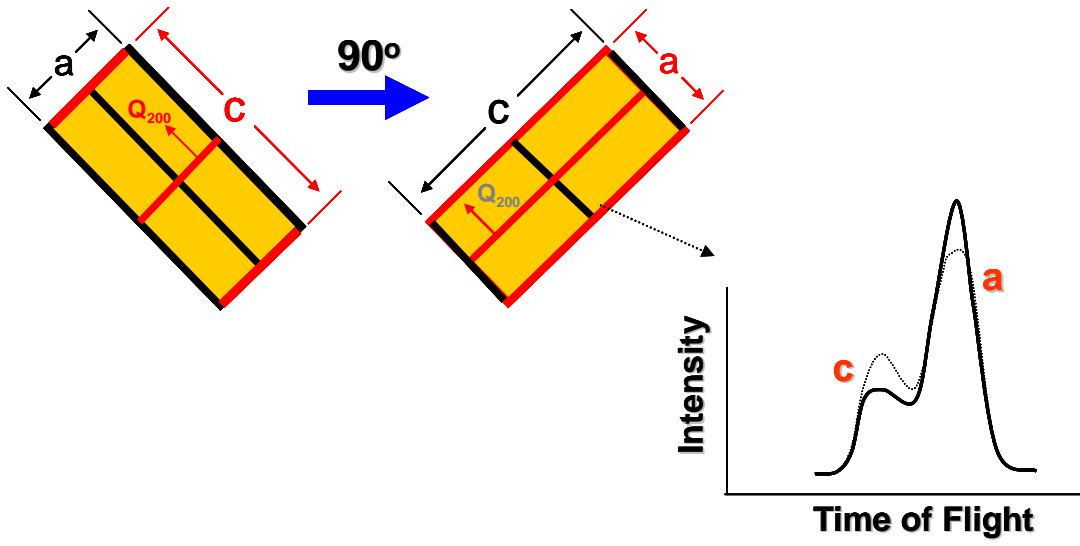
Figure 38. Stress induced intensity trade-off from the parallel c axis to the a axis

Chapter Four- Results and Discussion

1. Preparation of the BaTiO$_3$ Reinforcement Powder

The BaTiO$_3$ powder was successfully ground and sieved from 3-12mm pieces into a uniform, free-flowing -325 +500 powder.   During this process roughly 50% was lost as -500 mesh fines (<30µm particles). Here, approximately 1 gram of barium titanate powder was dispersed in deionized water and suspended by the flow of water through a loop, while laser scattering was used to analyze the particle size distribution of barium titanate particles yielding a median diameter of 35.475 µm.

As can be seen in Figure 39, the as-received 3-12mm pieces appear to consist of a network of 20-100µm grains dispersed into a highly porous, fine-grained structure.
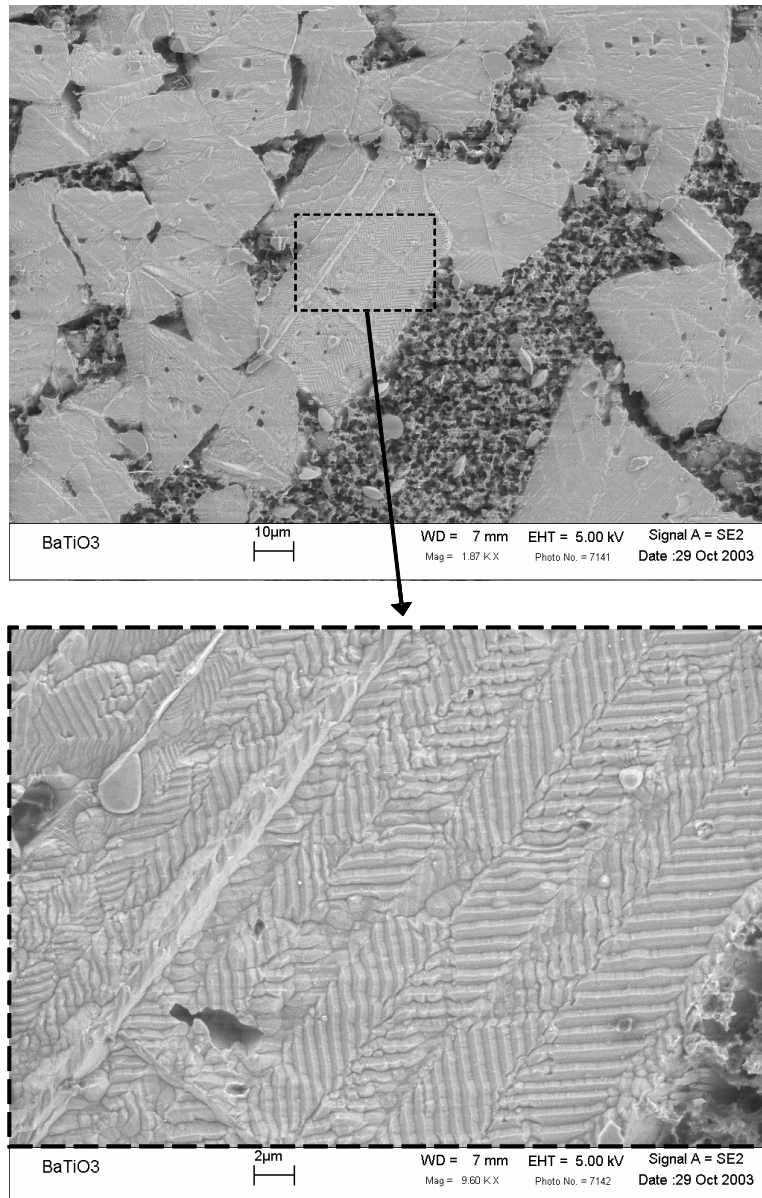
Figure 39. SEM image of the domain structure of the as-received BaTiO$_3$ 3-12mm pieces

This morphology is likely responsible for the relative ease of grinding as most of the fracture is occurring in the porous regions between grains. Within the grains a prominent herring bone domain structure can be observed. This consists of ferroelectric 180° domains which are heavily twinned by ferroelastic 90° domains. This structure is near ideal as it is the motion and creation of these 90° domains within a coarse grain structure (>1µm) that is responsible for the ferroelastic damping examined in this work.[1]

After grinding and sieving, DSC was used to verify that the powder remained ferroelectric/ferroelastic. Peaks at the Curie temperature (130°C) upon heating and cooling can be seen in Figure 40.
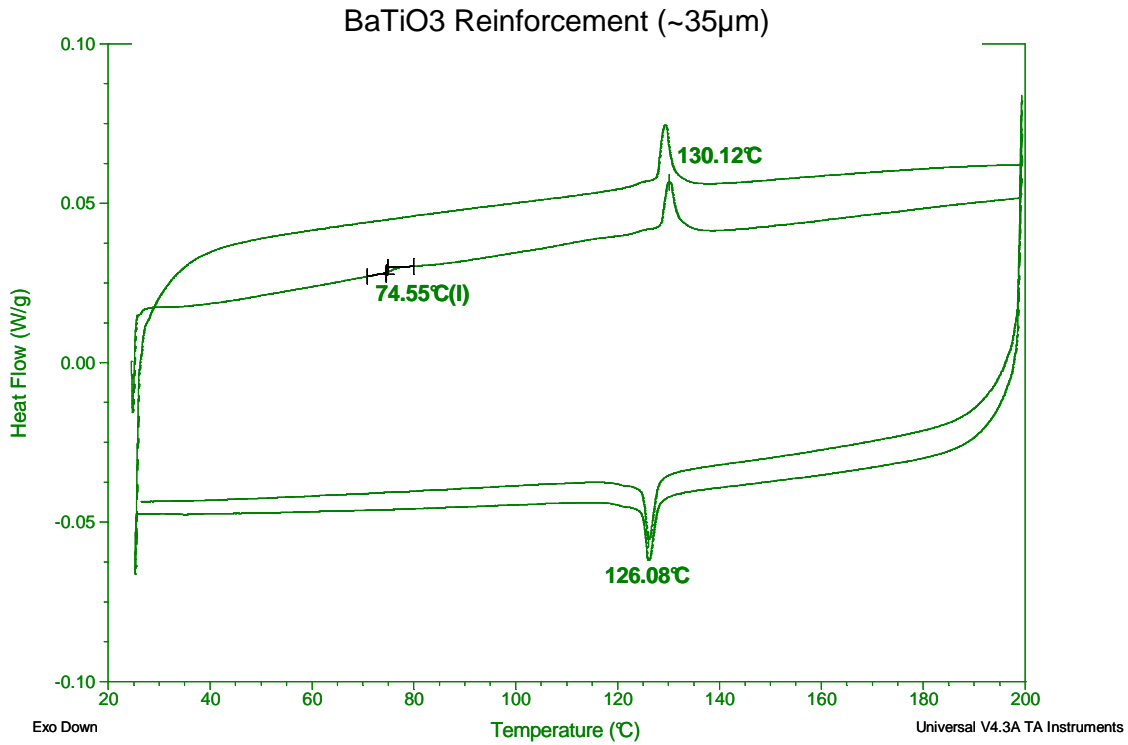

Figure 40. DSC data for the ground and sieved BaTiO$_3$ reinforcement powder for heating and cooling during two cycles

These peaks represent the ferroelectric to paraelectric phase change upon heating through the Curie temperature (T_C) and the paraelectric to ferroelectric phase change upon cooling through T_C. The heating peak verifies that the powder remains ferroelectric after grinding. While the presence of both peaks is evidence that the phase change remains reversible with the current particle size, structure and morphology.

1.1 Electroless Copper Plating

Electroless plating of the BaTiO$_3$ reinforcement resulted in a uniform copper coating while maintaining the free-flowing properties of the powder.

Figure 41. Unplated vs. electroless Cu plated BaTiO$_3$ reinforcement powder

This resulting uniform Cu coating has a thickness of 3-4µm, as shown in Figure 42.
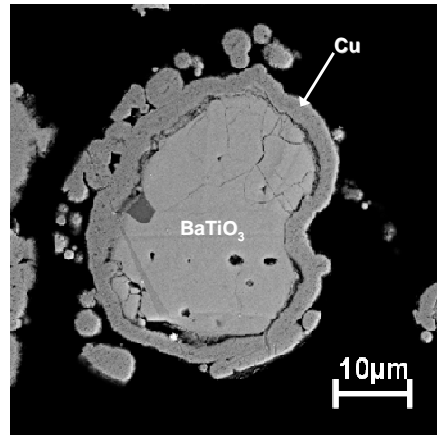

Figure 42. SEM image of a copper plated BaTiO$_3$ particle

Although there appears to be a separation between the plated layer and the particle, this is an artifact of the sample preparation. During polishing, the BaTiO$_3$ is worn away at a faster rate than the surrounding copper resulting in their surfaces resting on different planes. As a result the BaTiO$_3$ is shadowed causing it to appear black in the areas near the plated layer.

DSC analysis of the Cu plated powder confirmed the preservation of the ferroelectric/ferroelastic nature of the reinforcement, Figure 43.
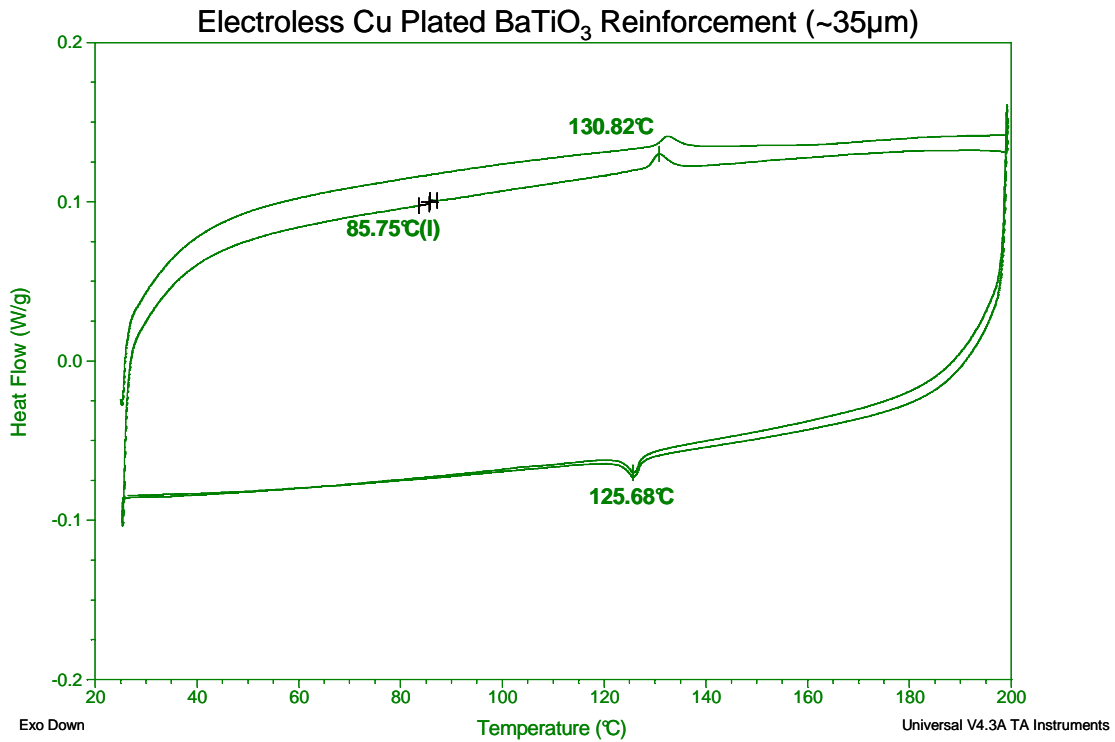
Figure 43. DSC data for the Cu plated BaTiO$_3$ reinforcement powder

The presence of both peaks is evidence that the phase change remains reversibly ferroelectric after the series of chemical treatments involved in the plating process.

1.2 Electroless Nickel Plating

Electroless plating of the BaTiO$_3$ reinforcement resulted in a uniform nickel coating while maintaining the free-flowing properties of the powder.
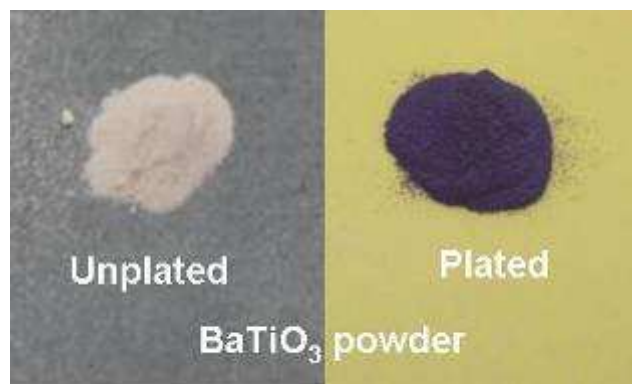

Figure 44. Unplated vs. electroless Ni plated BaTiO$_3$ reinforcement powder

This resulting uniform Ni coating has a thickness of 3-4µm, as shown in Figure 42.
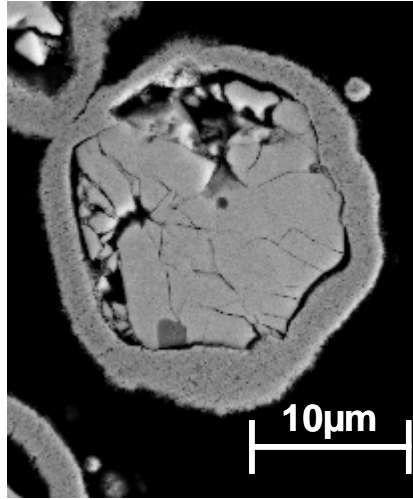
Figure 45. SEM image of a nickel plated BaTiO$_3$ particle

Again the separation between the plated layer and the particle is an artifact of the sample preparation. During polishing, the BaTiO$_3$ is worn away at a much faster rate than the surrounding nickel resulting in their surfaces resting on different planes. As a result the BaTiO$_3$ is shadowed causing it to appear black in the areas near the plated layer.

As for the Cu plated particles, DSC analysis of the Ni plated powder confirmed the preservation of the ferroelectric/ferroelastic nature of the reinforcement during plating, Figure 46.

Figure 46. DSC data for the Cu plated BaTiO$_3$ reinforcement powder
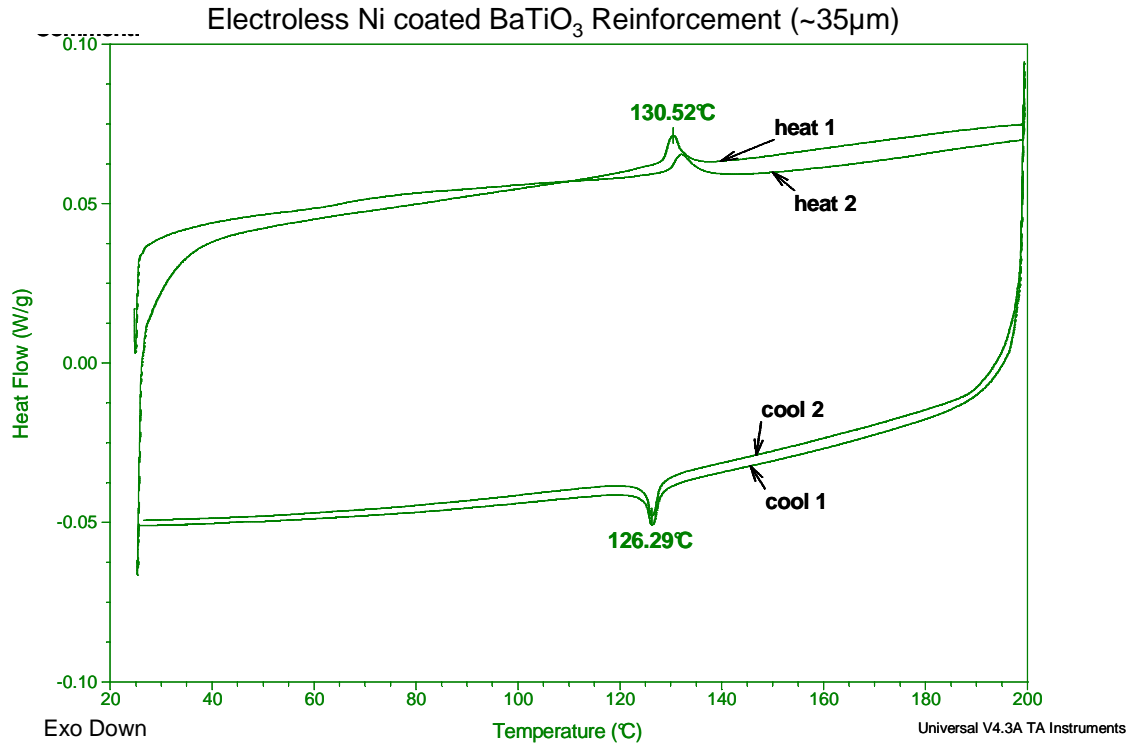
The heating peak verifies that the powder remains ferroelectric after plating, while the presence of both peaks is evidence that the phase change remains reversible after the series of chemical treatments involved in the plating process.

2. Composite Structure

As previously mentioned, the composite structure plays a key role in the amount of stress transfer that exists between the matrix and reinforcement. As the key damping mechanism is active only in the reinforcement particles, structure is extremely important when attempting to maximize ferroelastic damping in FR-MMCs.

2.1 Sintered Bronze-BaTiO$_3$ System

To evaluate damping ability in FR-MMCs, a straightforward fabrication method allowing for the creation of composites having specific volume fractions of reinforcement was

needed. As specific amounts of matrix and reinforcement can be combined and sintered, traditional powder metallurgical methods were selected. Copper was initially chosen as the matrix material, as elemental Cu can be sintered at ~900-1050°C.[27, 63] This range is much lower than that for other structural metals such as Ni, Ti, Fe and Mo. Cu is also much less reactive than lower melting point, structural metals such as Al and Mg. To further reduce the sintering temperature, an alloy of Cu- 10 w% Sn (bearing bronze) was finally selected for the matrix metal. This alloy can be liquid phase sintered at 820°C and is resistant to oxidation leading to greater ease in lab handling.

Barium titanate (BaTiO$_3$) became the obvious reinforcement material on the basis of thermodynamic stability and high damping ferroelastic nature. Many of the current Pb based ferroelectric ceramics (PZT, PLZT, PMN, etc.) are unstable in most structural metals, such as Fe, Ni, Al, and Cu-Sn bronze, at temperatures above 300°C, as manifested by excessive reactions between the metal matrix and the reinforcement. BaTiO$_3$ also has a distinct Curie temperature (T_C), associated with the tetragonal-cubic phase change near 130°C.[36] This is opposed to the gradual transition typical of Pb-based solid solutions, and allows for quantification of ferroelastic damping through the comparison of data just before and after T_C.

In this work, the barium titanate (BaTiO$_3$) particles were electrolessly Cu plated before incorporation into the bronze matrix and were pressed and sintered twice to improve the M/R interface and decrease porosity. With this improved structure, the mechanical and damping properties of the resulting ferroelectric reinforced metal matrix composite (FR-MMC) could be better investigated.

Metal-particle interface

In previous work,[4, 7-9] FR-MMCs have been produced using the powder metallurgy (PM) route. However relatively poor physical and mechanical properties were obtained due to the existence of large amounts of residual porosity which tended to agglomerate at the matrix/reinforcement (M/R) interface. This is not unusual, and is thought to be the result

of both the non-wetting characteristics between the metal matrix and the ceramic
reinforcement and porosity from incomplete consolidation.[5, 67] Plating of the particles
has been shown to reduce this problem.[5] An example of such an interface from the
current work is shown in Figure 47, which contains an SEM image of a Cu plated $BaTiO_3$
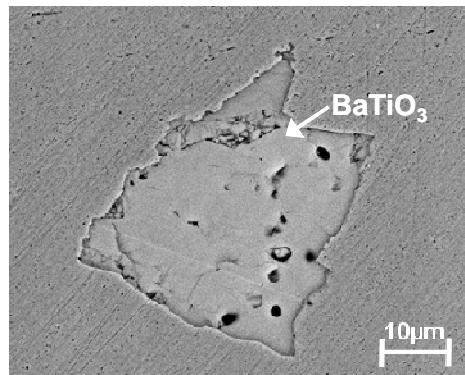particle embedded in a bronze matrix.

Figure 47. Copper plated $BaTiO_3$ particle embedded in a bronze matrix

A sound interface appears to exist across nearly the entire particle surface. As the tin
component of the bronze matrix becomes liquid during sintering, it is able to wet the Cu
surface of the reinforcement, decreasing the tendency for pore agglomeration at the
interface and allowing it to be spread more evenly throughout the composite. Plated
particles not only provide increased M/R interface, but the interface created is also of
higher quality. Here, improved adhesion is realized through the formation of a Cu-Sn
solid solution with the plated layer associated with tin interdiffusion from the bronze
matrix into the Cu layer of the particle.[67]

Overall composite structure

To examine the effect of volume percent reinforcement on composite structure, images of
bronze-$BaTiO_3$ composites of varying v% reinforcement are compared in Figure 48.
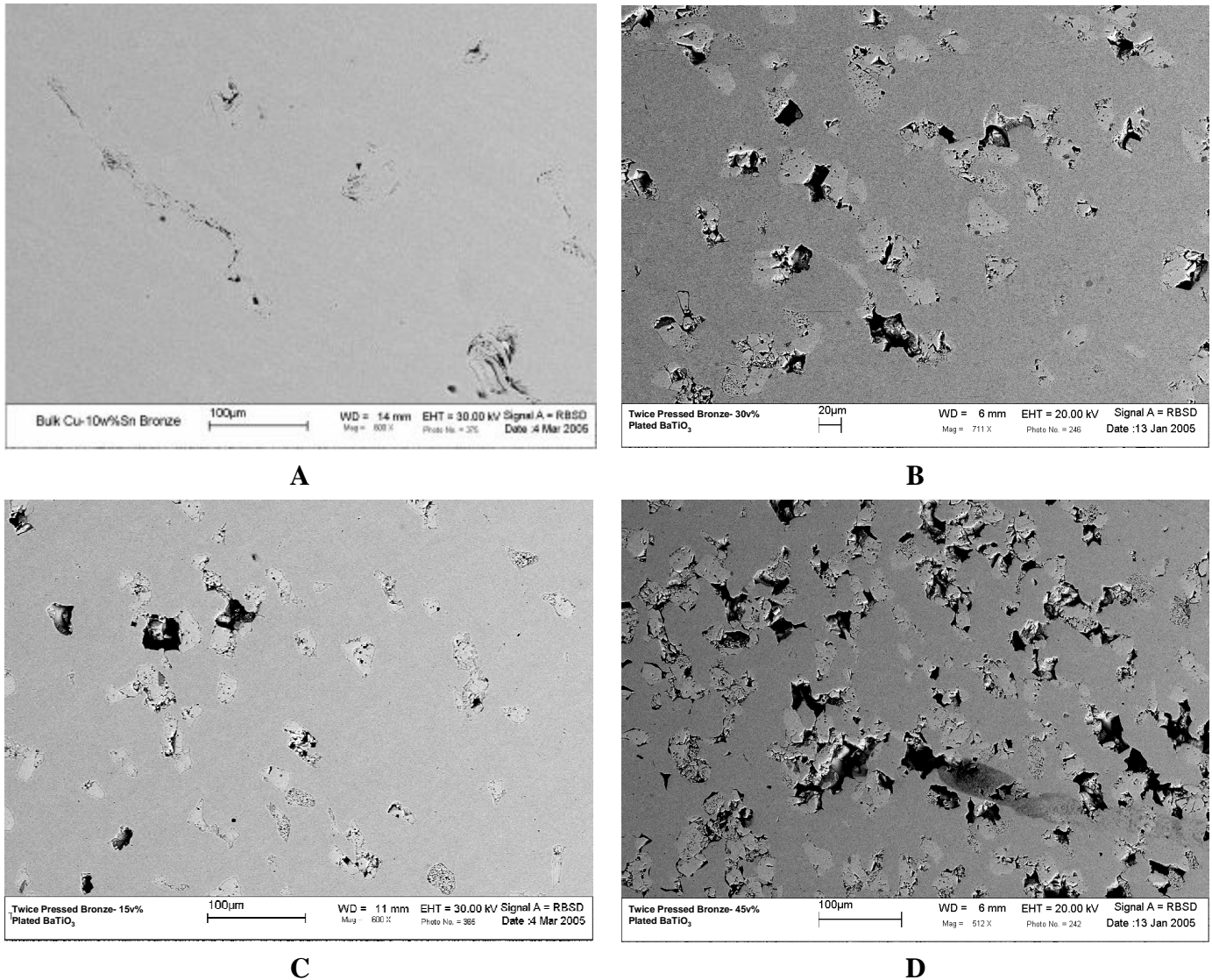
Figure 48. A.) Bronze- 0v% plated BaTiO$_3$, B.) Bronze- 30v% plated BaTiO$_3$, C.) Bronze- 15v% plated BaTiO$_3$, D.) Bronze- 45v% plated BaTiO$_3$

This upward trend in porosity with volume percent ceramic is not unusual. Before sintering, the composite is simply a pressed mixture of metal and ceramic powder. When hard and soft powders are mixed together the compaction behavior is dominated by the connectivity of the hard material.[63] In this work Cu, Sn and BaTiO$_3$ powders having yield strengths of 69MPa[27], 11MPa[68], and 82MPa[23] respectively were combined, therefore, this would cause the pressed green density of the discs to decrease with increasing ceramic BaTiO$_3$ content. Upon sintering, this decreased green density should in turn lead to decreased density (increased porosity) in the composite disks. Although

structural improvements have been made through secondary pressing and sintering and by utilizing plated $BaTiO_3$, the resulting composite continues to be a model system and is still far from ideal.

2.2 Electroformed Nickel-BaTiO$_3$ System

The goal of this work is to further the understanding and the limitations of ferroelastic domain motion (twinning) as the primary damping mechanism inherent to FR-MMCs. In order to further characterize this mechanism, efforts have been made to fabricate FR-MMCs consisting of materials other than the bronze-BaTiO$_3$ system. Due to incompatibility issues surrounding most other material combinations, a near room temperature processing technique was chosen. Here, Ni (matrix) plus BaTiO$_3$ reinforced metal matrix composites were fabricated through electroforming.   Electroforming of composites, also known as occlusion or composite plating, does not require the high temperatures and pressures involved in more traditional methods, such as internal oxidation, powder metallurgy, high pressure bonding, and infiltration.[61] The high processing temperatures involved during sintering has restricted the ability to independently vary process variables due to reactivity between most structural metals and ferroelectric ceramic combinations.

Using this method, reinforcement particle diameters can range from 0.02-100µm, with the only requirement being that they remain suspended, and particle quantities dispersed in solution generally vary from 50-200g/L.[61] Utilizing traditional electroforming methods, even with such high particle loading of the bath, it is difficult to achieve a high volume fraction reinforcement, especially for large particle sizes. Here, incorporation relies on weak electrophoretic forces to capture a particle at the cathode before ionic species, adsorbed onto the particle, are reduced, incorporating it into the composite. From there sufficient metal has to be plated around the particle sufficient to hold it in place before electrolyte convection can knock it away.[61] To overcome these issues, high particulate loading of the electrolyte is utilized, but this can cause contamination in the bath which can severely affect the platability and properties of the matrix metal.

In this work, electroless Ni plated BaTiO$_3$ particles were suspended into a Ni sulfamate electrolyte and incorporated into the electroformed Ni as it was deposited. The conductive nature of the plated reinforcement assists in its incorporation into the composite, significantly decreasing the required particle loading and leading to a composite with a strong matrix/reinforcement interface. Instead of the particles having to be "caught" by the electroformed Ni layer, as is the case with bare nonconducting ceramic particles, the Ni plated particles actually become electrically connected and part of the cathode upon contact. This causes Ni to be electroformed on and around each particle leading to incorporation after a single contact event with the cathode, decreasing the necessary amount of particles which must be added to the electrolyte from roughly 200 to 0.02g/L and increases the amount of reinforcement that may be incorporated in the composite. This electroless Ni coating also creates a barrier between the reinforcement particle and the Ni sulfamate electrolyte significantly decreasing contamination of the bath.

Metal-particle interface

Here, the Ni matrix and BaTiO$_3$ reinforced composites were fabricated through electroforming. Ni plated BaTiO$_3$ particles were suspended into the Ni sulfamate electrolyte and are incorporated into the Ni matrix as it is electroformed. In Figure 49, an etched sample is shown to accentuate the layering of the electroformed Ni over the embedded particulates.
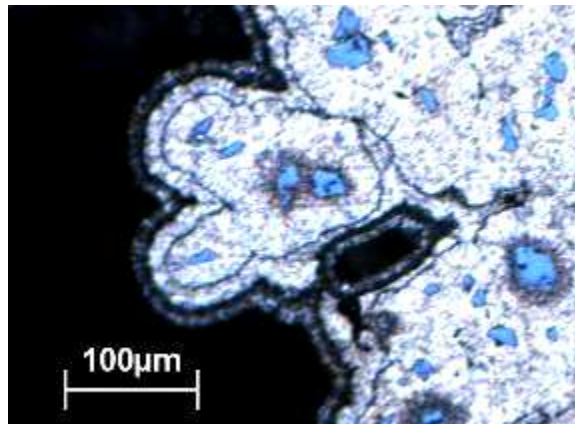

Figure 49. Conductive particle incorporation into the electroformed Ni matrix

Upon contact with the cathode, plating occurs on and around the conductive, reinforcement particles. As they come in contact with the cathode, Figure 50, they assume its charge and effectively become a part of the cathode.
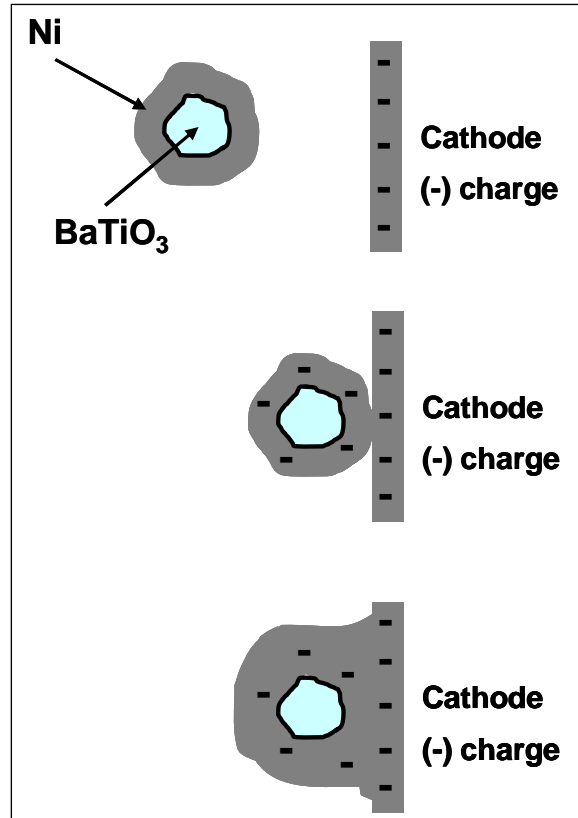

Figure 50. Incorporation of BaTiO3 particles having a conductive Ni coating

This allows for Ni to be deposited over the particulate, fully incorporating it into the composite. Here the Ni coating is chemically and mechanically bonded to the $BaTiO_3$ and seamlessly becomes a part of the Ni matrix leading to a strong M/R interface.

Overall composite structure
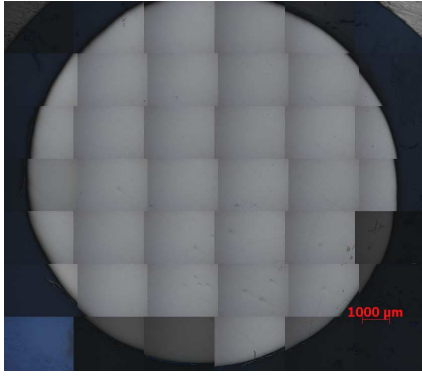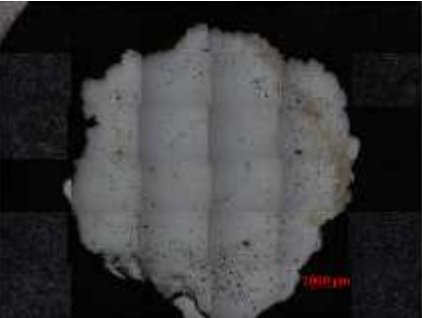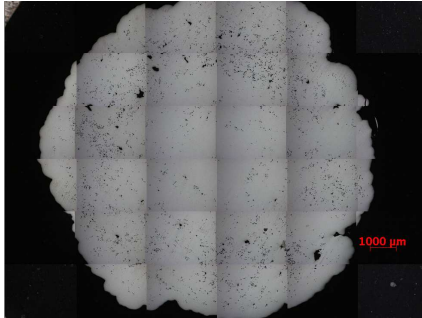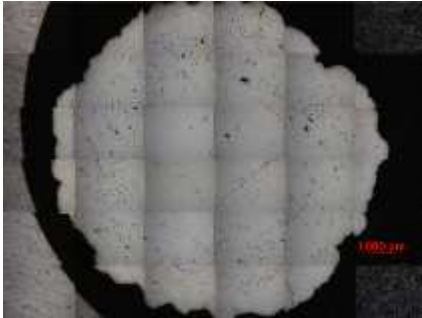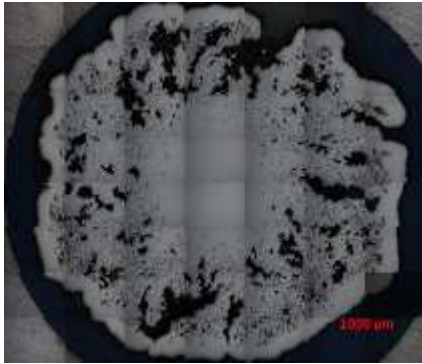
The electroformed Ni composites, as mentioned previously, are grown radially from a rotating Ni wire cathode. The wire is 125mm in length and is grown into a composite rod having a final diameter of 12-14mm. An example can be seen in Figure 51.

Figure 51. Electroformed Ni-BaTiO3 composite rod after fabrication

The curvature seen in this composite bar is not due to residual stress but to slack which occurred in the initial 250 micron Ni wire cathode. From the composite bars, a 5mm tall disc section was taken from the bottom (A), middle (B), and top (C) for characterization. A composite of optical images can be seen in Table 13 of the cross-sections of each of the three composites fabricated in this work.

Table 13. A composite of optical images of the various cross-sections of each of the three composites fabricated in this work: 1.) Ni- 0v% BaTiO3 2.) Ni- 3v% BaTiO3 3.) Ni- 12v% BaTiO3

Bottom, A	Middle, B	Top, C

Composite #1, Ni- 0v% BaTiO$_3$

Bottom, A	Middle, B	Top, C

Composite #2, Ni- 3v% BaTiO$_3$

Bottom, A	Middle, B	Top, C

Composite #3, Ni- 12v% BaTiO$_3$

Here porosity drastically increased with increasing volume percent BaTiO$_3$ adversely affecting the mechanical properties of the composites as will be discussed in the next section. As mentioned previously, the volume percent reinforcement was calculated using optical imagery, as derived from making a binary image and taking a pixel count of the areas containing reinforcement particles. This was done using the image editing software Image J. The results for composites #2 and #3 can be seen in Table 14 and Table 15.

Table 14. Image J volume percent calculations for composite #2

Composite #2					
slice	area 1	area 2	area 3	area 4	average
A (bottom)	3.22	2.51	8.49	1.99	4.05
B (middle)	5.76	2.76	2.67	2.51	3.43
C (top)	2.93	2.05	2.21	3.35	2.63
				Overall volume % BaTiO$_3$	3.37

Table 15. Image J volume percent calculations for composite #3

Composite #3					
slice	area 1	area 2	area 3	area 4	average
A	8.60	11.71	6.81	23.28	12.60
B	23.07	13.24	12.09	8.13	14.13
C	15.97	8.47	21.72	9.86	14.00
				Average volume % BaTiO$_3$	13.58
				Overall volume % BaTiO$_3$, adjusted for porosity (15.20%)	11.79

The volume fraction of composite #1 was 0v%. For composite #2 the volume percent was calculated to be 3.37v% using the selected micrographs, but will be estimated for the remainder of this document as 3v%. The volume fraction for composite #3 was adjusted to take into account the large level of porosity of 15.20%, also calculated using Image J. This adjustment considered the pore area as part of the matrix, effectively decreasing the overall volume percent BaTiO$_3$ from 13.58% to 11.79%. This will be estimated as 12v% in this work.

Examining the composite microstructure there exists a near defect-free bond between the matrix and reinforcement, Figure 52.
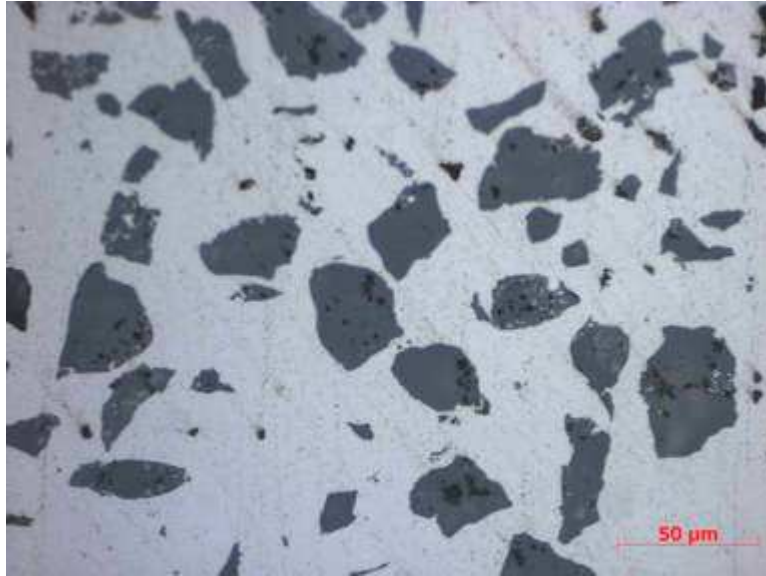

Figure 52. Optical micrograph of the matrix/reinforcement interface

Upon further magnification, Figure 53, the M/R interface appears sounds, however pores of ~5-10µm are found interspersed between and within the reinforcement particles.
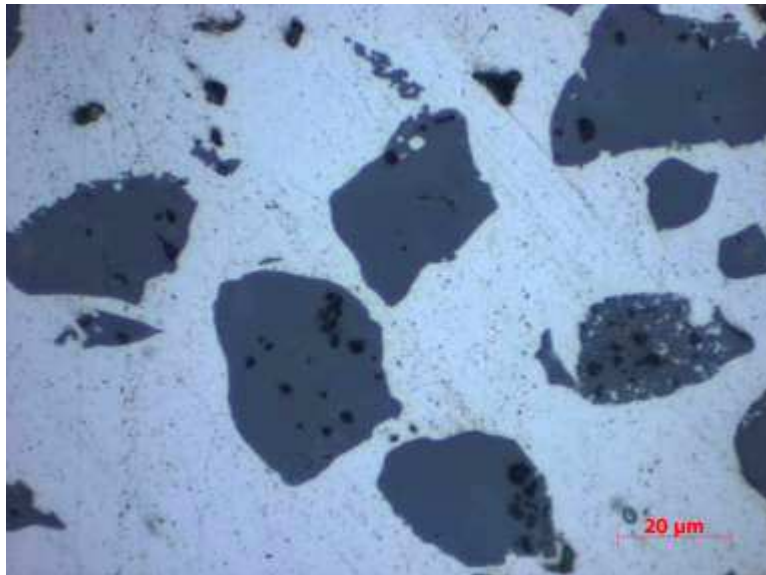
Figure 53. Optical micrograph of the matrix/reinforcement interface of increased magnification

Occasionally these pores do form around the particles at the M/R interface.
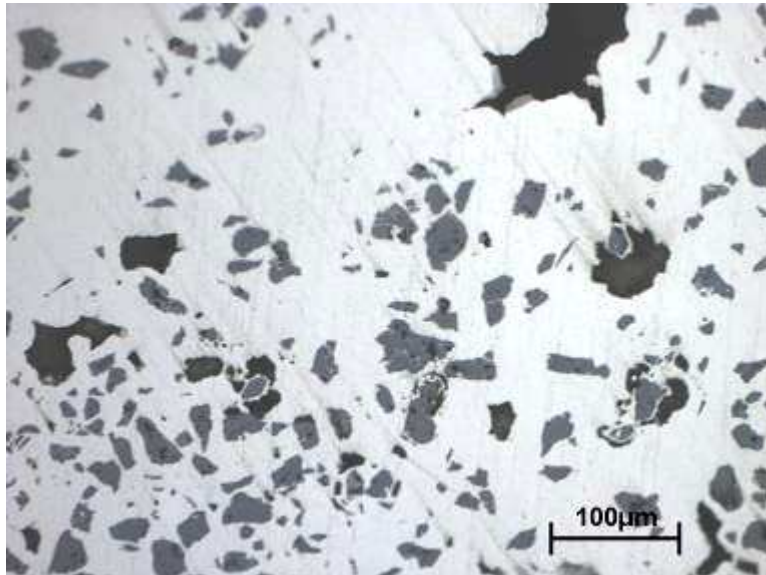
Figure 54. Optical micrograph showing pores at the matrix/reinforcement interface

This generally is found in areas of high porosity and in most cases is cased by meeting of two dendrites between the particle and the anode. This shields the particle from the current supply and halts metal deposition around the particle leaving behind a pore. A similar effect is thought to be responsible for pore formation in the matrix. Evidence of this can be found in Figure 55.
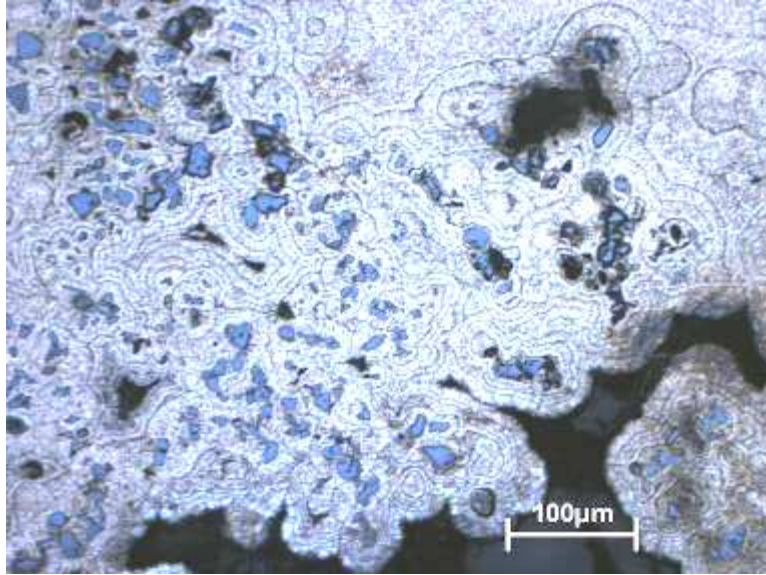
Figure 55. Optical micrograph etched to show pore formation

Here the sample has been etched to reveal the layering of the matrix metal during electroforming. The particles themselves induce dendrite formation by providing surface roughness upon incorporation. These "bumps" become current concentration sites which grow at an accelerated rate out into the electrolyte. Further evidence can be seen in Figure 56.
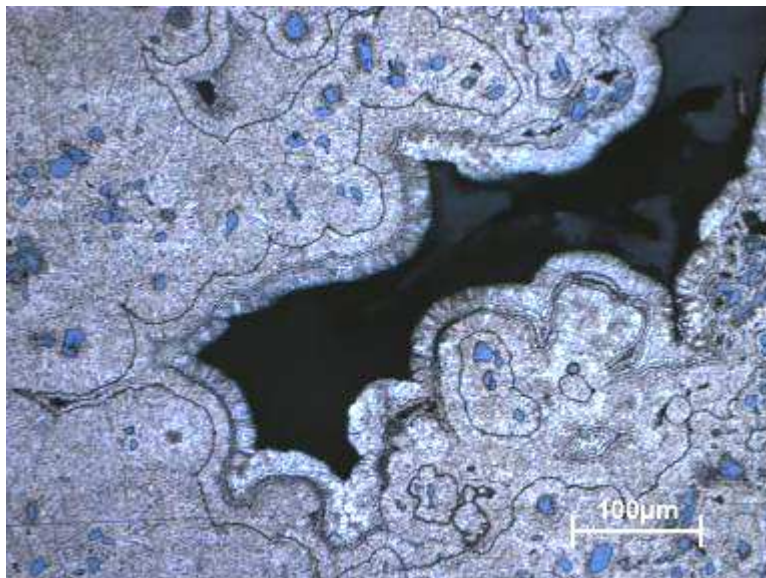
Figure 56. Optical micrograph etched to accent dendrite formation

In this work, uncontrolled dendrite formation created the high porosity found in composite #3, and made the fabrication of composites having increased volume fraction reinforcement nearly impossible. Power supplies with periodic reverse capability could remedy this. Here the polarization is periodically reversed with increased current. The same mechanisms that cause dendrites to form, will drive them to preferentially erode away when the current bias is reversed. This type of rectifier was unavailable for this work.

3. Damping Behavior of the Composites

The goal of this work is to further the understanding and the limitations of ferroelastic domain motion (twinning) as the primary damping mechanism inherent to FR-MMCs. This damping occurs from energy dissipation stemming from the motion of ferroelastic domains which are physically manifested as twins in the tetragonal structure.[1, 43] This damping ability inherent to ferroelectric ceramics can be extended to stiff structural materials through compositing. This section will focus on the effects of frequency (0.01-50 Hz), temperature (25-200°C), and number of strain cycles (0-30,000 cycles) on damping behavior (*tan δ*) for the sintered bronze-BaTiO$_3$ and electroformed Ni-BaTiO$_3$ composite systems. These tests were performed with a maximum strain of 0.09% about a static strain if 0.05%. This strain level maintains stresses within the active region of 15-100 MPa[3, 42] for ferroelastic damping mechanisms, Table 16.

Table 16. Effective stresses in the composites during DMA analysis

Composite	Stress at 0.09% Strain, MPa
Bronze- 0v% BaTiO$_3$	57.7
Bronze- 15v% BaTiO$_3$	51.6
Bronze- 30v% BaTiO$_3$	52.7
Bronze- 45v% BaTiO$_3$	37.5
Nickel- 0v% BaTiO$_3$	82.5
Nickel- 3v% BaTiO$_3$	64.5
Nickel- 12v% BaTiO$_3$	34.7
Ferroelastic damping active region	15-100[3, 42]

These strains also fall well within the linear elastic region of the composites to avoid energy dissipation due to plastic deformation.

3.1 Sintered Bronze-BaTiO$_3$ System

Damping vs. Frequency

Damping ability at room temperature was measured versus frequency from 0.01-20 Hz for three identical bronze-BaTiO$_3$ composite samples at each volume percent. These results are shown in Figure 57.
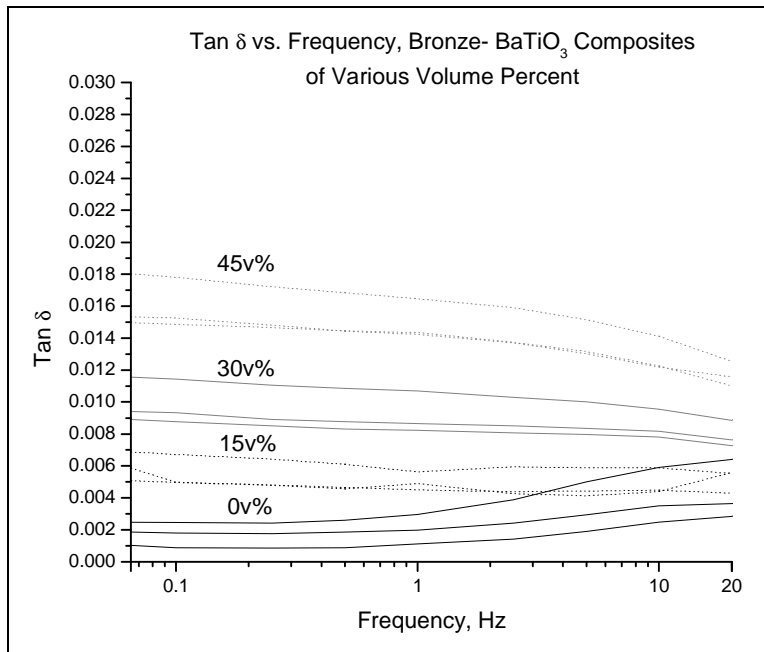
Figure 57. *Tan δ* **vs. frequency of the bronze-BaTiO$_3$ composites of various v%**

As expected, the overall damping seemed to increase with increasing volume percent for pure bronze. In the composite samples there appears to be little dependence in *tan δ* on frequency. Determining a point of stability was the main reasoning for examining damping behavior versus frequency in the composites. Based on this data, 1 Hz was selected as the test frequency for the damping versus temperature experiments performed in this work. In order to fully understand the magnitude of damping provided by ferroelastic twinning, and attempt was made to minimize variation of the other active damping mechanisms. To better understand the repeatability of these measurements, Figure 58 through Figure 61 include the *tan δ* versus frequency data for each bronze-BaTiO$_3$ volume fraction.
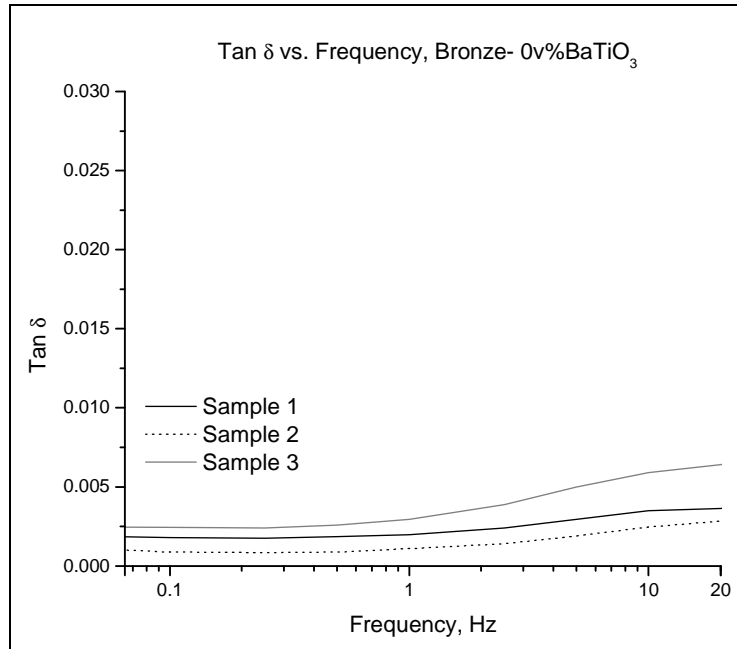
Figure 58. *Tan δ* **vs. frequency for bronze- 0v%BaTiO$_3$**

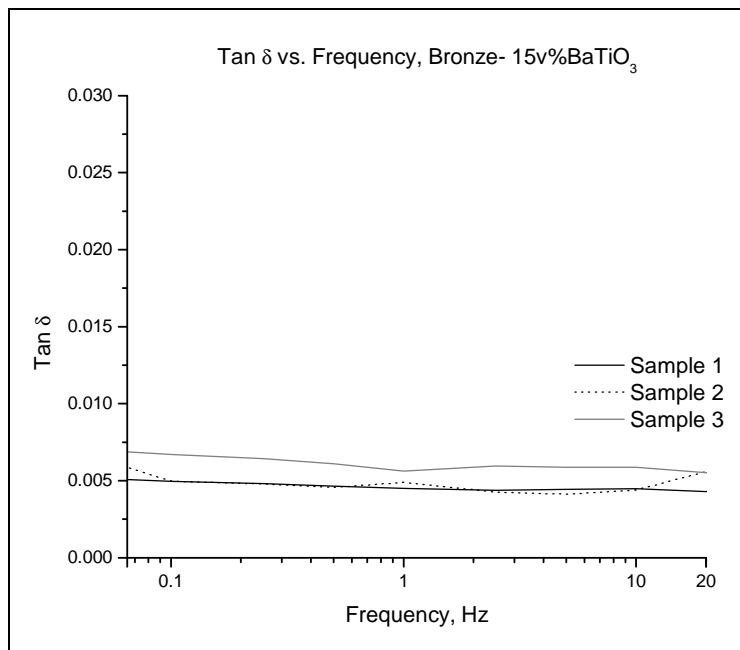**Figure 59.** *Tan δ* **vs. frequency for bronze- 15v%BaTiO$_3$**
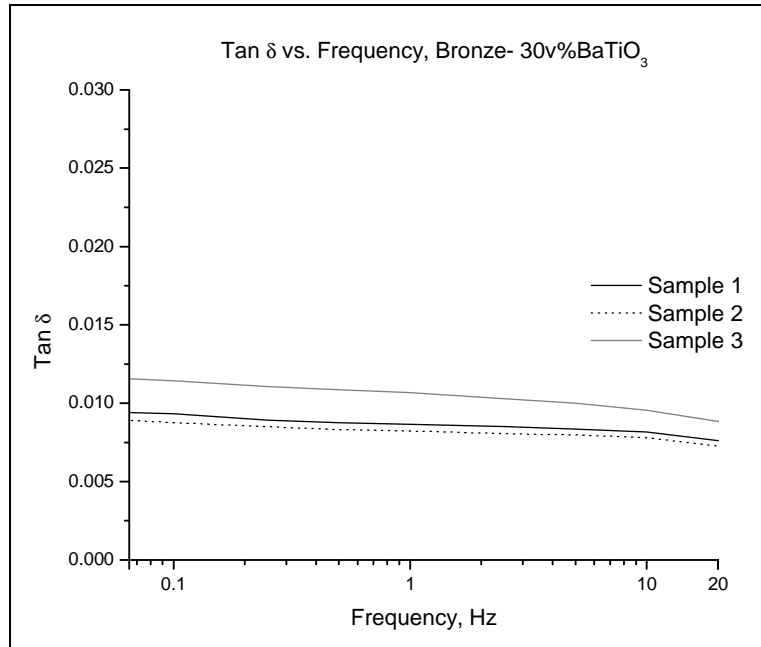
Figure 60. *Tan δ* **vs. frequency for bronze- 30v%BaTiO₃**
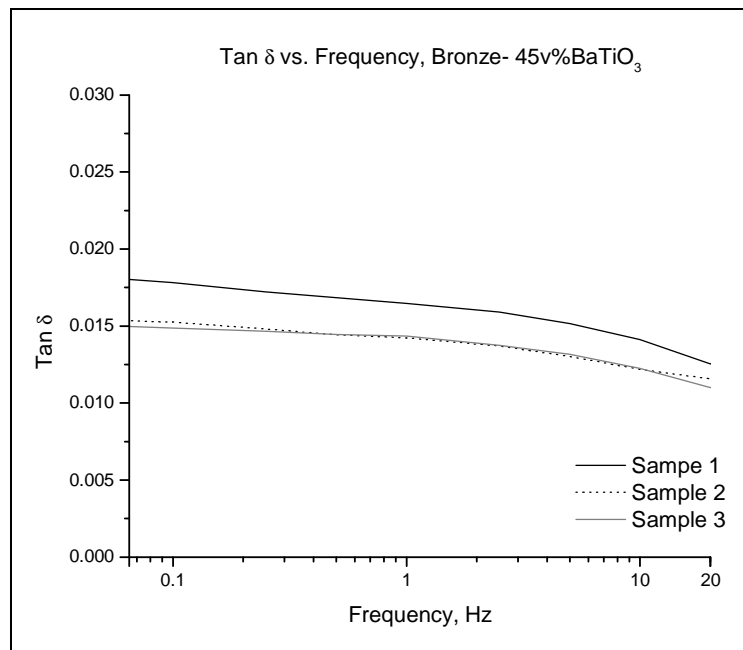

Figure 61. *Tan δ* **vs. frequency for bronze- 45v%BaTiO₃**

Damping vs. Temperature

Figure 33 shows the effect of volume percent reinforcement on the *tan δ* of bronze-

BaTiO₃ FR-MMCs over the temperature range of 25-200$^{\text{o}}$C.

110
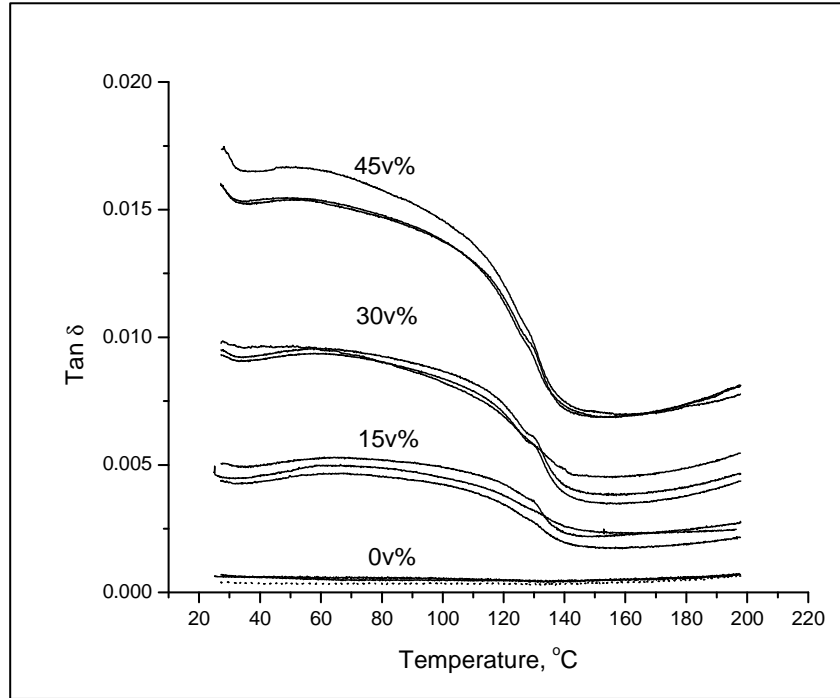
Figure 62. *Tan δ* **vs. temperature of bronze-BaTiO₃ of various v%**

It is apparent here that increasing the volume percent of the reinforcement leads to an increased damping ability in the composite. This follows intuition as the reinforcement is the primary source of energy dissipation in the composite. Increased volume percent reinforcement leads to a greater amount of internal interface in the material. Frictional sliding occurs at these interfaces causing anelastic behavior in the material as stress energy is dissipated.

Not only do metal-ceramic interfaces in the system increase its damping ability, but energy is also dissipated through mechanisms related to the ferroelectric domains in the ceramic reinforcement. As the ceramic is mechanically strained, domain wall motion in the form of ferroelastic twinning is induced.[42] This occurs as the ceramic strives to maintain its current degree of polarization by arranging unit cells in such a way that they are not stressed along the axis of polarization. Above T_C though, this mechanism disappears, allowing for its quantification through comparison of damping values just before and after T_C. These distinct areas of the curve are highlighted in Figure 63 and can be broken into three parts labeled A, B, and C.

111
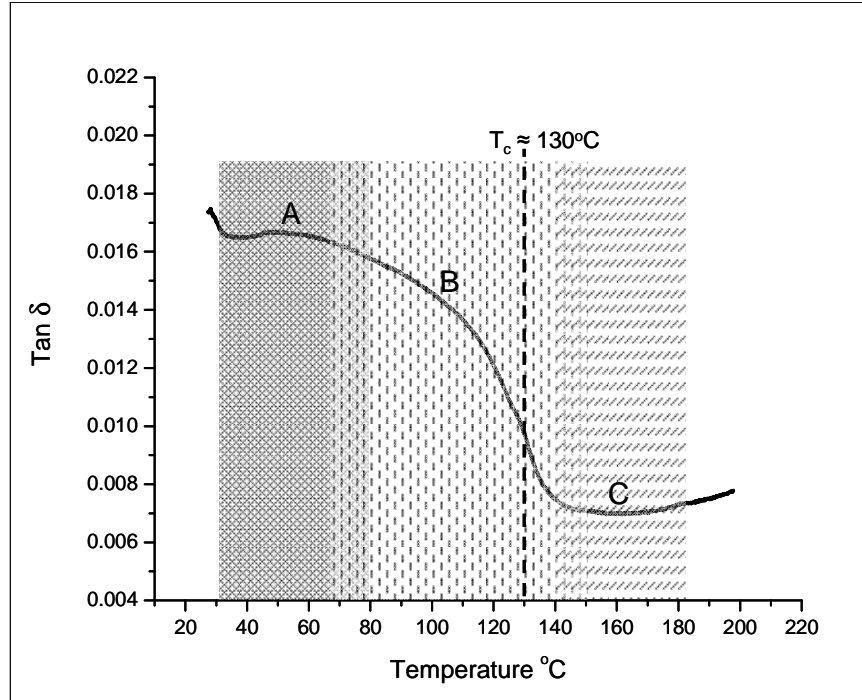
Figure 63. Tan δ vs. temperature curve of a bronze- BaTiO$_3$ FR-MMC

Region A represents the total damping behavior of the composite, in which both traditional and ferroelastic mechanisms are active. Region B represents both a gradual and sharp drop in *tan δ*. The gradual decrease in tan d can be attributed to the steady decrease in the ratio of the "c" axis to the "a" axis of the tetragonal unit cell found in ferroelectric BaTiO$_3$. It is thought that as the c/a ratio is decreased, compression of the elongated "c" axis has a decreased tendency to cause ferroelastic twinning in the domain structure. Thus as the composite is heated, it is thought that this steady decrease in the c/a ratio leads to the gradual decrease in *tan δ* seen in the composite upon heating in region B.   The sharp drop in *tan δ* however, is associated with the ferroelectric to paraelectric phase change at the Curie temperature (T_C). At this point the reinforcement is no longer ferroelectric. Here the lack of a domain structure causes BaTiO$_3$ to lose its ferroelastic damping mechanisms. The fact that this drop exists at T_C represents a proof of concept showing that increased damping associated with the ferroelectric nature of the reinforcement is exhibited by the composite.

Region C represents the region in which only the traditional damping mechanisms are active. The difference in damping behavior between A and C can be used to estimate the

112

magnitude of ferroelastic damping in the composite. It should be noted however that the boundaries between regions A, B, and C are not considered sharp, and an interpretation of their overlap is represented in the texture overlap in the figure. As previously mentioned, below T_C ferroelastic damping mechanisms are active, whereas due to a phase change, above T_C these mechanisms are not.
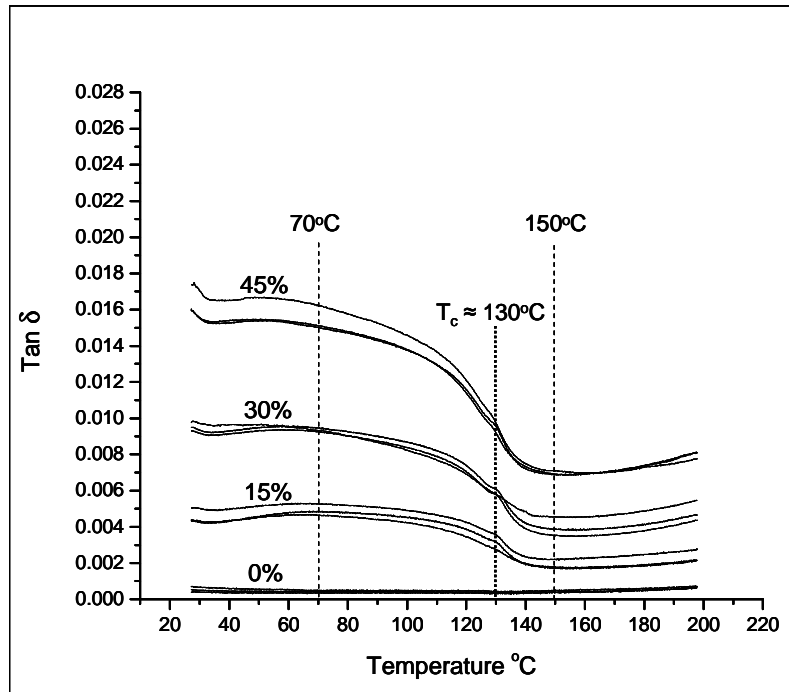
Figure 64. Points of measure to quantify the drop in tan δ at T_C.

As outlined in Figure 64, the damping values at 150°C were subtracted from those at 70°C resulting in an estimate of the overall decrease in *tan δ* due to the ferroelectric, tetragonal to paraelectric, cubic phase change. Figure 65 shows how this drop in *tan δ* appears to increase with increasing reinforcement volume percent, for the bronze-BaTiO$_3$ composite system.

113
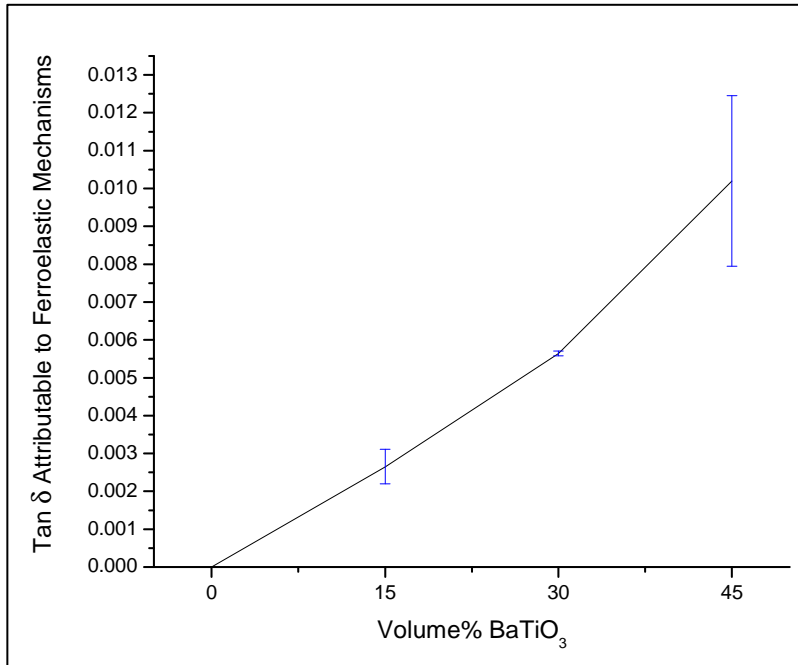
Figure 65. Drop in *tan δ* across T_C with increased v% BaTiO$_3$

Over the range of v% BaTiO$_3$ studied, the drop in *tan δ* appears to follow a linear relationship with increased v%. When bulk BaTiO$_3$ is included, Figure 66, the trend appears to stray from linearity at higher volume percents.
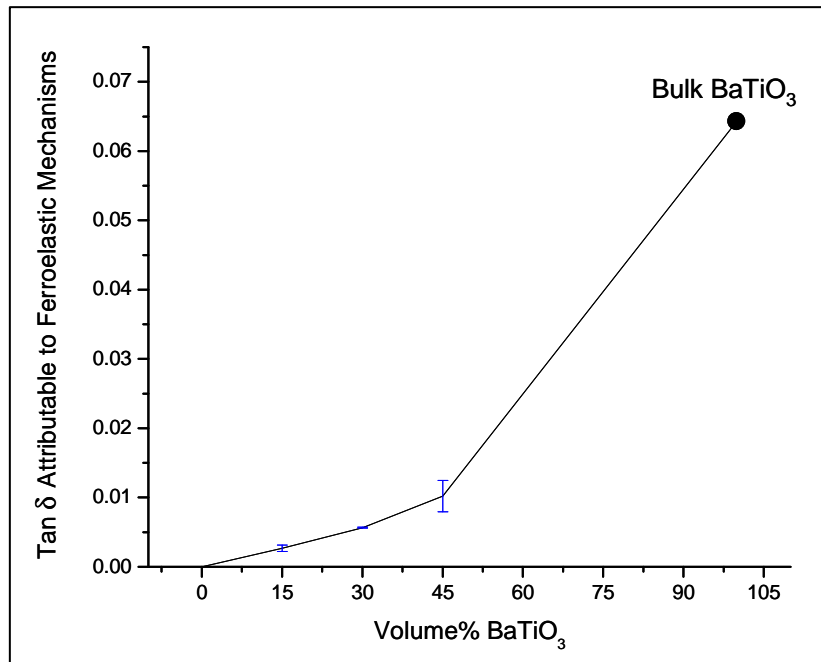
Figure 66. Drop in *tan δ* across T_C with increased v% BaTiO$_3$, including bulk BaTiO$_3$

The data from the composites in Figure 65 indicate that the $BaTiO_3$ is contributing less to the overall damping capability than would be predicted from a simple rule-of-mixtures analysis. In fact, this trend would most likely be a linear relationship, if the composite was fully dense with ideal M/R interfaces. Porosity in the matrix and the geometry of the reinforcement, decrease stress transfer to the reinforcement, so the full damping capacity of the $BaTiO_3$ is never reached. This accounts for the lower than predicted damping capacity in the composites, which also leads to a decrease in the drop in *tan δ* across T_C.

Figure 67 gives an example of how composite damping behavior can be predicted based on the damping curves for bulk $BaTiO_3$ and bulk bronze.
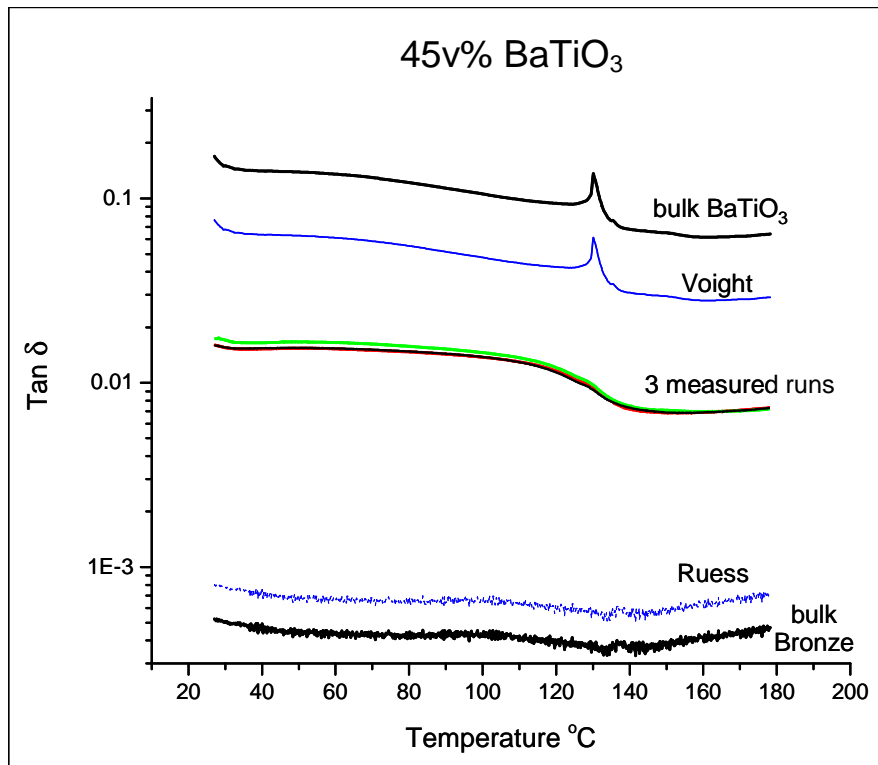
Figure 67. Measured vs. predicted *tan δ* curves for bronze- 45v% BaTiO₃

This theoretical curve was obtained by taking the measured *tan δ* values for both bulk bronze and bulk $BaTiO_3$ and combining them using the rule of mixtures based on a composite of bronze- 45v% $BaTiO_3$ having a flaw-free matrix and strong M/R interfaces. This was accomplished using an upper Voight bounds:

$$\tan \delta_{Composite} = \tan \delta_{Bronze} V_{Bronze} + \tan \delta_{BaTiO_3} V_{BaTiO_3}$$

Eq 37

which assumes no interdependence of the damping mechanisms, and a lower Ruess bounds assuming strong interdependence of the damping mechanisms.

$$\frac{1}{\tan \delta_{Composite}} = \frac{V_{Bronze}}{\tan \delta_{Bronze}} + \frac{V_{BaTiO_3}}{\tan \delta_{BaTiO_3}}$$

Eq 38

The three measured runs seem to fall within the Voight and Ruess bounds, however there may still be some room for improvement, due to porosity in the matrix, poor M/R interfaces, and flaws in the reinforcement particles themselves.

Damping vs. Strain Cycles

Reversible twinning of ferroelastic domains have been identified as the primary source of damping behavior at temperatures below T_C. These twins, however, can be made irreversible after becoming pinned against one another, by oxygen vacancies, by domain walls or by grain boundaries.[1] In an effort to understand reversible versus irreversible ferroelastic twinning in the bronze-BaTiO$_3$ system, *tan δ* has been measured from 0-30,000 strain cycles. These results are shown for various volume fractions in Figure 68.
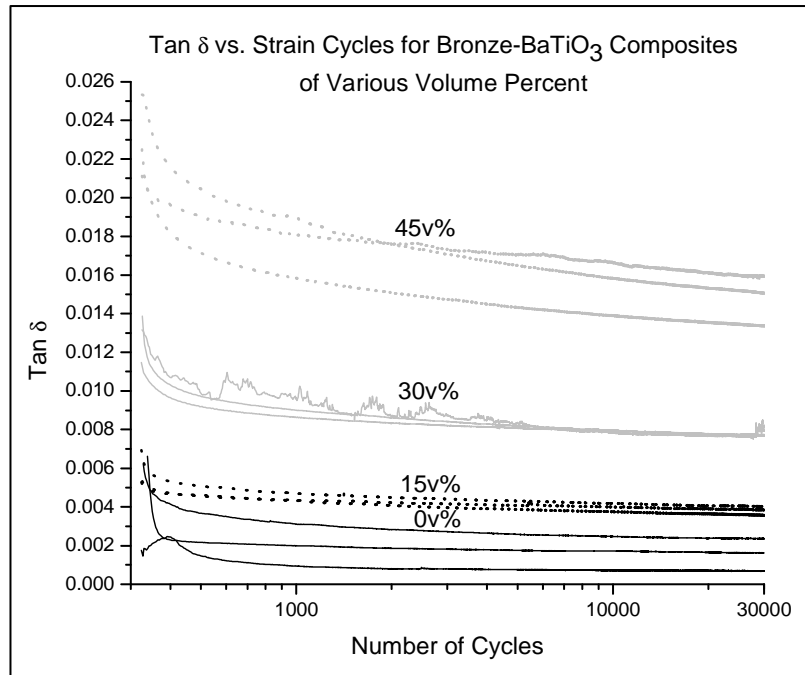
Figure 68. *Tan δ* vs. strain cycles of the bronze-BaTiO₃ composites of various v%

Within the first 400 cycles there appears to be a sharp decrease in damping behavior. This is attributable to the activation of an irreversible damping mechanism. The fact that this trend is also seen in the pure bronze points to the mechanism being inherent to the matrix and not to irreversible domain motion in the reinforcement. This is followed by a gradual decrease in *tan δ*, as the applied directional stress further induces texture in the material as some of the previously reversible twins become pinned. It would be expected that under constant loading conditions, damping in the composite would eventually decay to zero due to complete texturing of the domain structure due to the creation and pinning of ferroelastic twins. In "real world" service however, any variation in the loading conditions should serve to minimize this decay in damping behavior by serving to free a portion of the twin structures that were previously pinned. Figure 69, Figure 70, Figure 71, and Figure 72 contain the *tan δ* versus strain cycle date for each individual bronze-BaTiO₃ volume fraction.
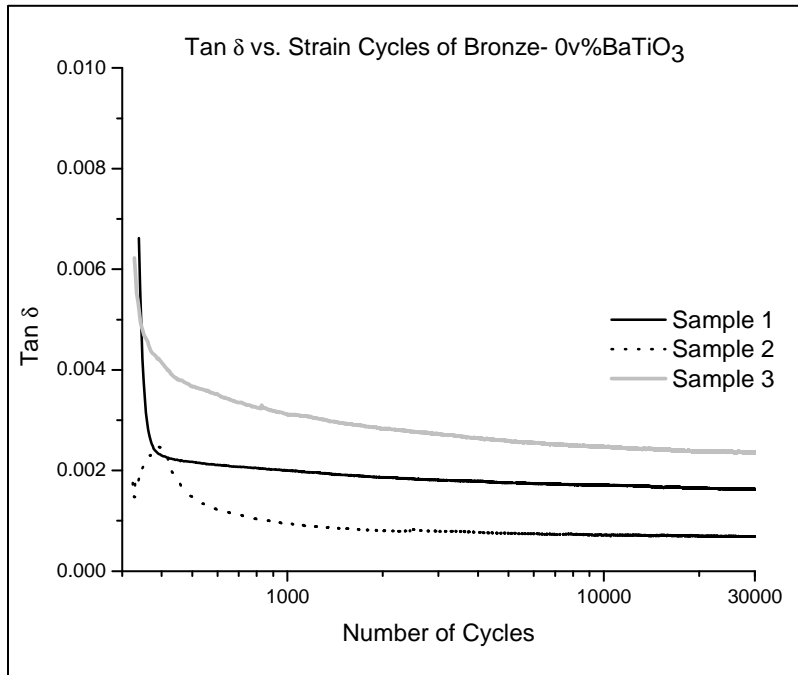
Figure 69. *Tan δ* **vs. strain cycles for bronze- 0v%BaTiO₃**
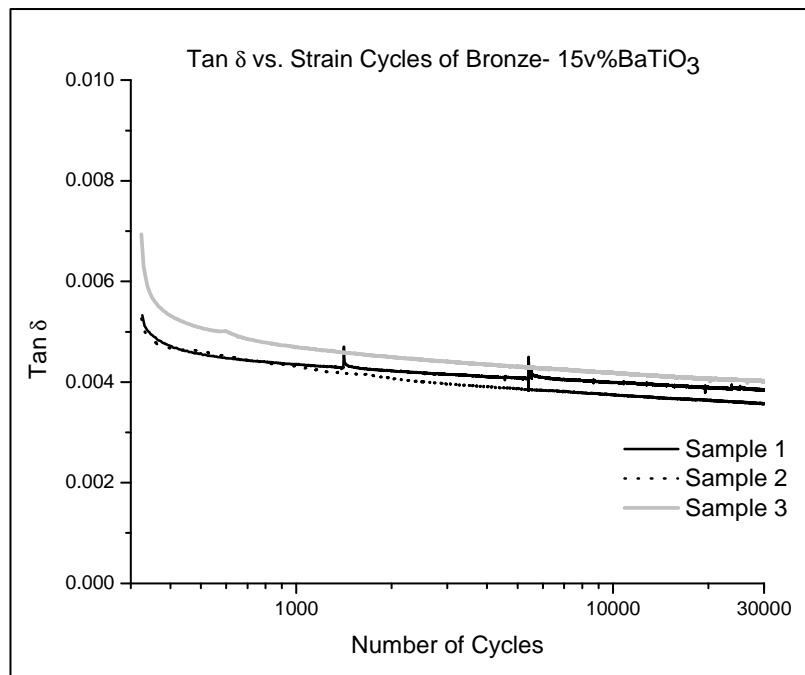
Figure 70. *Tan δ* **vs. strain cycles for bronze- 15v%BaTiO₃**

118
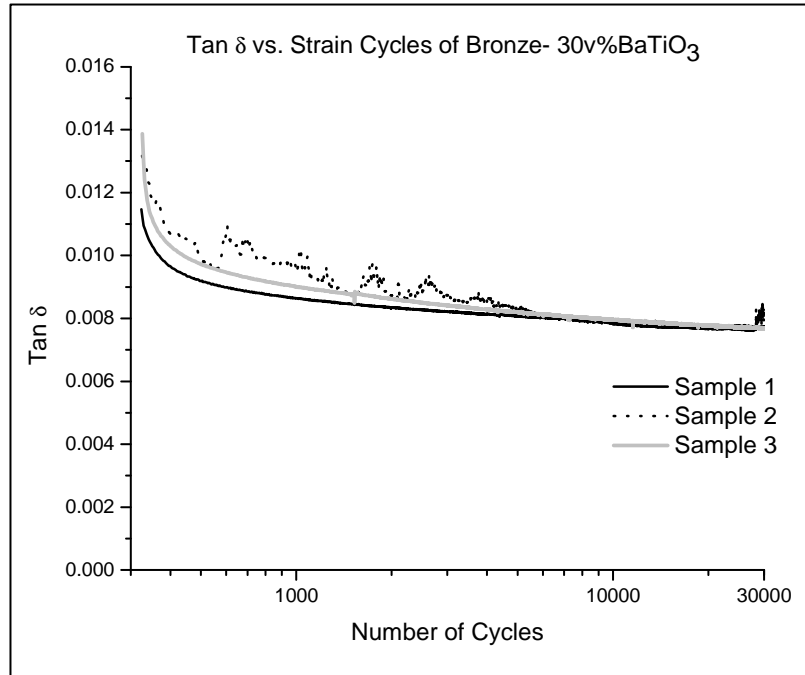
Figure 71. *Tan δ* **vs. strain cycles for bronze- 30v%BaTiO₃**
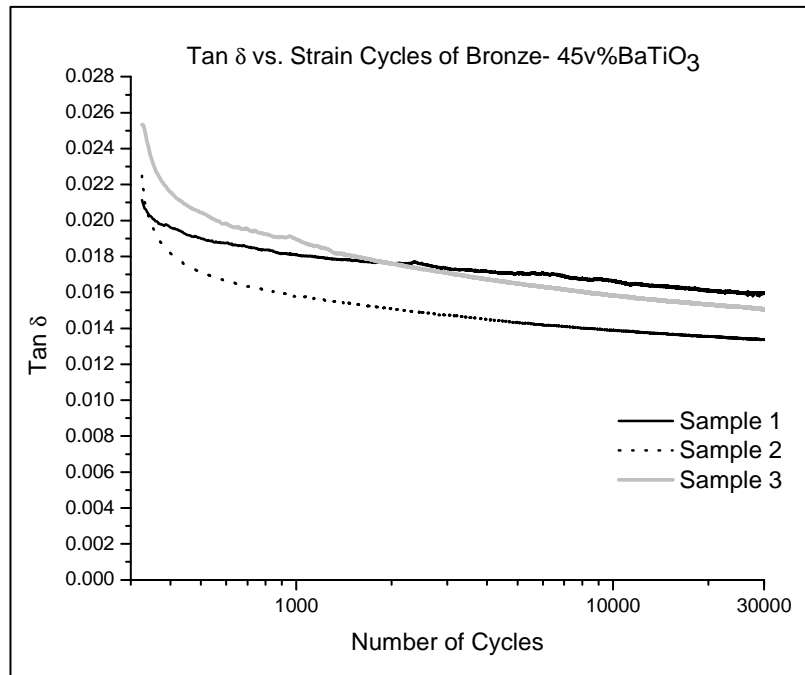
Figure 72. *Tan δ* **vs. strain cycles for bronze- 45v%BaTiO₃**

3.2 Electroformed Nickel-BaTiO$_3$ System

Damping vs. Frequency

Damping ability at room temperature was also measured versus frequency for the Ni-BaTiO$_3$ system. This was done from 0.01-50 Hz for three nickel-BaTiO$_3$ composites at each fabricated volume percent. These results are shown in Figure 73.
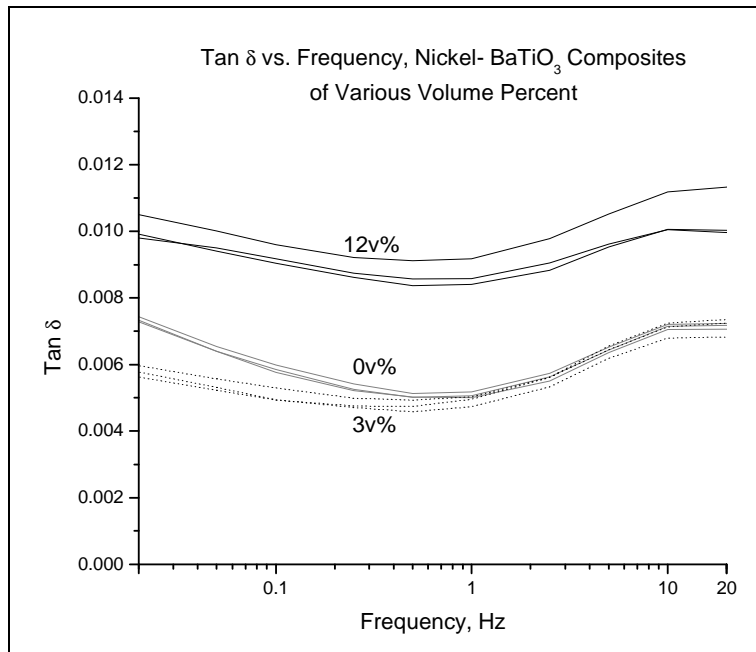
Figure 73. *Tan δ* vs. frequency of the nickel-BaTiO$_3$ composites of various v%

As with the bronze matrix system, the overall composite damping seemed to increase with increasing volume percent BaTiO$_3$. This behavior showed little dependence on frequency. Based on the data, 1 Hz was also selected as the test frequency for the damping versus temperature experiments performed on the Ni matrix system. To better understand the repeatability of these measurements, Figure 74 through Figure 76 include the *tan δ* versus frequency data for the nickel-BaTiO$_3$ composites at each volume fraction.
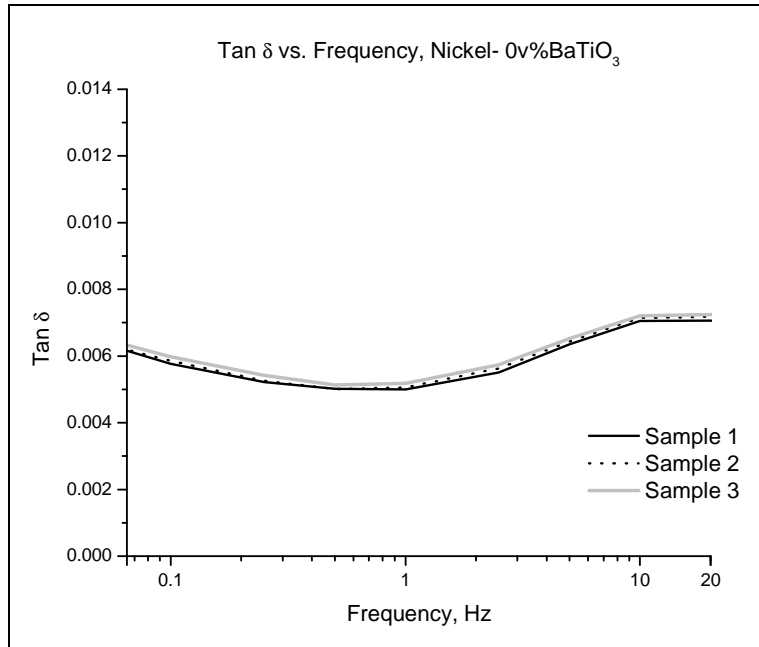
Figure 74. *Tan δ* **vs. frequency for nickel- 0v%BaTiO₃**
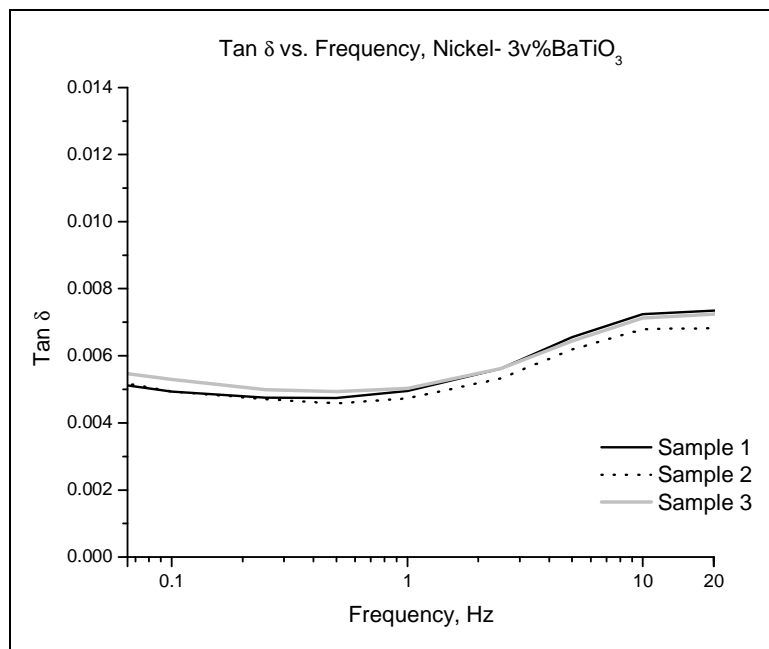
Figure 75. *Tan δ* **vs. frequency for nickel- 3v%BaTiO₃**
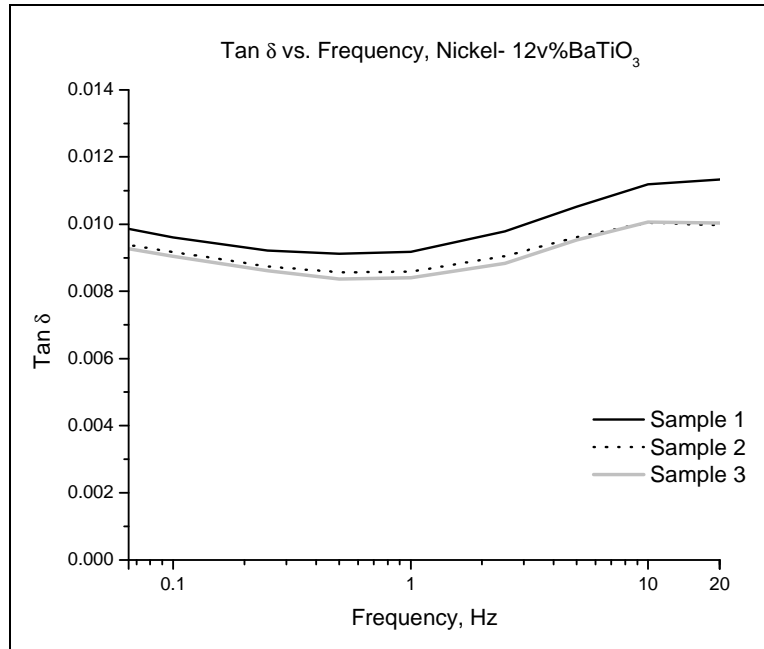
Figure 76. *Tan δ* **vs. frequency for nickel- 12v%BaTiO₃**

Damping vs. Temperature

Figure 77 shows the effect of volume percent reinforcement on the *tan δ* of nickel-
BaTiO$_3$ FR-MMCs over the temperature range of 25-200°C.
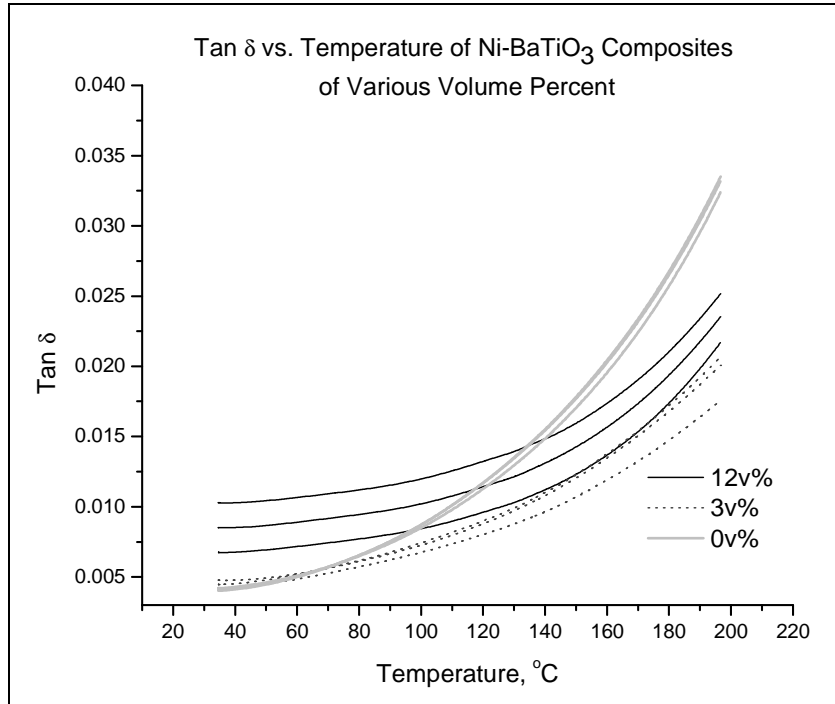
Figure 77. *Tan δ* vs. temperature of nickel-BaTiO$_3$ of various v%

As seen in the frequency experiments, it is apparent here that increasing the volume
percent of the reinforcement leads to an increased damping ability in the electroformed
composite. Increased volume percent reinforcement leads to a greater amount of internal
interface in the material. Frictional sliding occurs at these interfaces causing anelastic
behavior in the material as stress energy is dissipated causing *tan δ* to increase with
increasing volume percent reinforcement. In addition, energy should also be dissipated
through mechanisms related to the ferroelectric domains in the ceramic reinforcement.

Unlike the bronze-BaTiO$_3$ system, however, the electroformed Ni system seems to
exhibit no obvious drop in *tan δ* at T_C.
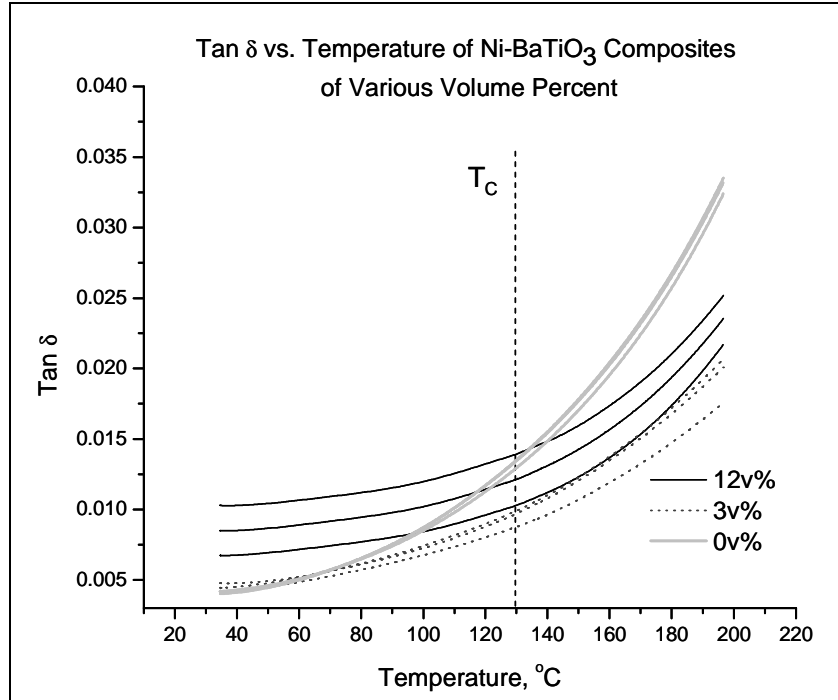
Figure 78. *Tan δ* **vs. temperature of nickel-BaTiO$_3$ of various v% with the T_C labeled**

There does seem to be a change in slope of the 12v% composite damping curves near T_C, above which the curve begins to more closely match that of pure electroformed Ni.
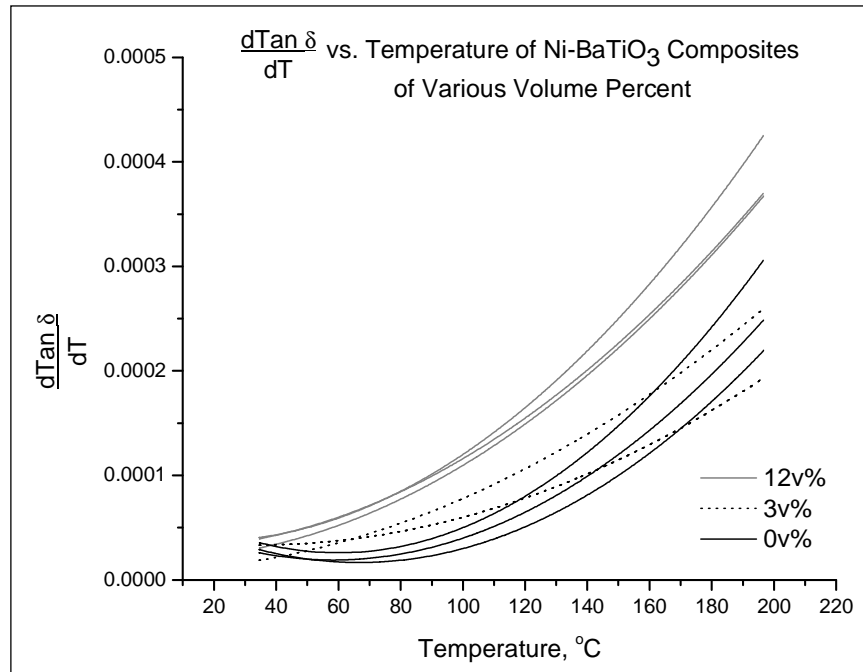
Figure 79. Change in slope of composite curves near T_C

According to Figure 79, the slope appears to increase rapidly, especially above T_C. This is attributed to the transition from ferroelastic twinning in the reinforcement to the inherent mechanisms in the Ni matrix as the primary damping mechanism in the composite.

In BaTiO$_3$, the c/a ratio steadily decreases upon heating.[22] As in the bronze system, this is thought to decrease the amount of damping contributed to the system by ferroelastic twinning. Simultaneously as shown in Figure 78, the inherent damping of the Ni matrix increases with increasing temperature.   Above T_C, the highly temperature dependent, ferromagnetic damping behavior of Ni appears to dominate. Below T_C, it seems that the damping behavior is influenced by the reinforcement. Here the damping in the composites is less temperature dependent, consistent with that of pure BaTiO$_3$ at temperatures below the vicinity of T_C.   The added damping from all composite mechanisms seemed to be sufficient to affect damping behavior however, at T_C one cannot resolve the *tan δ* due to ferroelastic damping due to the high inherent contribution to *tan δ* of Ni at elevated temperatures.

Porosity in the matrix and the geometry of the reinforcement, decrease stress transfer to the reinforcement, so the full damping capacity of the BaTiO$_3$ is never reached and it cannot realize its full contribution to the damping behavior of the composite system. This accounts for the lower than predicted damping capacity in the composites, which also leads to a decrease in the drop in *tan δ* across T_C. Here the drop is so small that it does not visibly affect the shape of the damping curve.

Figure 80 gives an example of how composite damping behavior can be predicted based on the damping curves for bulk BaTiO$_3$ and bulk nickel. This theoretical curve was obtained by taking the measured *tan δ* values for both bulk bronze and bulk BaTiO$_3$ and combining them using the rule of mixtures based on a composite of nickel- 12v% BaTiO$_3$ having a flaw-free matrix and strong M/R interfaces. This was accomplished using an upper Voight bounds, Eq 37, which assumes no interdependence of the damping mechanisms, and a lower Ruess bounds, Eq 38, assuming strong interdependence of the damping mechanisms.
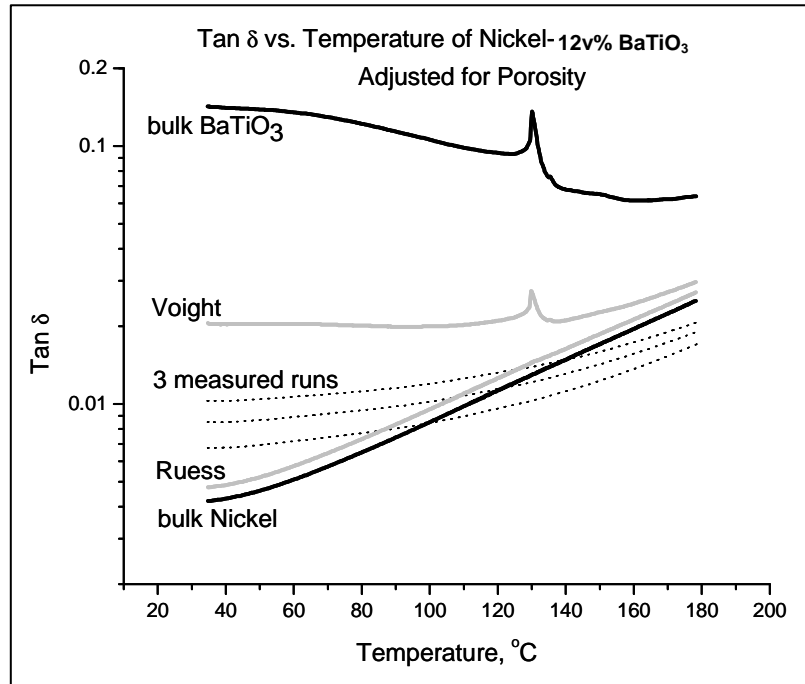
Figure 80. Measured vs. predicted *tan δ* curves for nickel-12v% BaTiO₃

The three measured runs seem to fall within the Voight and Ruess bounds, only at low temperatures. At increased temperature, the ferromagnetic damping in Ni is the dominant mechanism. The composites contain 15.20% porosity and thus 15.20% less Ni volume to contribute to damping behavior. Figure 81 shows the results of adjusting for this lack of material by simply subtracting 15.20% from the damping values of the pure nickel sample.
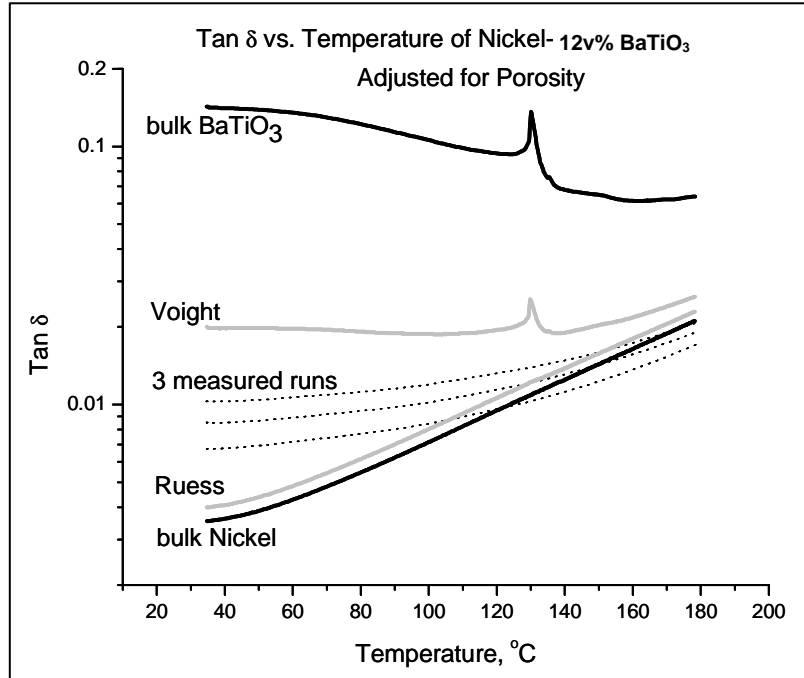
Figure 81. Measured vs. predicted *tan δ* curves for nickel-12v% BaTiO₃, adjusted to account for

Although this adjustment seems to help, the three measured runs still do not fall completely within the Voight and Ruess bounds. This is most likely due to 15.20% being an underestimate of the open porosity found in the Ni- 12v%BaTiO₃ composites as it was measured at only a single cross-section.

Damping vs. Strain Cycles

It was previously mentioned that the twinning of ferroelastic domains can be made irreversible after becoming pinned against one another, by oxygen vacancies, by domain walls or by grain boundaries.[1] As for the bronze matrix composites, *tan δ* has been measured from 0-30,000 strain cycles in an effort to understand reversible versus irreversible ferroelastic twinning in the Ni-BaTiO₃ system. These results are shown for various volume fractions in Figure 82.
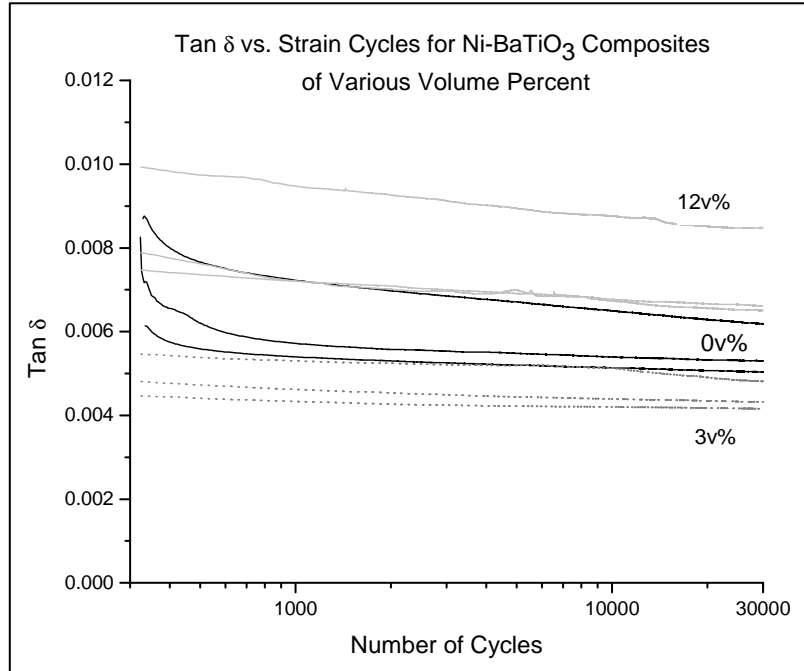
Figure 82. *Tan δ* **vs. strain cycles of the nickel-BaTiO$_3$ composites of various v%**

As with the bronze system, within the first 400 cycles there appears to be a sharp decrease in damping behavior for the pure Ni. Here, this is attributable to the activation of an irreversible damping mechanism in the Ni. In both the pure Ni and the composites, a gradual decrease in *tan δ* is seen with increasing strain cycles. As with the bronze system, this is evidence some portion of the damping mechanism becoming irreversible. This is attributable to a slow decrease in total twinning activity due to the pinning of reversible ferroelastic twins.   Figure 83, Figure 84, and Figure 85 contain the *tan δ* versus strain cycle date for each individual Ni-BaTiO$_3$ volume fraction.
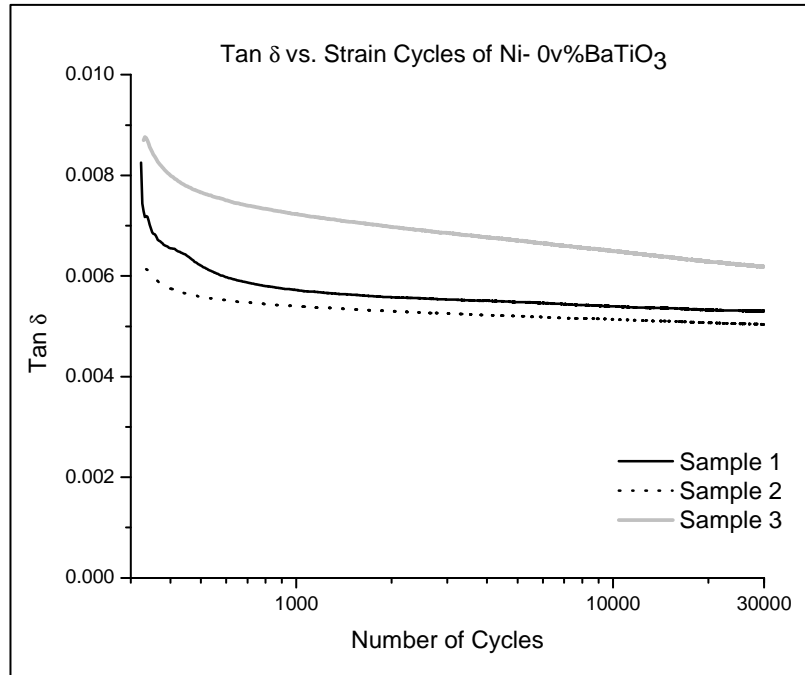
Figure 83. *Tan δ* **vs. strain cycles for nickel- 0v%BaTiO₃**
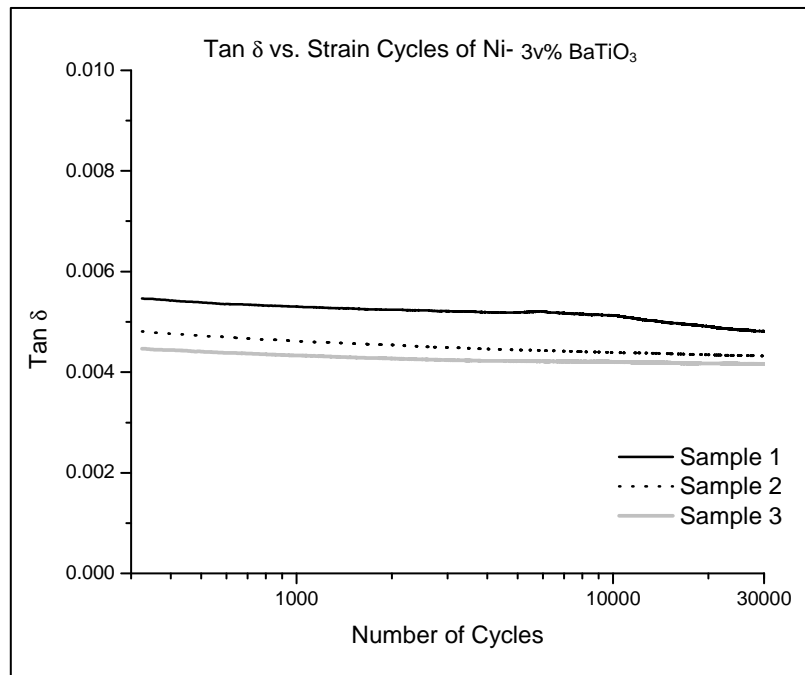
Figure 84. *Tan δ* **vs. strain cycles for nickel- 3v%BaTiO₃**
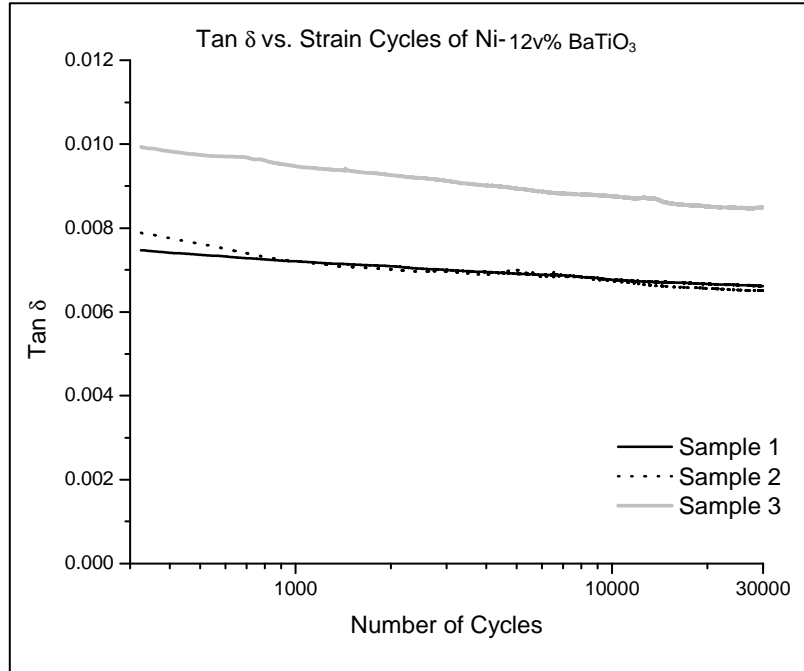
Figure 85. *Tan δ* **vs. strain cycles for nickel- 12v%BaTiO₃**

4. Strength Behavior of the Composites

In traditional composite systems, reinforcement is generally added to a matrix to provide added strength. In this work the primary goal of the ferroelectric/ferroelastic ceramic particle additions was to provide added damping to the system. The following section provides information on how this reinforcement affected strength in the different composite systems.

4.1 Sintered Bronze-BaTiO$_3$ System

Porosity degrades the mechanical properties of PM materials. As an example, strength generally decreases with increasing porosity since pores reduce the load bearing cross-sectional area, and concentrate stress. Secondary pressing and sintering can serve to mechanically and thermally close pores, while reinforcement plating has been shown to decrease pore formation around the embedded particles and allow them to diffusion bond with the matrix.[5] In composite systems, strength is strongly related to the M/R interface. In composites with strong interfaces, stress can be transferred from the matrix to the reinforcement allowing for combined load bearing, while at the same time dispersion mechanisms can add to the strengthening of the matrix. As interfacial integrity decreases, M/R interaction decreases, and the role of the reinforcement approaches that of traditional porosity.

Based on the negative effects of volume percent reinforcement on composite structure, one would predict that increases in ceramic volume percent would lead to decreased mechanical properties of the composite. Based on the results of the engineering stress/strain (s/s) analysis in three-point bending found in Figure 86, this assumption appears to be correct.
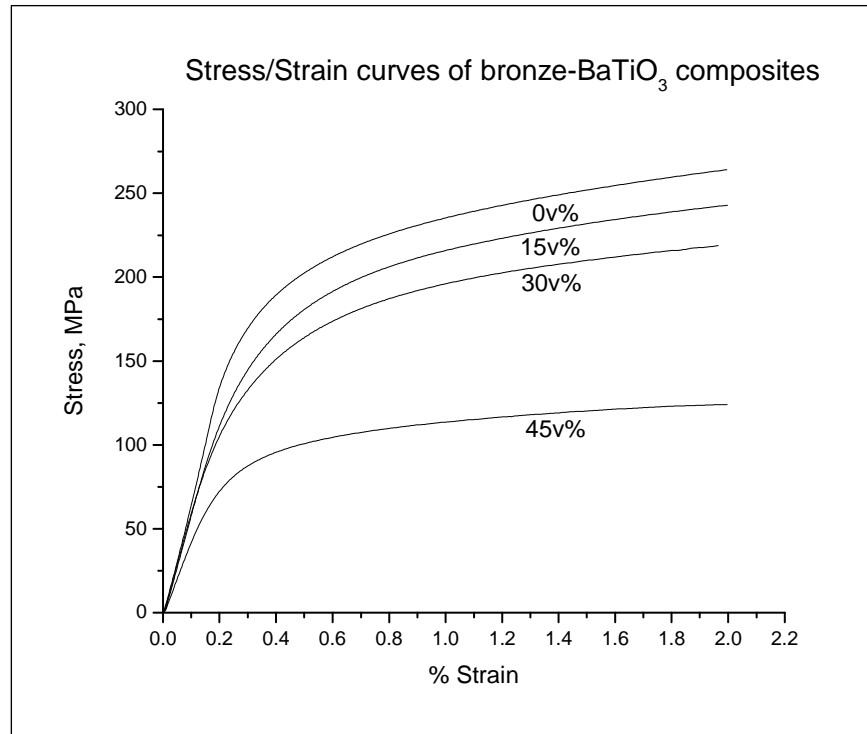
Figure 86. Stress/Strain curves of bronze-BaTiO$_3$ composites of various volume percents

This is further emphasized by the modulus data seen in Figure 87.
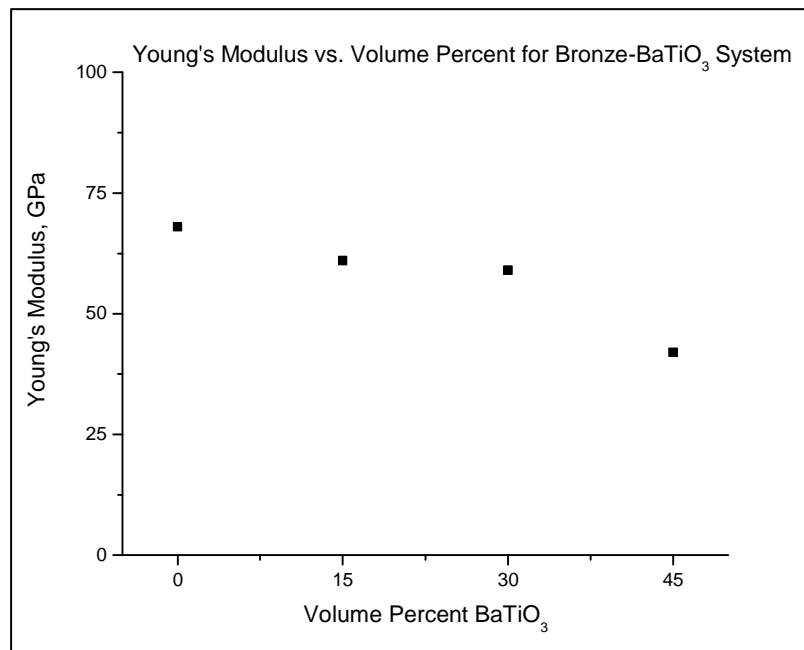
Figure 87. Young's modulus vs. volume fraction plated BaTiO$_3$

A steady decease in modulus is seen with increasing volume percent reinforcement. This follows the steady increase in porosity seen with increasing reinforcement seen in the previous section. This porosity decreases the load bearing cross-section of the sample, decreasing its measured modulus. This decrease in mechanical properties becomes further apparent in the plot of average yield strength versus volume fraction shown in Figure 88.
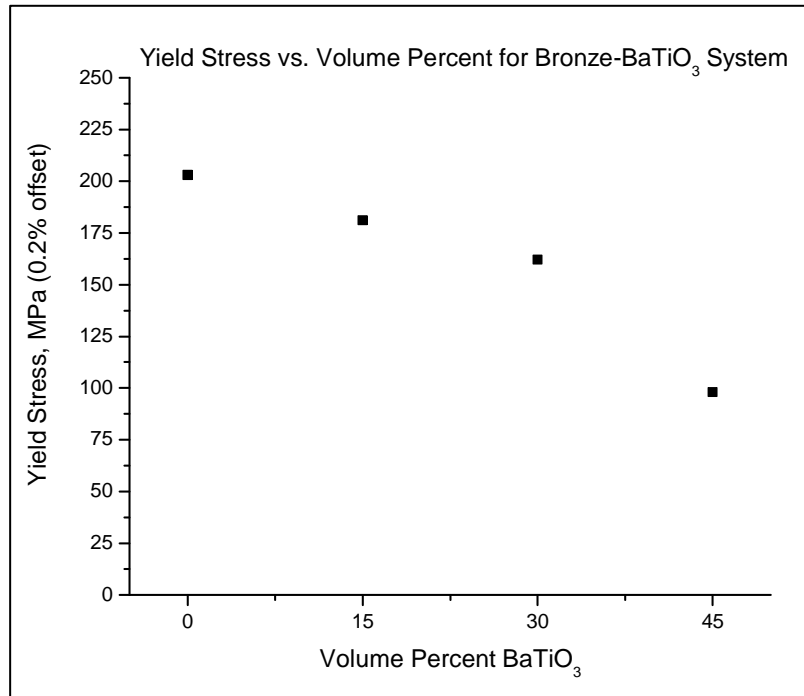
Figure 88. Composite yield strength vs. volume fraction plated BaTiO₃

It seems further improvements in consolidation are necessary before the benefits from composite strengthening, as modeled in chapter 2, can overcome strength decreases due to porosity. Decreased overall porosity should serve to strengthen both the metal matrix and the M/R interfaces. Without a strong interface, the reinforcement can act as added porosity. This combined with porosity in the matrix decreases the effective load bearing surface area of the composite, while adding sites of stress concentration in the matrix, leading to the overall decrease in composite mechanical properties shown in this work.

4.2 Electroformed Nickel-BaTiO$_3$ System

In most materials, porosity tends to have a negative effect on mechanical properties. As previously mentioned, this can be magnified in composite systems if the porosity affects the M/R interface. The unique properties of composite systems are based on the interaction between the matrix and reinforcement, and for them to fully interact there needs to exist a strong interface. As seen in section 2, the M/R interface of the electroformed Ni-BaTiO$_3$ composites appeared to be sound and in general lacked the presence of heavy porosity. The matrix itself however, exhibited a steep increase in porosity with increasing volume percent reinforcement, which had a marked effect on the mechanical properties of the system.

In the electroformed composites, increased volume fraction reinforcement led to increased porosity in the matrix due to high surface roughness causing dendrite formation. The increased porosity caused a significant decrease in mechanical properties in the composite, as shown in Figure 89.
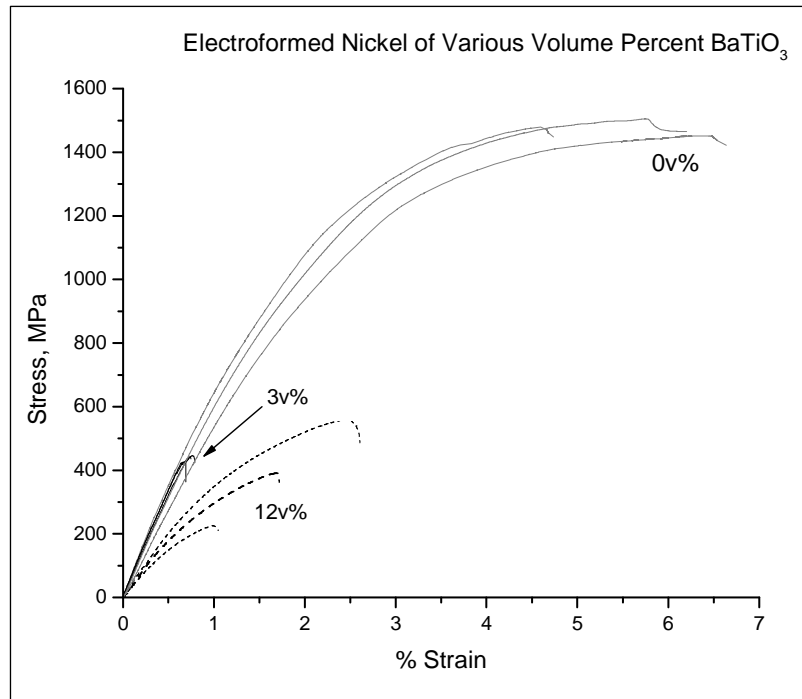
Figure 89. Stress/Strain curves of electroformed nickel- BaTiO$_3$ composites of various v%

However, the 0v% electroformed Ni appears to out perform commercially pure Ni 200 whose yield is 148 MPa.[27] This is common with electroformed materials and is attributed to a fine grain structure and the Hall-Petch effect.[62] The Hall-Petch relationship predicts that for Ni an increase in yield strength from 148 to ~800 MPa in Ni would require a ~60 nm grain size.[69] This increased strength quickly diminishes as reinforcement is added due to induced porosity as shown in section 2 of this chapter.
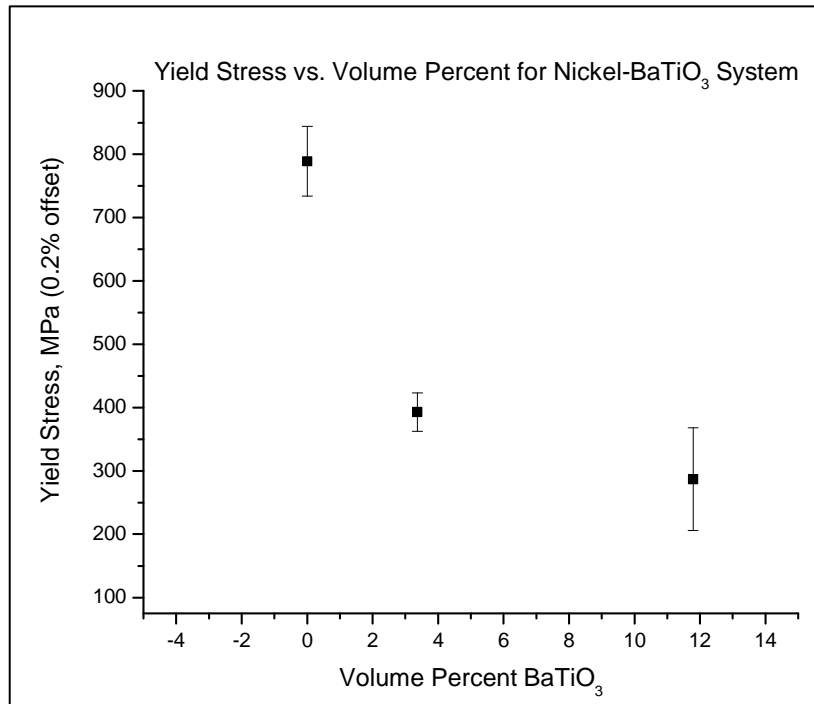
Figure 90. Yield stress versus volume percent for Ni-BaTiO₃ composites

This is further emphasized by the modulus data seen in Figure 91.
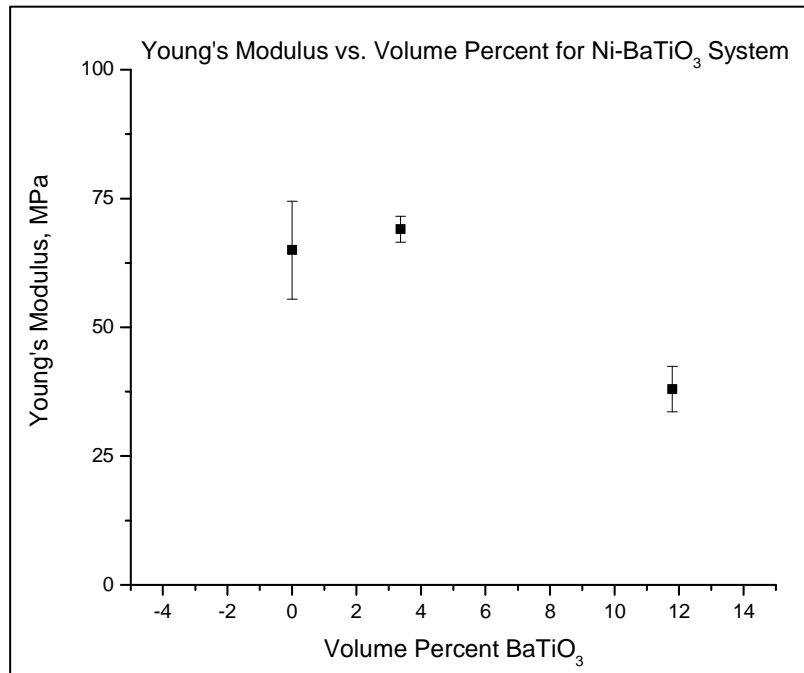
Figure 91. Young's modulus versus volume percent for Ni-BaTiO$_3$ composites

Three samples of each volume fraction were tested and the stress/strain curves for these are shown individually in Figure 92, Figure 93, and Figure 94.
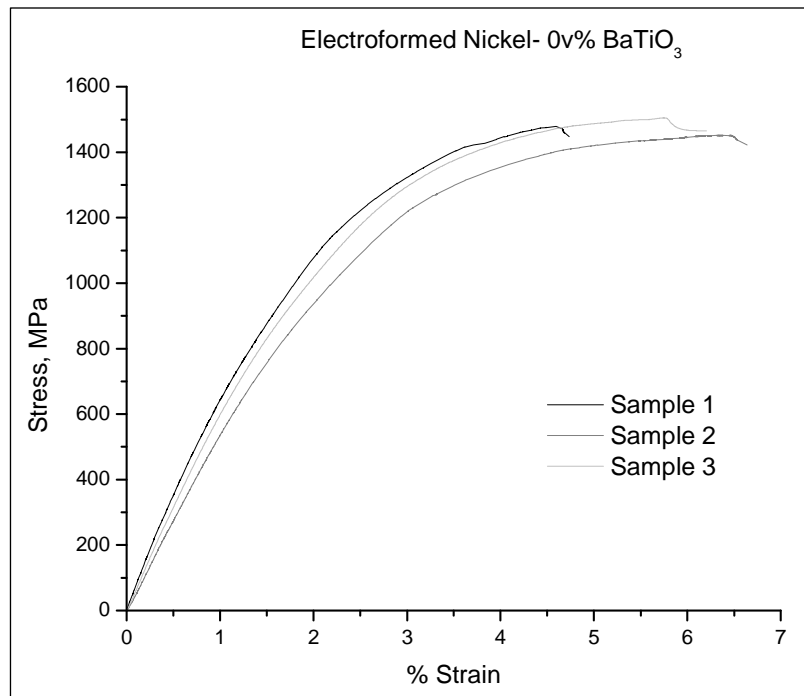
Figure 92. Stress/Strain curves of electroformed- 0v%BaTiO$_3$ composites
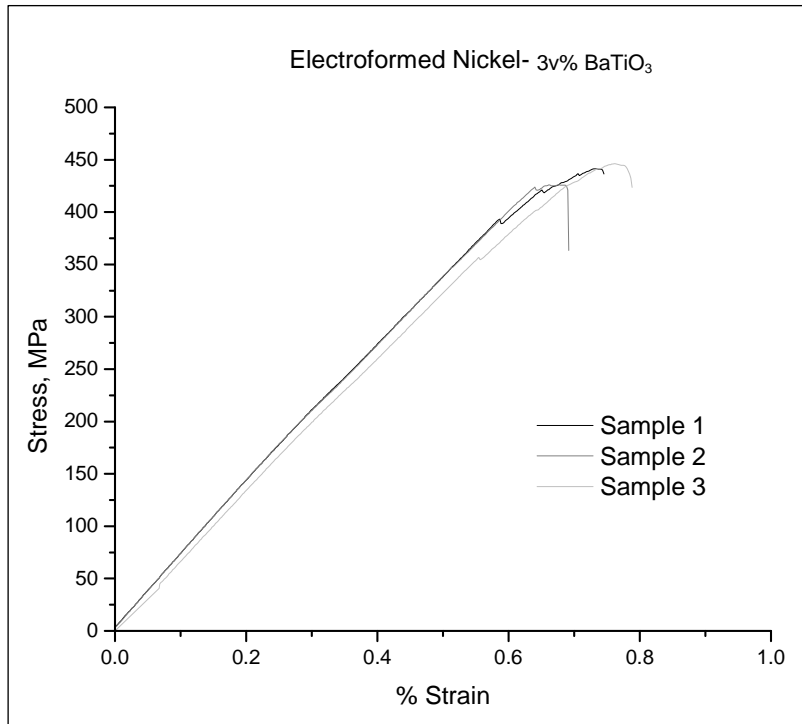
Figure 93. Stress/Strain curves of electroformed- 3v%BaTiO$_3$ composites
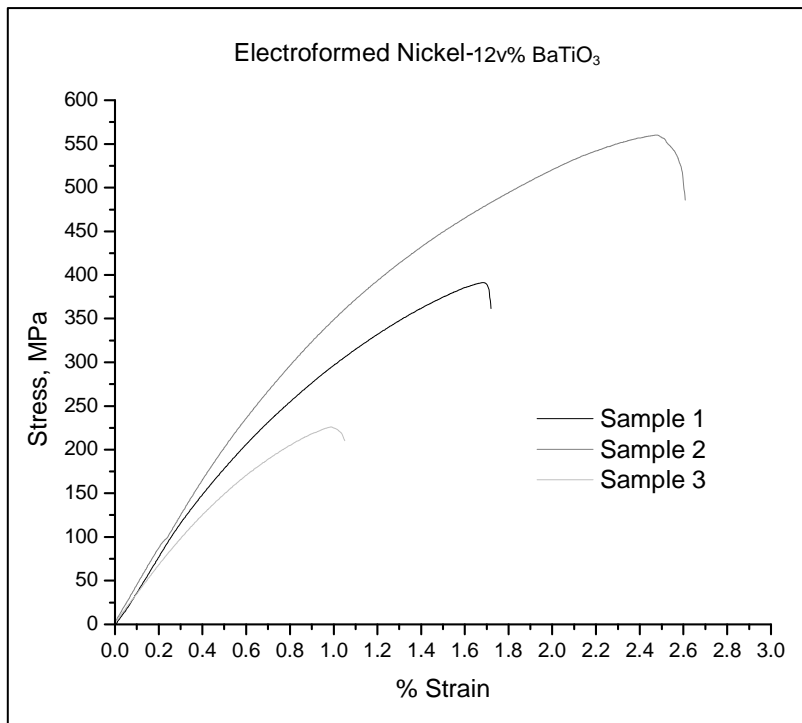
Figure 94. Stress/Strain curves of electroformed- 12v%BaTiO$_3$ composites

5. Reinforcement Particle Quality

The departure from predicted damping and mechanical behavior cannot be attributed solely to the poor quality (porosity) of the matrix. The embedded $BaTiO_3$ particles were produced through mechanical grinding of monolithic sintered pieces. As a result, this grinding, left many residual cracks throughout the individual particles, which can be seen in Figure 39.
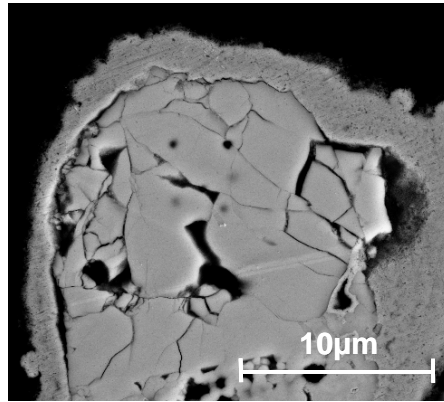
Figure 95. Cracks in individual reinforcement particles left by grinding for size refinement

Due to these cracks, the reinforcement phase can no longer be though of as individual particles but as tight agglomerations of smaller ones. This decrease in effective particle size has most likely lead to a drastic decrease in the overall ferroelastic damping capability of the reinforcement. First, a portion of the stress that would normally activate twinning in the $BaTiO_3$ can be dissipated through frictional sliding in the cracks. Secondly, the ferroelastic damping ability in the reinforcement is very sensitive to domain structure and grain size. The decrease in effective particle size due to cracking, also leads to decreased grain size as grains are fractured. As particle size drops below 1μm, this becomes increasingly important due to the limiting effects of grain boundaries on the mobility of domain walls and the twinning responsible for ferroelastic damping.[1]

Porosity also seemed to be significant in the $BaTiO_3$ reinforcement particles, an example of this can be seen in Figure 40.
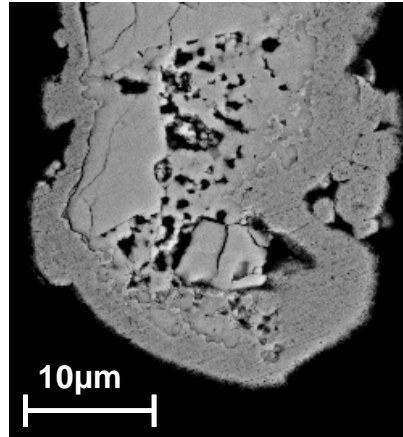
Figure 96. Porosity in the reinforcement material

Porosity can cause a significant decrease the mechanical properties in the reinforcement,[63] while at the same time promote further cracking stemming from stress concentration in the pores. These pores, like grain boundaries, can also limit domain wall motion and thus the ferroelastic damping ability of the embedded particles. Improvements in the reinforcement would increase the damping ability of the bulk reinforcement. This, in turn, should upwardly shift the theoretical composite damping curve at all volume percents.

6. Neutron Diffraction

As part of a larger unpublished study by Schultz et. al.,[44] including the author of this work, neutron diffraction was used to verify ferroelastic domain motion as an active damping mechanism in FR-MMCs.[44, 66] These tests were performed on the Spectrometer for Materials Research at Temperature and Stress (SMARTS) at the Los Alamos Neutron Science Center (LANSCE).

Due to its tetragonal structure, $BaTiO_3$, exhibits a doublet peak at a d-spacing near four angstroms in both x-ray and neutron diffraction. This doublet is a result of an overlap between the peak of the a-axis (3.992 Å at 25^oC)[22] and that of the c-axis (4.036 Å at 25^oC)[22]. The ratio of the c- to a-axis is generally used to define the degree of tetragonality of ferroelectric materials. When stress is applied to a tetragonal material such as $BaTiO_3$, those c-axes parallel to the applied stress are compressed. With sufficient grain size, this stress is generally alleviated through the formation of a twin. This effectively changes the orientation of the tetragonal structure by 90° placing the c-axis perpendicular to the applied load stabilizing the structure. Under x-ray or neutron diffraction, these twins are represented as a trade-off in intensity between the a- and c-axis peaks depending on the orientation of the detector. In this work, the occurrence of such a shift has shown evidence that ferroelastic twinning is active in the composite under load and is responsible for energy dissipation (damping) in the material.

In the electroformed $Ni-BaTiO_3$ composite system, $BaTiO_3$ tetragonal peaks are eclipsed by the primary Ni peaks of the matrix, so neutron diffraction studies could not provide useful information for this system. For the bronze matrix system, a cylindrical bronze-30v% $BaTiO_3$ composite sample was subjected to an oscillating stress state (±10 MPa) about a static compressive stress of 30 MPa at room temperature while being examined using neutron diffraction. This led to a maximum stress state of 40 MPa, well within the elastic region of the composite yet sufficient to initiate twinning in the reinforcement assuming ideal stress transfer.[3] The sample was subjected to 50 cycles at 1 Hz. Diffraction patterns were taken upon the initial loading at 1, 5, 10, 20, 30, and 40 MPa.

Then during each of cycles 1, 2, 5, 10, 25, and 50, five diffraction patterns were taken. To facilitate a sufficient neutron count, the cyclic loading was paused for ~1 hour while obtaining each diffraction pattern. For each cycle examined a pattern was taken at the initial 30 MPa stress state, the second at the maximum stress (40 MPa), the third upon passing through the static stress of 30 MPa, the fourth at the minimum stress (20 MPa) and again at the initial static stress of 30 MPa. The peak intensities found from these patterns are plotted in Figure 97.
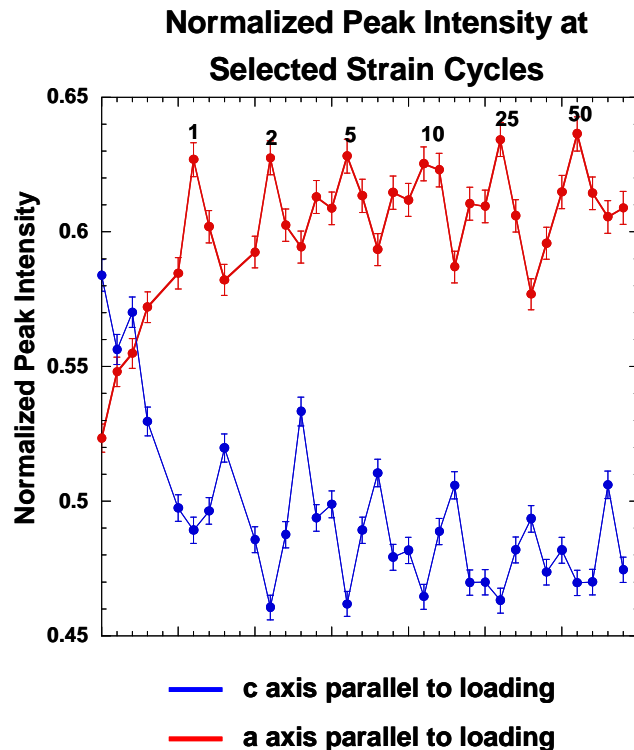
Figure 97. Normalized peak intensities for the a and c axes at selected strain cycles

Here the trade-off in intensity between the "c" and "a" axes becomes apparent and the fact that stress applied to the composite induces a change in the reinforcement is strong evidence of stress transfer in the composite system from the matrix to the reinforcement. This becomes more apparent when the peak intensities are plotted versus the stress applied to the sample. These results are shown in Figure 98.

141
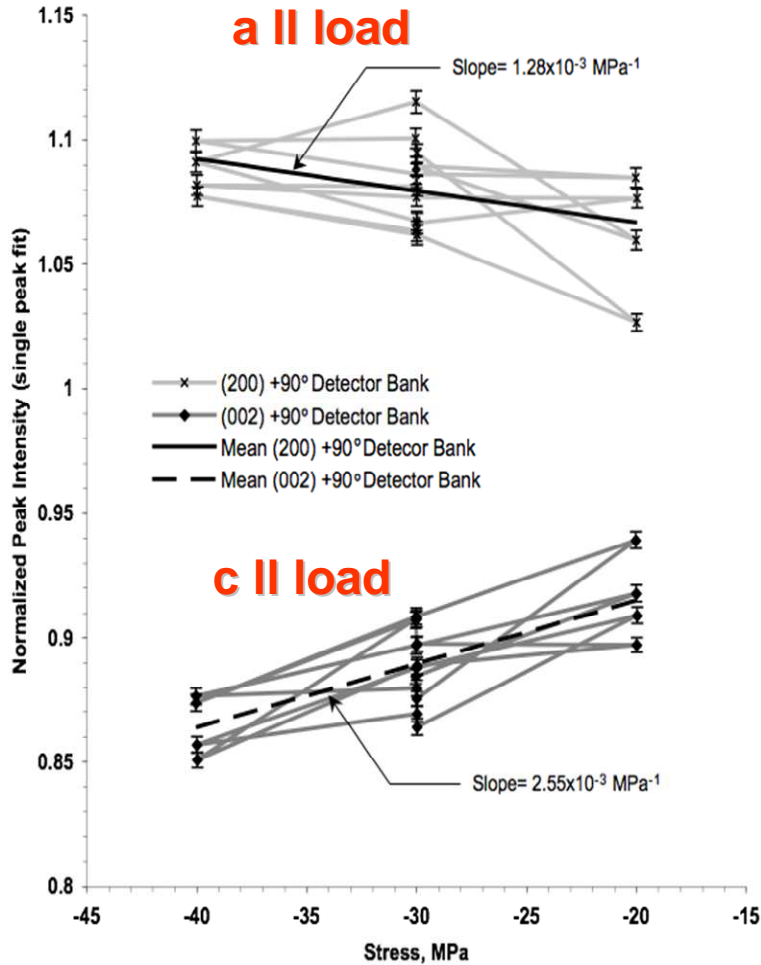
Figure 98. Peak intensity vs. compressive stress of the c- and a-axes perpendicular to the loading direction

As the stress was increased the peak intensity of the a-axis parellel to the applied load increased, while the peak intensity corresponding to the parellel c-axis decreased. This is evidence that the texture of the tetragonal structure has been modified through the formation of ferroelastic twins and agrees with the Forrester et. al. who performed similar neutron experiments for monolithic $BaTiO_3$. [42]

By comparing the average slopes of this change the magnitudes are not equal as predicted earlier. Comparison of the magnitude of the slope for each curve exhibits a preservation of the 2:1 ratio between the "a" and "c" axes, stemming from the fact that in a three-dimensional tetragonal system there exists two a-axes for each c-axis. The c-axis can

twin into either of the a-axis directions, thus depending on the orientation of the detector, only an average of half of the change seen in the c-axis is manifested as a change in the detected a-axis, with the other half affecting the undetected a-axis. This showed that the domains twinned allowing the elongated c axis to take a more favorable orientation, perpendicular to the applied stress. Upon unloading this twinning effect appeared to be reversible as the c peaks tended to recover to their initial intensity.

Chapter Five- Conclusions

Overall, significant evidence has shown that stress induced ferroelastic twinning is an active damping mechanism in ferroelectric reinforced metal matrix composites. The systems studied however, using current processing techniques, are far from ideal. The effects of increased volume percent reinforcement on $tan\ \delta$, although shown to increase the overall ferroelastic damping, are masked by the increase in $tan\ \delta$ stemming from additional porosity created as the v% $BaTiO_3$ is increased for both processing methods.

In the model System, the Cu- 10wt%Sn bronze and $BaTiO_3$ have been shown to be thermally compatible during high temperature sintering, and the Cu plated reinforcement greatly reduced the formation of porosity around the reinforcement. Here, composites having 0, 15, 30, and 45v% reinforcement were easily formulated, and ferroelastic domain twinning was shown to be an active damping mechanism. Evidence of this was first shown by a steep drop in tan δ upon heating through the T_C, but was then confirmed using neutron diffraction. By cyclically stressing a composite in the path of the neutron beam, the resulting diffraction patterns were used to measure the intensity of the peaks corresponding to the c-axis, which decreases in the loading direction, and the a-axis, which increases in the loading direction. This trade-off in intensity also preserved the 2:1 a:c ratio which is typical of the tetragonal structure of the $BaTiO_3$.

In further analysis of the damping behavior of the model system, irreversible damping mechanism are thought to be active as evidenced by a steep decrease in tan δ during the initial 400 strain cycles applied to the composite. There also seem to exist irreversible damping mechanisms inherent to matrix as a steep trop was also seen in for the pure bronze. However, the bulk of this ferroelastic twinning appears to be reversible, as the "c" to "a" axis trade-off in intensity was repeated over several compression cycles during neutron diffraction. Additionally, only a small decay in tan δ was seen from 400-30,000 strain cycles. Finally for the model system, the damping behavior does not exhibit a strong dependence on strain frequency from 0.01-40 Hz.

For the low temperature system, composite electroforming has been shown to be a viable means to combine Ni and $BaTiO_3$, which cannot be combined through traditional Ni processing techniques as they are not thermally incompatible at the temperatures required. Composite electroforming also shows promise as means to combine other thermally incompatible material systems. During fabrication, electroless plating of the $BaTiO_3$ reinforcement decreased the required BaTiO3 loading in the electrolyte and improve matrix/reinforcement interface.

Damping behavior for the low temperature system exhibited a low strain frequency dependence, across the range tested, 0.01-40 Hz. In evaluating the service life of the composite, the *tan δ* decreases gradually with increasing strain cycles. Unlike the bronze system, no drop in *tan δ* was seen upon heating through T_C. This may have been due to the small volume fractions of $BaTiO_3$ realized, (0, 3, 12v%). This allowed the damping behavior of the Ni to be dominant washing out any small drop in tan δ at T_C.

To more effectively study these effects, materials of greater quality should be utilized and improvement to the current fabrication methods should be explored. Composites of greater quality consisting of less flaws, would allow not only for a greater ferroelastic effect, but also a more precise quantification of that quantity, as the signal to noise ratio vs. that of other damping mechanisms would be increased. Specifically in the case of fabrication through electroforming, techniques allowing for greater volume percent

reinforcement involving a matrix metal with minimal internal friction should be investigated.

Damping behavior could also be increased using a reinforcement of increased quality. Reinforcement improvements are not only limited to improving the quality of $BaTiO_3$. Other materials of superior ferroelastic damping ability could be utilized further shifting the bulk curve upward. Increased mechanical properties of the reinforcement should also increase the mechanical properties of the composite. This will be increasingly important as the M/R interface is improved allowing for greater stress transfer between them, at which point an increase in the aspect ratio of the embedded material may be warranted. Improvements in the matrix will be primarily effective through a decrease in overall porosity, which can be blamed for the decrease in mechanical properties as reinforcement is added, shadowing any gains made through compositing.   This decrease in stress concentration sites coupled with an increase in effective cross-sectional area, can lead to improved mechanical properties as well as damping ability.

Chapter Six- Future Work

There are several changes that could be made to improve the magnitude of ferroelastic damping, as well as aid in the ability to distinguish between damping associated with tradition mechanisms and those stemming from ferroelastic behavior.

As previously mentioned, since matrix/reinforcement interface improvements lead to increased stress transfer, this interface is extremely important when attempting to maximize ferroelastic damping in the embedded ceramic. To improve the interface, future consolidation methods should result in a decreased level of porosity as compared to the current method of liquid phase sintering. In the case of the sintered bronze system, an obvious choice might be hot isostatic pressing (HIP). However elevated temperatures and isostatic pressures tend to favor the non-ferroelastic cubic phase of the reinforcement.[36] Cooling through the Curie temperature (T_C) at increased pressure prevents the efficient phase transition from the paraelectric, cubic phase to the ferroelastic/electric, tetragonal phase, by effectively decreasing T_C and stabilizing the cubic phase in $BaTiO_3$ as well as in most perovskite-type oxides.[36] Uniaxial pressure, however causes the polar c axis in a tetragonal structure to form perpendicular to the axis of the applied pressure,[36, 38] which can cause anisotropy in damping behavior.

In the ideal case, the consolidation process should be done at low pressure and temperatures well below those required by sintering. Decreased temperature during

processing would also allow for the use of better performing ferroelastic ceramics that are currently unstable in most metal matrices at current processing temperatures. This was demonstrated for the electroformed Ni system evaluated in this work. Ni and $BaTiO_3$ are not thermodynamically compatible at elevated temperatures, but remained as stable individual phases during electroforming at 70^oC. In this case however, porosity quickly became an issue with increasing volume fraction reinforcement when using a direct current source. The strong temperature dependent ferromagnetic damping behavior in Ni easily washed out any drop in *tan δ* see at T_C. In the future, periodic reverse methods could be utilized to combat the formation of porosity during electroforming, thus allowing for greater reinforcement incorporation. This combined with the use of a nonferromagnetic matrix should allow for greater resolution of damping contributed to ferroelastic mechanisms in the reinforcement.

With respect to the ceramic reinforcement itself, increased ferroelastic behavior could be seen by increasing grain size or through the use of single crystals. Damping could be further increased by using a ceramic fabrication method resulting in decreased porosity and that did not require grinding to reach the final particle size. High levels of porosity and residual internal cracks in the reinforcement not only lead to decreased damping ability, but also decreased mechanical properties. Finally the aspect ratio of the ferroelastic particles could be increased. The use of elliptical shaped particles or ideally short fibers would increase stress transfer allowing for greater activation of the reinforcement leading to more energy being dissipated (damped) by the composite.

Once a FR-MMC has been fabricated, damping due to ferroelastic mechanisms must be distinguished from that due to traditional mechanisms. In this work, this was done using neutron diffraction to directly measure twinning in the reinforcement, and DMA, to compare the damping behavior above and below the T_C of the ceramic reinforcement. If this second method is effective, since the ferroelastic properties are active below T_C, and cease completely above it.

To further increase this difference or drop in damping upon heating through T_C, a low damping, high stiffness matrix should be utilized. Ideally, this stiff metal should have a

high melting temperature relative to the T_C of the reinforcement to minimize changes in the matrix's damping ability upon heating through T_C.

One could also incorporate a non ferroelectric/ferroelastic reinforcement material otherwise having the same shape and mechanical and physical properties as $BaTiO_3$ into the same matrices studied in this work. Any variation between the $BaTiO_3$ reinforced composite system and the system having an "inert" reinforcement, both having the same matrix, should allow for quantification of the damping contribution due to the ferroelectric nature of the $BaTiO_3$ reinforcement.

In addition, it is proposed by the authors and in the literature that by using poled ferroelectric reinforcement, Joule heating can be induced in the matrix due the traditional piezoelectric effect.[70] Stress in the matrix would be transferred to the embedded piezoelectric particles creating a voltage across the material. Through this effect, stress would then be transferred into electrical energy and dissipated through resistive heating in the matrix. This would be another and possible more effective mechanism for the dissipation of vibrational energy in FR-MMCs.

References

1.   Cheng, B.; Gabbay, M.; Maglione, M.; Fantozzi, G., Relaxation Motion and Possible Memory of Domain Structures in Barium Titanate Ceramics Studied by Mechanical and Dielectric Losses. *Journal of Electroceramics* **2003,** 10, 5-18.

2.   Asare, T. A. Fabrication and Damping Behavior of Particulate $BaTiO_3$ Ceramic Reinforced Copper Matrix Composites. Virginia Polytechnic and State University, Blacksburg, 2004.

3.   Carman, G. P.; McKnight, G.; Chaplya, P.; Nersessian, N. *Magnetostrictive Particulate Composites for Damping*; F49620-01-1-0037; University of California, Los Angeles,: 2004.

4.   Kampe, S. L.; Aning, A. O.; Schultz, J. P.; Asare, T. A.; Poquette, B. D. In *Piezoelectric-Reinforced Metal Matrix Composites*, 11th International Conference on Composites / Nano Engineering (ICCE-11), Hilton Head, SC, 14-18 August, 2004; Hilton Head, SC, 2004; pp 657-658.

5.   Poquette, B. D. Damping Behavior in Ferroelectric Reinforced Metal Matrix Composites. Master of Science, Virginia Polytechnic Institute and State University, Blacksburg, VA, 2005.

6.   Christodoulou, L.; Venables, J., Multifunctional Material Systems: The First Generation. *JOM* **2003,** 55, (12), 39-45.

7.   Goff, A. C.; Aning, A. O.; Kampe, S. L., A Model to Predict the Damping Potential of Piezoelectric-Reinforced Metal Matrix Composites. *TMS Letters* **2004,** 1, (3), 59-60.

8.   Kampe, S. L.; Aning, A. O.; Schultz, J. P.; Goff, A. C.; Franklin, J. S. Piezoelectric Ceramic-reinforced Metal Matrix Composites. Patent #7126257, 2004.

9.   Yoshida, I.; Yokosuka, M.; Monma, D.; Ono, T.; Sakurai, M., Damping Properties of Metal-Piezoelectric Composites. *Journal of Alloys and Compounds* **2003,** 355, 136-141.

10.   Asmatulu, R.; Claus, R. O.; Mecham, J. B.; Inman, D. J., Improving the Damping Properties of Composites Using Ferrelectric Inclusions. *Journal of Intelligent Material Systems and Structures* **2005,** 15, (5), 463-468.

11.   Dowling, N. E., *Mechanical Behavior of Materials*. Prentice-Hall: Upper Saddle River, 1993.

12.   Lavernia, E. J.; Perez, R. J.; Zhang, J., Damping Behavior of Discontinuously Reinforced Al Alloy Matrix Composites. *Metallurgical and Materials Transactions* **1995,** 26A, (November), 2803-2818.

13.   Sinning, H. R., Low-Frequency Internal Friction of Metallic Glasses Near T_g. *Non-Crystalline Solids* **1989,** 110, 195-202.

14.   Lazan, B., *Damping of Materials and Members in Structural Mechanics*. First ed.; Pergamon Press Ltd.: Oxford, 1968; p 317.

15.   Ashby, M., *Materials Selection in Mechanical Design*. 2nd ed.; Pergamon Press: Oxford, 1999.

16.   Chung, D. D. L., Review: Materials for vibration damping. *Journal of Materials Science* **2001,** 36, 5733-5737.

17.   Taya, M.; Arsenault, R. J., *Metal Matrix Composites - Thermomechanical Behavior*. Pergamon Press: Oxford, 1989.

18.   Batist, R. D., *Internal Friction of Structural Defects in Crystalline Solids*. American Elsevier: New York, 1972; Vol. 5, p 477.

19.   Clyne, T. W.; Withers, P. J., *An Introduction to Metal Matrix Composites*. Cambridge University Press: Cambridge, 1993; p 509.

20.   Martin, J. W., *Micromechanisms in Particle-Hardened Alloys*. Cambridge University Press: Cambridge, 1980; p 201.

21.   Orowan, E., *Dislocations in Metals*. AIME: New York, 1954.

22.   Jaffe, B.; Cook, W.; Jaffe, H., *Piezoelectric Ceramics*. Academic Press Limited: India, 1971.

23.   Jaffe, B., A Primer on Ferroelectricity and Piezoelectric Ceramics. *Morgan Electroceramics Technical Publications*.

24.   Roberts, S., Dielectric Constants and Polarizabilities of Ions in Simple Crystals and Barium Titanate. *Physical Review* **1949,** 76, (8), 1215-1220.

25.   Robinson, P. Properties of Wrought Coppers and Copper Alloys. http://products.asminternational.org.ezproxy.lib.vt.edu:8080/hbk/index.jsp (2/2005),

26.   Bari, G. A. D., Electrodepositon of Nickel. In *Modern Electroplating, Fourth Edition*, Schlesinger, M.; Paunovic, M., Eds. John Wiley & Sons, Inc.: New York, 2000.

27.   Callister, W. D., *Materials Science and Engineering An Introduction*. 3rd ed.; John Wiley & Sons, Inc.: New York, NY, 1994; p 811.

28.   Kelly, A., *Strong Solids*. Clarendon Press: Oxford, 1966.

29.   Nardone, V. C., Assessment of Models Used to Predict the Strength of Discontinous Silicon Carbide Reinforced Aluminum Alloys. *Scripta Metallurgica* **1987,** 21, (10), 1313.

30.   Nardone, V. C., On the Strength of Discontinuous Silicon Carbide Reinforced Aluminum Composites. *Scripta Metallurgica* **1986,** 20, (1), 43-48.

31.   Aikin-Jr., R. M.; Christodoulou, L., The Role of Equiaxed Particles on the Yield Stress of Composites. *Scripta Metallurgica et Materialia* **1991,** 25, 9-14.

32.   Kelly, A.; Street, K. N., Creep of Discontinuous Fiber Composites II, theory for the steady-state. *Proc. R. Soc. Lon.* **1972,** A328, (2), 283-293.

33.   Courtney, T. H., *Mechanical Behavior of Materials*. McGraw-Hill: New York, 1990.

34.   Arsenault, R. J., Strengthening of Metal Matrix Composites Due to Dislocation Generation Through CTE Mismatch. In *Metal Matrix Composites: Mechanisms and Properties*, Everett, R. K.; Arsenault, R. J., Eds. Academic Press, INC.: San Diego, CA, 1991; pp 79-100.

35.   Ramakrishnan, N., An Analytical Study on Strengthening of Particulate Reinforced Metal Matrix Composites. *Acta Materialia* **1996,** 44, (1), 69-77.

36.   Jona, F.; Shirane, G., *Ferroelectric Crystals*. 1st ed.; Macmillan Company: New York, 1962; Vol. 1.

37.   Merz, W. J., Domain Formation and Domain Wall Motions in Ferroelectric BaTiO$_3$ Single Crystals. *Physical Review* **1954,** 95, (3), 690-698.

38.   Kim, S.; Chung, T.; Kim, D., Effect of External Compressive Stress on the Domain Configuration of Barium Titanate Ceramics. *Journal of the European Ceramic Society* **1993,** 12, (2), 147-151.

39.   Chou, J.; Lin, M.; Lu, H., Ferroelectric Domains in Pressureless Sintered Barium Titanate. *Acta mater.* **2000,** 48, 3569-3579.

40.   McNeal, M. P.; Jang, S.; Newnham, R. E., The Effect of Grain and Particle size onthe Microwave Properties of Barium Titanate (BaTiO3). *Journal of Applied Physics* **1998,** 83, (6), 3288-3297.

41.   Arlt, G., Twinning in ferroelectric and ferroelastic ceramics: stress relief. *Journal of Materials Science* **1990,** 25, 2655-2666.

42.   Forrester, J.; Kisi, E.; Studer, A., Direct Observation of Ferroelastic Domain Switching in Polycrystalline $BaTiO_3$ Using in situ Neutron Diffraction. *Journal of the European Ceramic Society* **2004,** article in press.

43.   S. Kampe, J. S., B. Poquette, T. Asare, D. Brown, In 2005.

44.   Schultz, J. P.; Asare, T. A.; Brown, D. W.; Poquette, B. D.; Kampe, S. L., Unpublished work. In Virginia Tech
LANSE: 2005.

45.   Pynn, R., *Neutron Scattering, A Primer*. Los Alamos Neutron Science Center: Los Alamos, NM.

46.   Dianoux, A.-J.; Lander, G., *Neutron Data Booklet*. 2 ed.; Institut Laue-Langevin: Grenoble, France, 2003.

47.   Spectrometer for Materials Research at Temperature and Stress. http://lansce.lanl.gov/lujan/instruments/SMARTS/index.html (7/20),

48.   Schlesinger, M., Electroless Deposition of Nickel. In *Modern Electroplating*, 4th ed.; Schlesinger, M.; Paunovic, M., Eds. John Wiley & Sons, Inc.: New York, NY, 2000; pp 667-684.

49.   Shipley, C. R. Method of Electroless Deposition on a Substrate and Catalyst Solution Therefore. 3,011,920, Dec. 5, 1961.

50.   Kanani, N., *Electroplating and Electroless Plating of Copper & its Alloys*. Finishing Publications Ltd.: Herts,UK, 2003.

51.   Saubestre, E. B., Plating of Nonconductors. In *Modern Electroplating*, 3rd ed.; Lowenheim, F. A., Ed. Electrochemical Society: Princeton N. J., 1974; pp 636-655.

52.   Horkans, J.; Sambucetti, C.; Markovich, V., Initiation of Electroless Cu Plating on Nonmetallic Surfaces. *IBM Journal of Research and Developement* **1984,** 28, (6), 690-696.

53.   Paunovic, M.; Schlesinger, M., *Fundamentals of Electrochemical Deposition*. Wiley-Interscience: New York, 1998; p 301.

54.   D'Ottavio, E. D. Colloidal Metal Activating Solutions for Use in Chemically Plating Non-conductors, and Process of Preparing Solutions. 3,532,518, 1970.

55.   Dressick, W. J.; Kondracki, l. M.; Chen, M.; Brandow, S. L.; Matijevic, E.; Calvert, J. M., Characterization of a Colloidal Pd (II)-based Catalyst Dispersion for Electroless Metal Deposition. *Colloids and Surfaces A: Physicochemical and Engineering Aspects* **1996,** 108, 101-111.

56.   Oita, M., Deposition Rate and Morphology of Electroless Copper Film from Solutions Containing 2,2'-dipyridyl. *Electrochimica Acta* **1997,** 42, (9), 1435-1440.

57.   Schneble_Jr., F. W. Ductility Promoter and Stabilizer for Electroless Copper Plating Baths. 3,607,317, 1971.

58.   Paunovic, M., Electroless Deposition of Copper. In *Modern Electroplating*, 4th ed.; Schlesinger, M., Ed. John Wiley & Sons, Inc.: New York, NY, 2000; pp 645-665.

59.   Mallory, G. O., The Fundamental Aspects of Electroless Nickel Plating. In *Electroless Plating Fundamentals and Applications*, Mallory, G. O.; Hajdu, J. B., Eds. American Electroplaters and Surface Finishers Society: New York.

60.   Pearlstein, F., Electroless Plating. In *Modern Electroplating*, 3rd ed.; Lowenheim, F. A., Ed. Electrochemical Society: Princeton, NJ, 1974; pp 710-747.

61.   Dini, J. W., Electrodeposition of Copper. In *Modern Electroplating, 4th Edition*, Schlesinger, M.; Paunovic, M., Eds. Jonh Wiley & Sons, Inc.: New York, 2000.

62.   Spiro, P., *Electroforming*. 2nd ed.; Robert Draper LTD: Teddington, 1971.

63.   German, R. M., *Powder Metallurgy Science*. 2nd ed.; Metal Powder Industries Federation: Princeton, NJ, 1994.

64.   DiBari, G. A., Nickel Plating. In *Metal Finishing Guidebook and Directory*, Tucker, R. E., Ed. G. Valero: New York, NY, 2007; Vol. 74th.

65.   Beer, F. P.; E. R. Johnston, J., *Mechanics of Materials*. 2nd ed.; McGraw-Hill, Inc.: New York, NY, 1992; p 740.

66.   Asare, T. A. Investigating Ferroelastic and Piezoelectric Vibration Damping Behavior in Nickel-barium Titanate and Nickel-PZT Composites. Virginia Polytechnic and State University, Blacksburg, 2007.

67.   Moustafa, S. F.; Abdel-Hamid, Z.; Abd-Elhay, A. M., Copper matrix SiC and Al_2O_3 Particulate Composites by Powder Metallurgy Technique. *Materials Letters* **2002,** 53, 244-249.

68.   Hampshire, W. B. Pure Tin.

69.   Lee, T. R.; Chang, C. P.; Kao, P. W., The tensile behavior and deformation microstructure of cryo-rolled and annealed pure nickel. *Materials Science and Engineering A* **2005,** 408, 131-135.

70.   Law, H. H.; Rossiter, P. L.; Simon, G. P.; Koss, L. L., Characterization of Mechanical Vibration Damping by Piezoelectric Materials. *Journal of Sound and Vibration* **1996,** 197, (4), 489-513.

71.   Popov, E. P., *Introduction to Mechanics of Solids*. 1st ed.; Prentice-Hall, Inc.: Englewood Cliffs, 1968; p 570.

Appendix A: Derivations of the Maximum Stress, Maximum Strain and Instantaneous Slope Equations in Three-Point Bending

A-1 Maximum Stress Equation in Three-Point Bending

Three point bending is a form of pure bending.[65] Pure bending theory can be used to calculate the stress (σ) at any point in a member based on the force applied and the member geometry. The original load (P) applied at the midspan from Figure 24 in Chapter 3, can be represented by one half of P translated to either end of the member combined with the two moments M, as illustrated in Figure 41.
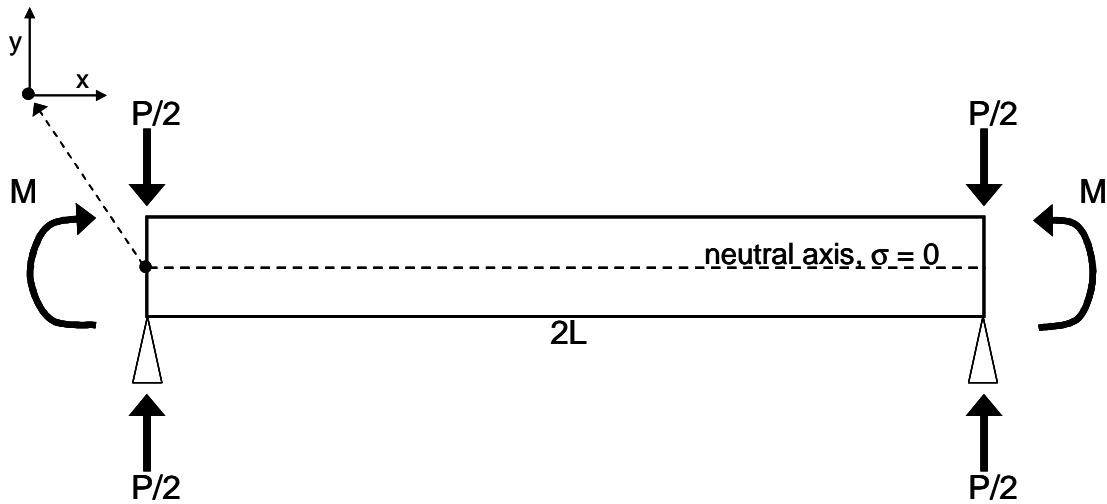

Figure 99. Three-point bending represented by two moments combined with translated stresses

Based on this rearrangement, an expression for stress (σ_x) at coordinates xy inside the member is given by Eq. 37.[65] This relation is known as the elastic flexure formula for beams.

$$\sigma_x = -\frac{My}{I}$$

[37]

Here M is the moment from Figure 41, y is the distance from the neutral axis and I is the moment of inertia. M and I can be broken down further as shown in Eqs. 38 and 39.[65]

$$M = \frac{PL}{2}$$

[38]

$$I = \frac{1}{12}wt^3$$

[39]

Eq. 35 stems from the definition of a moment, and Eq. 39 from the definition of the moment of inertia of a member having a rectangular cross-section. By combining Eqs. 37-39, a new expression for σ_x can then be found as shown in Eq. 40.

$$\sigma_x = -\frac{6PLy}{wt^3}$$ [40]

Finally since it is known that σ_{max} occurs at the surface of the member, one half of the member thickness ($t/2$) can be substituted for y in Eq. 40, resulting in the expression for σ_{max}, shown in Eq. 41.

$$\sigma_{max} = \frac{3PL}{wt^2}$$ [41]

Eq. 41 is identical to Eq. 31, which as previously mentioned in Chapter 3 is the equation used by the DMA software to calculate the maximum stress.

A-2 Equation for the Slope of the Stress/Strain Curve in Three-Point Bending

This relationship stems from Lagrangian mechanics which makes use of energy concepts using scalar functions instead of the vectorial representations found in Newtonian treatments. In mechanics, energy is defined as the capacity to do work, and work is the product of a force and the distance in the direction the force moves. In solid deformable bodies, stresses multiplied by their respective areas are forces, and deformations are distances. The product of these force and distance quantities represents the internal work done in a body by externally applied forces. This internal work is stored in a body as the internal elastic strain energy.

The internal elastic strain energy (U) can be represented in terms of stress and strain. This is done in an analogous manner for both normal and shear. For an infinitesimal element of a member, the definition of stress and the definition of strain are used to solve for the force and distance terms used to find the internal strain energy for uniaxial stress (dU_{normal}) and the internal strain energy in pure shear (dU_{shear}), respectively.   An example involving uniaxial stress in the x direction (σ_x) is shown in Eq. 42, and for pure shear in the xy plane (τ_{xy}) in Eq. 43.[71]

$$dU_{x\,normal} = \underbrace{1/2\,\sigma_x dydz}_{average\ force}\underbrace{\varepsilon_x dx}_{distance} = 1/2\,\sigma_x \varepsilon_x dxdydz = 1/2\,\sigma_x \varepsilon_x dV$$

$$\underbrace{\qquad\qquad\qquad\qquad}_{work\ (energy)}$$

[42]

$$dU_{xy\,shear} = \underbrace{1/2\,\tau_{xy} dxdz}_{average\ force}\underbrace{\gamma_{xy} dy}_{distance} = 1/2\,\tau_{xy}\gamma_{xy} dxdydz = 1/2\,\tau_{xy}\gamma_{xy} dV$$

$$\underbrace{\qquad\qquad\qquad\qquad}_{work\ (energy)}$$

[43]

Through the addition of dU_{normal} and dU_{shear} for each direction and with rearrangement, an expression for the total internal strain energy for an infinitesimal element (dU) can be found.[71]

$$\frac{dU}{dV} = 1/2\,\sigma_x \varepsilon_x + 1/2\,\sigma_y \varepsilon_y + 1/2\,\sigma_z \varepsilon_z + 1/2\,\tau_{xy}\gamma_{xy} + 1/2\,\tau_{yz}\gamma_{yz} + 1/2\,\tau_{zx}\gamma_{zx}$$

[44]

Integrating over the volume of the member gives Eq. 45.[71]

$$U = \frac{1}{2}\iiint_V (\sigma_x \varepsilon_x + \sigma_y \varepsilon_y + \sigma_z \varepsilon_z + \tau_{xy}\gamma_{xy} + \tau_{yz}\gamma_{yz} + \tau_{zx}\gamma_{zx})dxdydz$$

[45]

This expression is used for general elasticity. In the technical mechanics of solids a more specific class of problems is considered and Eq. 45 simplifies to Eq. 46.

$$U = \frac{1}{2}\iiint_V (\sigma_x \varepsilon_x + \tau_{xy}\gamma_{xy})dxdydz$$

[46]

This relation is sufficient for determining the strain energy in axially loaded bars as well as in bent and sheared beams.[71] This is because nearly all of the axial strain is occurring in the x direction and the shear strain in the xy plain.

For linearly elastic material, under uniaxial stress, $\varepsilon_x = \sigma_x/E$, and for pure shear, $\gamma_{xy} = \tau_{xy}/G$, according to Hooke's Law. Thus, with substitution and rearrangement, Eq. 46 transforms into Eq. 47, with E and G being the elastic and shear moduli, respectively.

$$U = \iiint_V \frac{\sigma_x^2}{2E} dx\,dy\,dz + \iiint_V \frac{\tau_{xy}}{2G} dx\,dy\,dz$$

$$\underbrace{\hspace{4cm}}_{\substack{\text{for axial loading and} \\ \text{bending in beams}}} \quad \underbrace{\hspace{4cm}}_{\text{for shear in beams}}$$

[47]

In the case of strain energy in bending, the first term in Eq. 47 can be further simplified through a substitution for σ_x according to Eq. 37. Then since both M and I are functions of x only and that by definition $\iint y^2 dy\,dz = I$, the first triple integral in Eq. 47 transforms to the last term in Eq. 48.

$$\iiint_V \frac{\sigma_x^2}{2E} dx\,dy\,dz = \iint_V \frac{1}{2E}\left(-\frac{My}{I}\right)^2 dx\,dy\,dz$$

[48]

$$= \iint_L \frac{M^2}{2EI^2}\left[\iint_A y^2 dy\,dz\right] dx = \int_L \frac{M^2}{2EI} dx$$

This result is Eq. 49 describing the total strain energy stored in the system (U) for beams in bending.

$$U = \int_L \frac{M^2}{2EI} dx + \iiint_V \frac{\tau_{xy}}{2G} dx\,dy\,dz$$

[49]

With this, an expression for deflection in the beam (δ) can be found by first setting U equal to the external work (W_e) using the principle of conservation of energy. The first law of thermodynamics expresses this principle, in Eq. 50,[71] stating that energy can neither be created nor destroyed.

$$\text{work done} = \text{change in energy}$$

[50]

For an adiabatic process, no heat is added or subtracted from the system. When no heat is generated (meaning forces are applied to the body so slowly that the kinetic energy can be neglected), the special form of this law for conservative systems reduces to Eq. 51.

$$W_e = U$$

[51]

Here W_e is the total work done by the externally applied forces during the loading process and U is the total strain energy stored in the system. It should be noted that the external work (W_e) added to the internal work (W_i) must equal zero.

$$W_e + W_i = 0$$

<div align="right">[52]</div>

Therefore, from Eqs. 52 and 53, the total strain energy is equal to the internal work,

$$U = -W_i$$

<div align="right">[53]</div>

where W_i has a negative sign since the deformations are opposed by the internal forces. This can then be applied to the case of a single elastic cantilever with a rectangular cross section in which a force (P) is applied at the free end as in Figure 42.
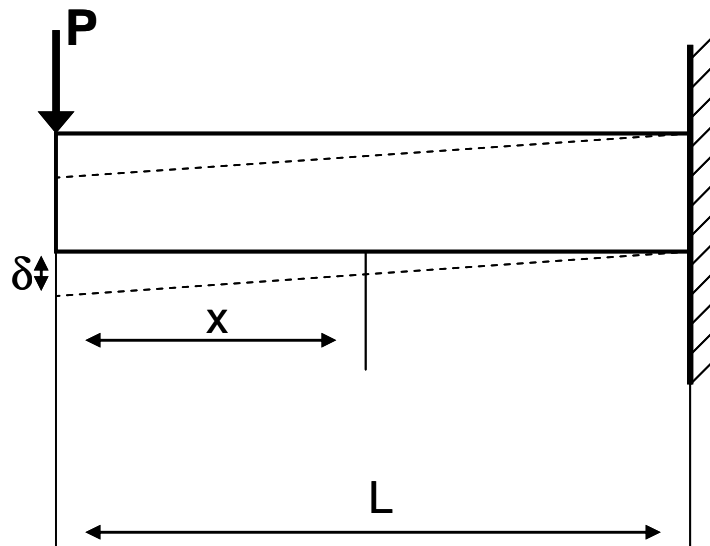

Figure 100. Single cantilever beam

As P is applied to the beam, Eq. 54 holds.

$$W_e = \frac{P\delta}{2}$$

<div align="right">[54]</div>

In this case, the total strain energy (U) consists of two parts. One part is due to the bending stresses ($U_{bending}$) and the other is caused by the shearing stresses (U_{shear}). Expressions for these parts can be found directly from Eq. 49 by the first and second terms on the right-hand side, respectively. The expression for $U_{bending}$ can be further simplified through substitution for M by noting $M = -P \cdot x$, and integrating along the length.

$$U_{bending} = \int_0^L \frac{M^2 dx}{2EI} = \int_0^L \frac{(-Px)^2 dx}{2EI} = \frac{P^2L^3}{6EI}$$

[55]

The expression for U_{shear} is found using the second term of Eq. 49. In the case of a single cantilever with a rectangular cross section, the shear at every section is equal to P, while the shear stress (τ) is a maximum at the neutral axis and is distributed parabolically across the plane of the cross section[71] as

$$\tau = \left[\frac{P}{2I}\right]\left[(t/2)^2 - y^2\right]$$

[56]

with t being the thickness of the beam and y the distance from the neutral axis. At increasing distances from the neutral axis, the shearing stresses gradually diminish, ceasing to exist at the upper and lower boundaries of the beam ($y = t/2$).

The infinitesimal volume ($dxdydz$) in Eq. 49, can be represented as $L{\cdot}w\,dy$. Making this substitution, along with that for τ in Eq. 56 and some additional rearrangement, one obtains the relation for U_{shear}, found in Eq. 57.

$$U_{shear} = \int_v \frac{\tau^2}{2G}dV = \frac{1}{2G}\int_{-t/2}^{t/2}\left[\frac{P}{2I}\left(\left(\frac{t}{2}\right)^2 - y^2\right)\right]^2 Lwdy$$

[57]

$$= \frac{P^2Lw}{8GI^2}\frac{h^5}{30} = \frac{P^2Lwt^5}{240G}\left(\frac{12}{wt^3}\right)^2 = \frac{3P^2L}{5AG}$$

From Eq. 54, and substituting using Eqs. 53 and 55, a relation involving U and δ is found.

$$W_e = U = U_{bending} + U_{shear}$$

[58]

$$\frac{P\delta}{2} = \frac{P^2L^3}{6EI}\frac{3P^2L}{5AG}$$

Finally, by rearranging, the Langrangian equation for deflection in the single cantilever mode is found as shown in Eq. 59.[71]

$$\delta = \frac{PL^3}{3SI} + \frac{6PL}{5AG} \qquad \qquad [59]$$

The 3-point bending case can be treated as two single cantilevers.[71] In this case, the deflection for two single cantilevers ($2 \cdot \delta$) should total twice that of one (δ), so Eq. 57 becomes Eq. 60.

$$2\delta = \frac{PL^3}{3SI} + \frac{6PL}{5AG} \qquad \qquad [60]$$

From here a substitution is made for G according to Eq. 59,[11] and also for A,

$$G = \frac{S}{2(1+\nu)} \qquad \qquad [61]$$

resulting in Eq. 62.

$$2\delta = \frac{PL^3}{3SI} + \frac{12\,PL\,(1+\nu)}{5wtS} \qquad \qquad [62]$$

Solving for S gives Eq. 63.

$$S = \frac{PL^3}{6\delta I} + \frac{12\,PL(1+\nu)}{10\,wt\,\delta} \qquad \qquad [63]$$

Multiplying the second term on right side by L^2/L^2 and making a substitution involving the stiffness (K) according to Eq. 64,

$$K = \frac{P}{\delta} \qquad \qquad [64]$$

gives Eq. 65.

$$S = \frac{KL^3}{6I} + \frac{12\,KL^3\,(1+\nu)}{10\,wtL^2} \qquad \qquad [65]$$

Substituting for I according to Eq. 36, and multiplying the second term on right side by t^2/t^2 leads to Eqs. 66.

$$S = \frac{KL^3}{6I} + \frac{KL^3 t^2\,(1+\nu)}{10\,IL^2} \qquad \qquad [66]$$

Rearranging gives Eq. 67.

$$S = \frac{KL^3}{6I} + \frac{KL^3}{I}\frac{1}{10}(1+\nu)\left(\frac{t}{L}\right)^2 \qquad [67]$$

Multiplying the second term on right side by 6/6 and simplifying leads to Eq. 68.

$$S = \frac{KL^3}{6I}\left[1 + \frac{6}{10}(1+\nu)\left(\frac{t}{L}\right)^2\right] \qquad [68]$$

Eq. 68 is identical to Eq. 32, which as previously mentioned is the equation used by the DMA software to calculate the slope at each data point in the s/s curve.

The direct Lagrangian solution of problems by equating the external work to the internal strain energy turns out to be useful in cases where only one force is applied to a member, as in three-point bending. To understand elastic systems subjected to any number of loads, a more general theorem for determining deflections and rotations of any element is needed. This theorem is associated with the name of Castigliano (1847-1884), and when applied to the simple case of an elastic beam having only one applied load, the solution simply becomes that of the Langrangian equation for deflection in the single cantilever mode,[71] shown in Eq. 59.

In order to determine not only elastic deformations but also deformations due to temperature changes, plastic deformations, and those due to misfit of the fabricated elements, a still more general procedure based on the concept of virtual work is required.[71] When the virtual work concept is applied to find the deflection at a point for the simple case of a linearly elastic beam, the solution becomes that of Castigliano's theorem.[71] Following, in the case of a single applied load (3-pt. bending), Castigliano's theorem in turn simplifies to the Langrangian equation for deflection in the single cantilever mode. When this equation is rearranged and the deflection is doubled to account for the use of two single cantilevers to represent three-point bending, it becomes the equation used by the DMA software to calculate the slope of the s/s curve at each data point.

A-3 Maximum Strain Equation in Three-Point Bending

With the equations. for σ_{max} and S known, the equation for ε_{max} is derived from a modified Hooke's Law.

$$\varepsilon = \frac{\sigma}{S} \qquad [69]$$

Since S is the slope at each point, his relation remains valid even for the nonlinear region of the s/s curve. This is only true however, when S is applied to each data point individually. Thus, S can be used to relate σ and ε, resulting in Eq. 70,

$$\varepsilon = \frac{\dfrac{PLt}{4I} = \dfrac{3PL}{wt^2}}{K\dfrac{L^3}{6I}\left[1 + \dfrac{6}{10}(1+v)\left(\dfrac{t}{L}\right)^2\right]} \qquad [70]$$

which simplifies to Eq. 71.

$$\varepsilon_{max} = \frac{6\delta t}{2L^2\left[1 + \dfrac{6}{10}(1+v)\left(\dfrac{t}{L}\right)^2\right]} \qquad [71]$$

Eq. 71 is identical to Eq. 33, which as previously mentioned is the equation used by the DMA software to calculate the maximum strain.

Appendix B: Large Optical Micrographs of the Cross-Sections of the Electroformed Nickel Composites
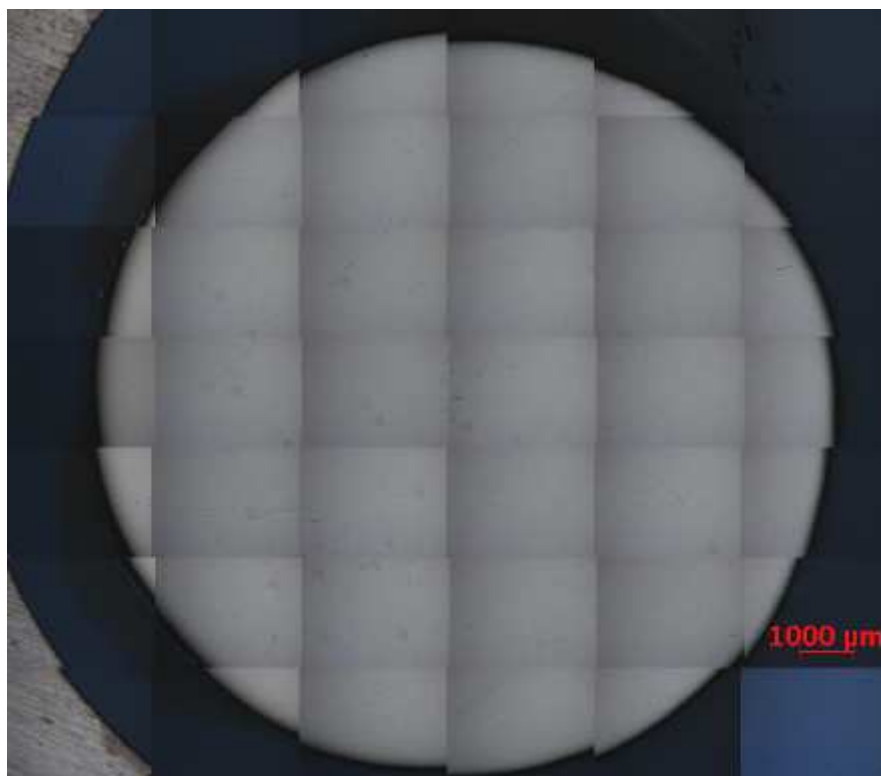
Figure 101. Cross section of Ni- 0v% BaTiO₃, Top A

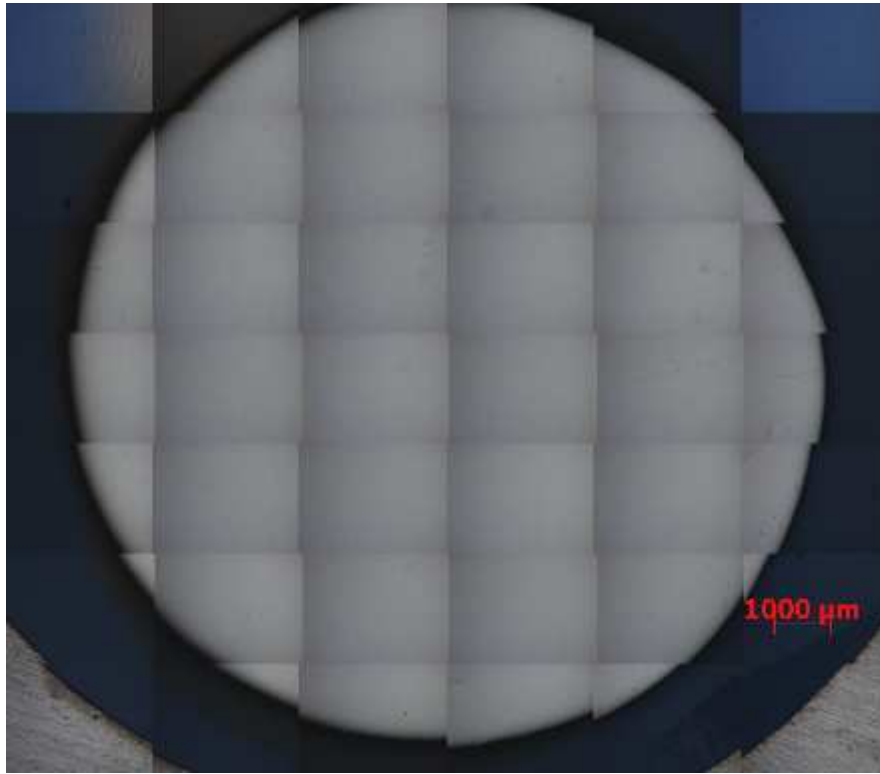**Figure 102. Cross section of Ni- 0v% BaTiO₃, Middle B**
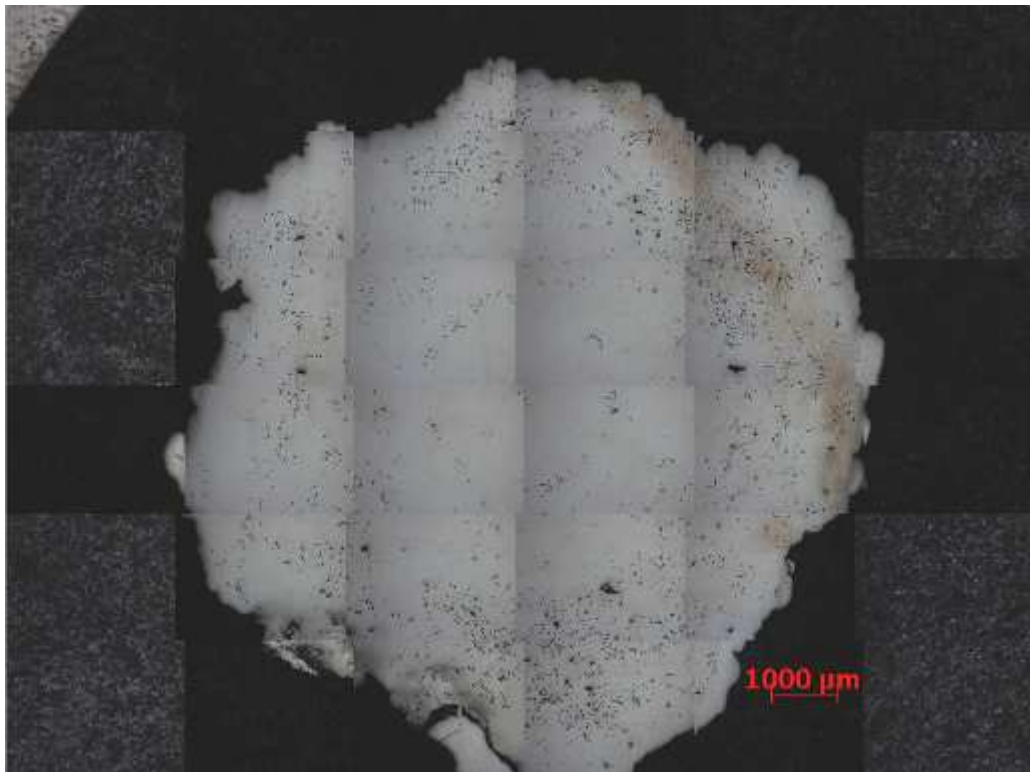
Figure 103. Cross section of Ni- 0v% BaTiO$_3$, Bottom C

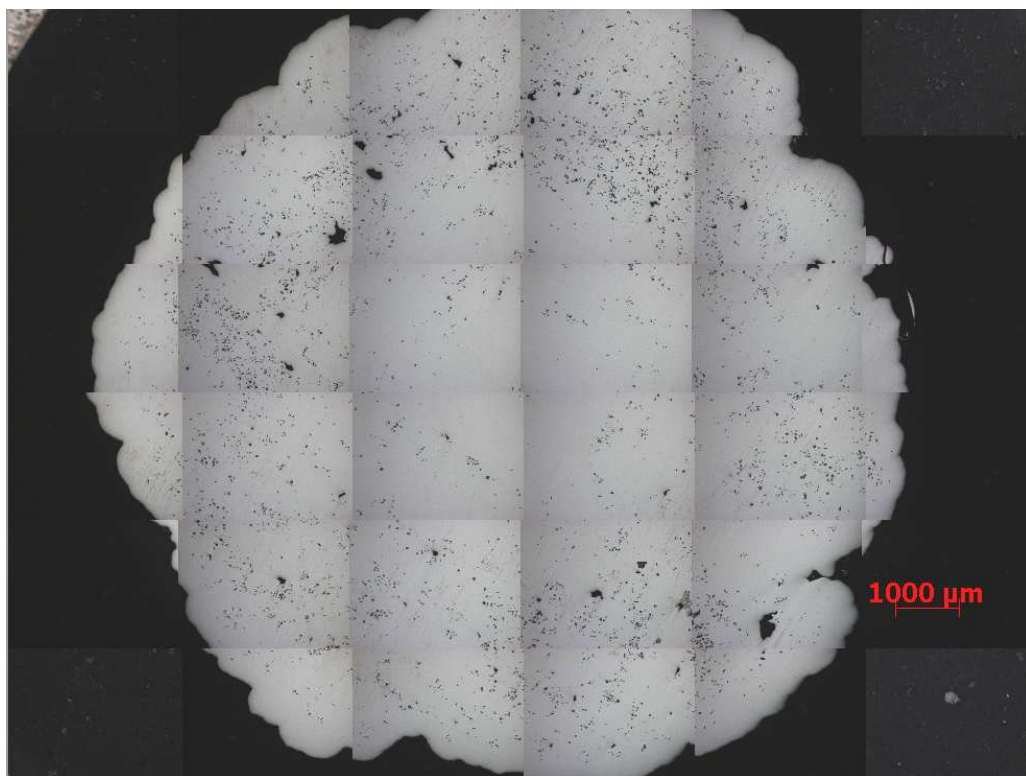**Figure 104. Cross section of Ni- 3v% BaTiO$_3$, Top A**
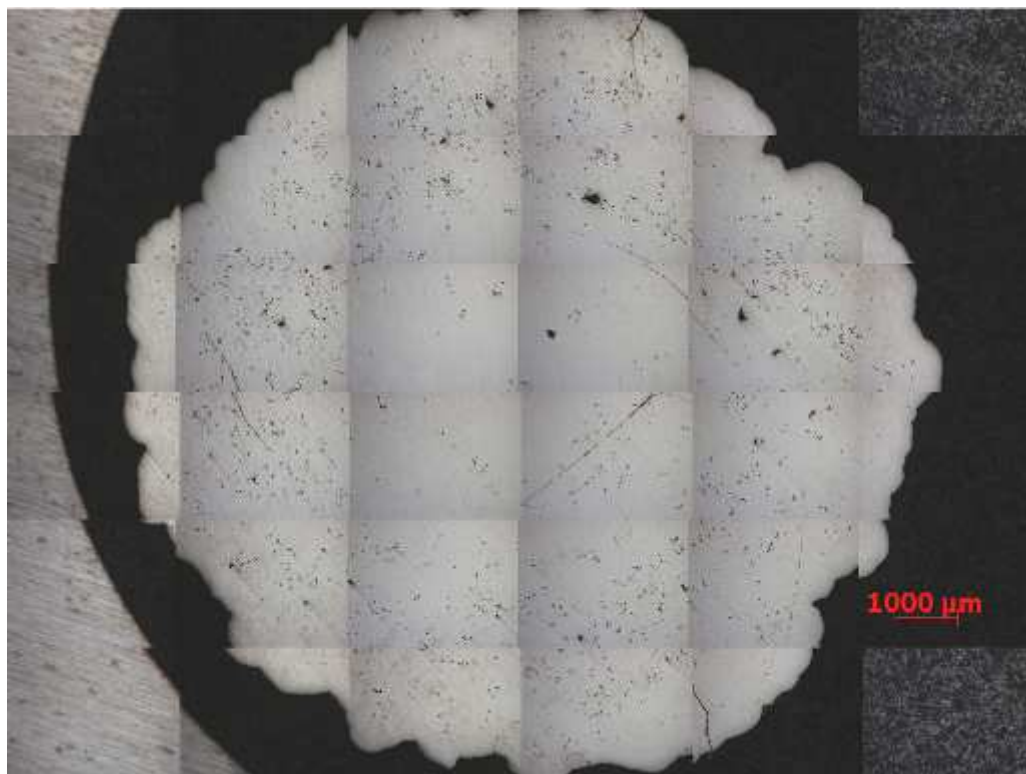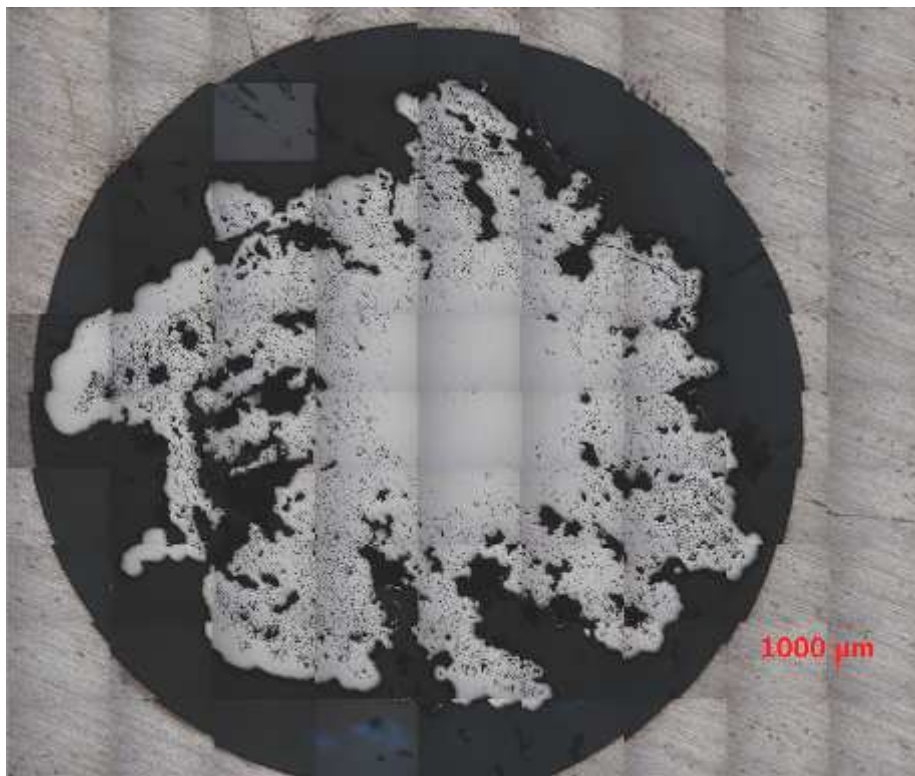
Figure 105. Cross section of Ni- 3v% BaTiO$_3$, Middle B

Figure 106. Cross section of Ni- 3v% BaTiO$_3$, Bottom C
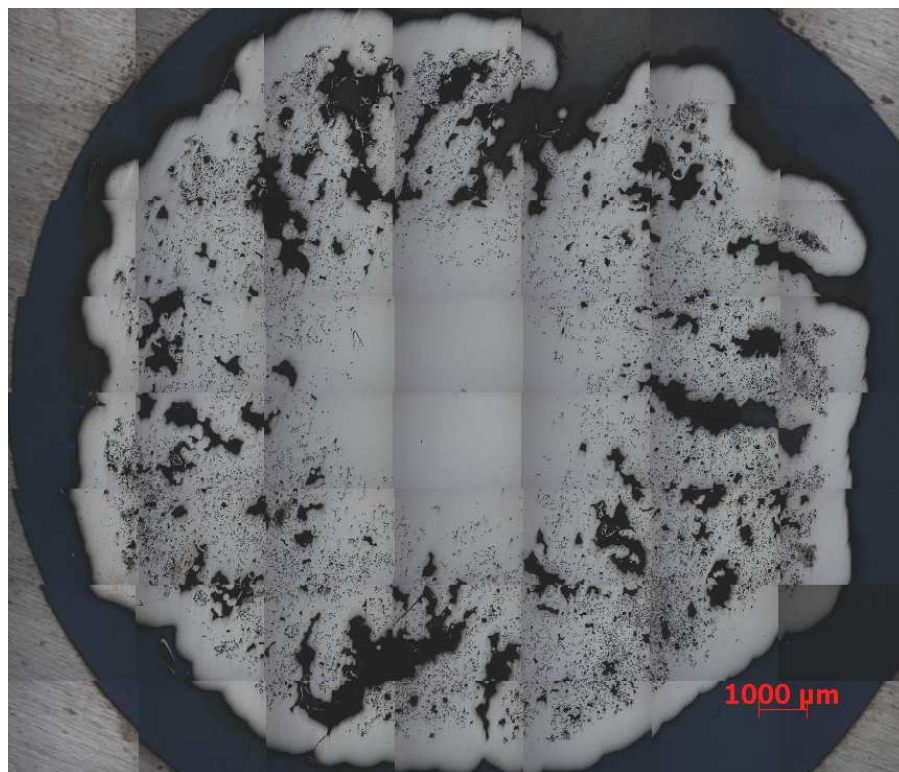
Figure 107. Cross section of Ni- 12v% BaTiO$_3$, Top A

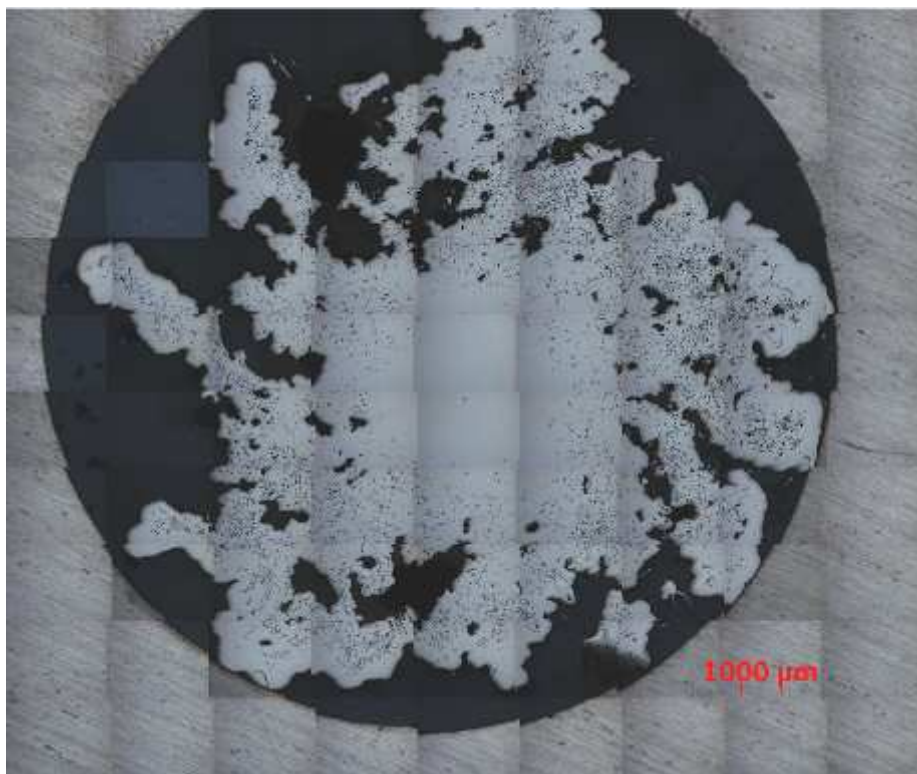**Figure 108. Cross section of Ni- 12v% BaTiO$_3$, Middle B**

Figure 109. Cross section of Ni- 12v% BaTiO$_3$, Bottom C

VITA

Ben Poquette was born and raised in and near the U.P. of Michigan, so as he got older it became obvious to attend Michigan Technological University, which was located even further north than his home. During his second year there, he took one year to study abroad in Xalapa, Mexico, where he learned Spanish. After a short bout with almost deciding to change majors, he continued in MSE, and in the Summer before his senior year, had an internship with Alcoa Aluminio in Recife, Brazil. Then in 2002 he received his bachelor's degree in MSE. Since then, he has been attending graduate school in MSE at Virginia Tech. While at Virginia Tech, he founded the Journal of Undergraduate Materials Research (JUMR).

It was also at Virginia Tech that met his fiancé, Christelle Jullian. She had an office down the hall and put up one heck of a fight. In his free time, Ben is an avid skier, and until recently was a member of the National Ski Patrol. He also loves the outdoors and traveling, and he brews a little hard cider on the side.